A Lagrangian Approach to Transport of Momentum and Biomass in Aquatic Biological Systems

Thesis by

Jifeng Peng

In Partial Fulfillment of the Requirements

for the Degree of

Doctor of Philosophy

California Institute of Technology

Pasadena, California

2010

(Defended June 19th, 2009)

Acknowledgements

In the first place, I would like to express my great gratitude to my advisor, Dr. John Dabiri, for his patient guidance, inspirational encouragement and excellent advice throughout the course of my Ph.D. study. For four years, he provided various training and supported my growth as a researcher. It as been a great experience to work with him. His ideas and passions in science have shown me what a first-class researcher needs.

I also want to thank Dr. Morteza Gharib for his support during my first year at Caltech. He provided a great opportunity for me to work on some very interesting projects during my rotation in his lab.

I would also like to gratefully recognize Dr. Shawn Shadden for introducing me to the concepts on which this thesis is based. He also provided great assistance to me in understanding both theory and calculation.

I am grateful to all of my collaborators on several research projects. I sincerely thank Dr. Robert Krasny, Dr. Jeff Eldredge, Dr. Ratnesh Shukla, Dr. George Lauder, Dr. Peter Madden, Dr. John Costello, Dr. Sean Colin, Dr. Moshe Rosenfeld, Dr. Tim Colonius, Dr. Kunihiko Taira, Mr. David Pekarek, Ms. Elisa Franco and Ms. Megan Wilson. Collaborations and discussions with them have contributed substantially to the studies presented in this thesis and beyond.

I also thank my colleagues in the group, Ms. Kakani Young, Ms. Lydia Ruiz, and Ms. Janna Nawroth for sharing experiences and knowledge during the time of study.

I would also like to express my great appreciation for Dr. Anthony Leonard, Dr. Jerrold Marsden, Dr. Morteza Gharib, and Dr. Sandra Troian for serving on my Ph.D. committee. I am grateful for their guidance and advice on my study.

Last, I thank my family for their ultimate support during the years of my study.

The research is funded by NSF Biological Oceanography Program grant OCE 0623475.

Abstract

In recent years, a Lagrangian Coherent Structures (LCS) method was developed to identify boundaries between distinct kinematic regions in unsteady flows. Many fluid transport processes can be described in terms of these kinematic boundaries in the flow. The method has since been applied to many engineering, biological, and geological fluid systems, but primarily on transport of homogenous fluid mass.

In this thesis, with emphases on aquatic biological transport systems, the LCS analysis is further developed to study momentum transport in animal locomotion and biomass transport in animal predation. Three independent studies are included in this thesis.

In the first study, LCS analysis is used to identify the boundary of the vortex attached to the fin in sunfish pectoral fin locomotion. A potential flow, deformable body theory is used to describe the dynamics of the vortex. The hydrodynamic forces acting on the fin are evaluated from the linear momentum of the vortex itself and its added-mass. The quantification of instantaneous locomotive forces provides necessary information for studying complicated locomotive behaviors such as motion control and maneuvers.

In the second study, the LCS analysis is applied to a numerically simulated undulatory swimming and shows existence of 'upstream fluid structures' that are invisible in Eulerian velocity/vorticity fields. These structures indicate the exact portion of fluid that interacts with the swimmer. A mass flow rate and a momentum flux are then defined. A metric for propulsive efficiency is established using the momentum flux, which can be used to measure and compare the efficiency of other engineering and natural propulsion systems.

In the third study, a framework is developed to study transport of zooplankton prey in the

feeding currents generated by a predator jellyfish. An equation of motion is proposed to describe the dynamics of prey in the flow. Then the concept of particle Lagrangian Coherent Structures (pLCS) is introduced to separate prey encounter regions from prey escape regions. The framework provides a mechanical basis for evaluating the predatory role of medusae in marine planktonic ecosystems. It can also be used to study transport and mixing in multiphase and granular flows in general.

Contents

Chapter 1

Introduction

Various fluid transport processes dominate physical interactions between aquatic animals and their fluid environments. Transport of mass, momentum and energy is ubiquitous in many functions and behaviors of aquatic animals. For example, locomotion, one of the most important functions and the basis for many other behaviors, is realized by momentum exchange between the animal and its fluid environment. This momentum exchange generates lift and thrust for locomotion. Many examples can be found in the swimming of medusae, amphibians, fishes, marine mammals et al. (e.g., Drucker and Lauder, 1999; Wilga and Lauder, 2004; Bartol et al., 2005; Dabiri et al., 2005; Stamhuis and Nauwelaerts, 2005). Animals are also known to utilize kinetic energy in ambient flows to facilitate maneuvering and improve their propulsive efficiency (Liao et al., 2003). In addition to locomotion, interactions with surrounding fluid are also used in predatory behaviors such as predator perception. For example, zooplankton such as copepods can detect the fluid mechanical signals generated by their predators and initiate escape response. Studies have shown that the signals for predator perception include several fluid velocity gradients, such as shear rate (Fields and Yen, 1996, 1997), vorticity and acceleration (Kiorboe and Visser, 1999; Kiorboe et al., 1999). Another important function influenced by fluid transport processes is feeding, as some animals can generate feeding currents to transport their prey and to facilitate feeding. For example, copepods use suspension feeding, in which they trap water borne particles by waving tentacles around in the water (Kiorboe and Saiz, 1995). Large hydromedusae and scyphomedusae periodically contract and extend their body to transport prey to the vicinity of tentacles (Costello and Colin 1994; Ford et al., 1997). Another example are whales,

which use suction feeding to draw prey into their mouths (Werth, 2006).

Methods used to study transport processes in animal-fluid interactions have evolved over the past half century. Early studies mostly use theoretical or semi-empirical models. Examples in locomotion studies include the slender fish model (Wu, 1971), the elongated-boddy theory (Lighthill, 1971), and several semi-empirical models (e.g., Webb and Blake, 1985; Vogel, 1994) which estimate locomotive forces from kinematic data of swimming appendages. In recent years, quantitative information of flow fields around animals become available, thanks to the developments in experimental and computational fluid mechanics. For experimental studies, the development of quantitative flow visualization techniques such as digital particle image velocimetry (DPIV) has enabled researchers to visualize flows around animals and to measure velocity and vorticity fields (e.g., Drucker and Lauder, 1999; Nauwelaerts et al., 2005; Spedding et al., 2003; Warrick et al., 2005). The development of computers and numerical methods facilitated many numerical studies on the interaction between aquatic animals and their fluid environments during locomotion and feeding (e.g., Eldredge, 2006; Jiang and Paffenhofer, 2008).

The availability of velocity field data from experimental measurements or numerical simulations provides quantitative information of flows around animals and enables studies on transport processes in detail. Most studies take a Eulerian perspective, directly analyzing Eulerian variables such as velocity fields or their derivatives such as vorticity fields or streamlines. These Eulerian variables are defined instantaneously and at fixed locations in space. For unsteady flows, which are characteristic of most biological fluid systems, a single frame of depiction of Eulerian properties does not provide much information on the evolution of flow and transport of mass, momentum, and energy. Generally, it is necessary to define a boundary to evaluate the transport equations (i.e., equations of mass, momentum and energy). However, the challenge of analyzing flow measurements from the Eulerian perspective is to identify consistent boundaries in the flow in which to evaluate the transport equations. The choice of boundaries and thus the interpretation of measured velocity data is currently *ad hoc*. Depending on the specific animal species and also the fluid transport processes, studies may focus on the fluid-solid boundary represented by the animal surface, the boundary layers on

the animal, or the surface of a control volume with length scales an order of magnitude larger than the animal itself. With different choices of boundaries and regions of interests, the requirements for resolution and field of view are different. So analyses are also sometimes limited by practical obstacles in flow measurements, especially in experimental studies.

Recent developments of Lagrangian, particle-tracking flow analyses have demonstrated that in many unsteady flows, there exist physically meaningful, fluid-fluid boundaries that act as barriers to fluid transport. A particular type of boundary is the Lagrangian Coherent Structures (LCS), developed by Shadden, Marsden, Haller and others from some dynamical systems concepts (Haller and Yuan, 2000; Haller 2001 and 2002; Shadden et al., 2005 and 2006). LCS are material surfaces, representing kinematic boundaries in the flow that separate the flow into different kinematic regions. Because they act as transport barriers in the flow, in many cases their temporal evolution can be used to describe transport. LCS technique has been widely applied to study fluid transport in a variety of applications. For example, the method has been used to study classical fluid mechanical problems such as the entrainment and detrainment of fluid in vortex rings (Shadden et al., 2006) and mixing in turbulence (Mathur et al., 2007). It has also been used to study cardiovascular flows (Shadden and Taylor, 2008; Xu et al., 2009), as well as meso-scale transport in atmospheric and oceanic flows (Sapsis and Haller, 2009; Shadden et al., 2009).

In these above-mentioned applications, the LCS analysis has been used primarily to understand transport of homogenous fluid mass. For aquatic biological systems, it is often more important to study the transport of momentum during locomotive activities. Also important is the transport of biomass during feeding processes. Therefore, the LCS technique is further developed in this thesis to study momentum and biomass transport and to understand interactions between animals and their fluid environments for locomotion and feeding respectively. Specifically, three transport systems are studied independently in this thesis: 1. locomotive force generation in sunfish pectoral fin; 2. propulsion energetics in undulatory swimming; and 3. interactions through fluid flows between a planktonic predatory pair. For each of these studies, an LCS-based approach is developed to study the corresponding transport processes.

The first study presents an approach to quantify unsteady fluid forces generated by swimming animals, based on measurements of the surrounding flow fields. Current state-of-the-art Eulerian approaches based on empirical wake velocity/vorticity measurements can only determine time-averaged locomotive forces, in which unsteady effects like added-mass tend to cancel when integrated over a swimming cycle. Using pectoral fin locomotion of bluegill sunfish (*Lepomis macrochirus*) as a demonstration, the LCS analysis is used to identify the boundary of the vortex attached to the fin. Its dynamics is approximated by potential flow concepts, especially the Kirchhoff and deformation potentials from deformable body theory. Instantaneous locomotive forces are evaluated and compared with previous estimation of time-averaged forces.

In the second study, a vortex sheet method is used to numerically simulate self-propelled swimming of an eel-like undulatory swimmer. The LCS analysis is applied to the simulated flow and reveals a type of 'upstream fluid structure', which is invisible in Eulerian velocity/vorticity fields. The 'upstream fluid structure' is demonstrated to be the exact portion of fluid that interacts with the swimmer. A mass flow rate is then defined and a momentum flux is calculated. A metric for propulsive efficiency is established using the momentum flux, which can be used to measure and compare the efficiency of animal locomotion.

In the third study, transport of small organisms in fluid flow is investigated. Due to their mass and self-propulsion, the dynamics of small organisms are different from ideal fluid tracers. Considering these small organisms as small spherical particles, an equation of motion is proposed to describe the their dynamics. The concept of particle Lagrangian Coherent Structures (pLCS) is then developed to identify transport barriers in the dynamical systems of particles. As a demonstration, the method is applied to a marine predator-prey system. In this system, the predator, moon jellyfish *Aurelia sp.*, feed on small planktonic prey such as copepods. The system is unique in that jellyfish use swimming movements to generate flow currents, which induce transport of prey towards the tentacles and oral arms, where the prey are encountered. Based on the geometry of pLCS, a prey encounter region is quantified. The study is able to demonstrate prey selection based on prey size and escape behaviours. The encounter region determined by the model can also explain the observed

pattern of the encounter region in empirical prey tracking experiments.

This thesis is organized as follow: Chapter 2 gives a brief description of the theory and calculation of LCS. Chapters 3 to 5 are designated to each of the abovementioned three studies. These three chapters can be viewed independently. Chapter 6 provides a brief conclusion. Some of the other LCS related studies I worked on are presented in the Appendix.

The contents in Chapters 3 to 5 are reorganized from several papers listed as follow, with necessary modifications and some additional analyses.

Chapter 3

Peng, J., Dabiri, J.O. Non-invasive measurement of instantaneous forces during aquatic locomotion: A case study of the bluegill sunfish pectoral fin. *J. Exp. Biol.* 210: 685–689, 2007.

Peng, J., Dabiri, J.O. A potential-flow, deformable-body model for fluid-structure interactions with compact vorticity, application to animal swimming measurements. *Exp. Fluid* 43: 655–664, 2008.

Chapter 4

Peng, J., Dabiri, J.O. The 'upstream wake' of swimming and flying animals and its correlation with propulsive efficiency, *J. Exp. Biol.* 211: 2669–2677, 2008.

Chapter 5

Peng, J., Dabiri, J.O. Transport of inertial particles by Lagrangian Coherent Structures: application to predator-prey interaction in jellysh feeding. *J. Fluid Mech.* 623: 75–84, 2009.

Peng, J., Colin, S.P., Costello, J.H., Dabiri, J.O. A physical model of prey transport in feeding currents generated by predator medusae, submitted.

Chapter 2

Finite-Time Lyapunov Exponent and Lagrangian Coherent Structures

2.1 Introduction

In fluid mechanics, it is important to quantify transport of fluid. In many cases transport processes can be described in terms of specific material surfaces and kinematic boundaries in the flow that delineate fluid particles with distinct behaviors. The separatrices between different regions of the flow can be identified in steady flows from streamlines derived from the Eulerian velocity field. In steady flows, the separatrix commonly manifests itself as a closed recirculation bubble that traps fluid particles over long convective time scales. For example, in a vortex dipole flow (Fig. 2.1), the dividing streamlines connecting two stagnation points, i.e., γ_1 and γ_2, are the separatrices in the flow. These trajectories separate the circulating fluid inside the vortex from the fluid that passes around the vortex.

In the language of dynamical systems, the dividing streamlines in the vortex dipole flow are called manifolds of the stagnation points. Specifically, the stable manifolds of point γ_1 are the trajectories that asymptote to point γ_1 in forward time as $t \to \infty$. In this steady flow, they coincide with unstable manifolds of point γ_2, i.e., the trajectories that asymptote to γ_2 as $t \to -\infty$. The manifolds are called heteroclinic connections as they connect two different equilibrium points.

The concepts of manifolds can be used to identify separatrices in unsteady flows with appar-

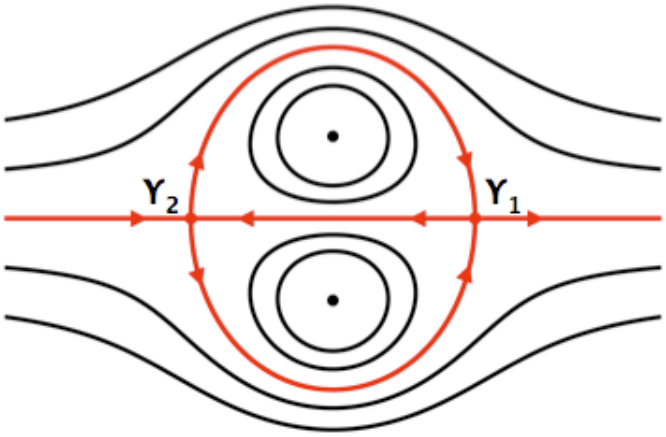

Figure 2.1: Schematic of streamlines and manifolds for the recirculation bubble of a vortex dipole. Fluid particle trajectories (i.e., streamlines in steady flow) that asymptote to the front stagnation point γ_1 as time $t \to \infty$ belong to the stable manifold of γ_1, whereas trajectories that asymptote to γ_1 as time $t \to -\infty$ belong to the unstable manifold of γ_1. The same considerations apply to γ_2.

ent temporal periodicity. This has been demonstrated in a variety of canonical systems including oscillating vortex pairs, isolated and leapfrogging vortex rings, and cylinder cross-flows (e.g., Aref 1984; Rom-Kedar and Wiggins, 1990; Rom-Kedar et al., 1990; Wiggins, 2005; Shariff et al., 2006). In general, heteroclinic connections observed in time-independent systems are typically broken in time-dependent systems. For example, by introducing a small time-periodic perturbation into the vortex dipole flow, the stable manifolds of point γ_1 and the unstable manifolds of point γ_2 do not coincide with each other, but exhibit spatial oscillations (Fig. 2.2). Stable and unstable manifolds still represent material surfaces, meaning that fluid does not cross these curves. However, there is no closed heteroclinic connection as in the steady vortex dipole flow. The stable manifolds of point γ_1 and the unstable manifolds of point γ_2 intersect with each other to form the heteroclinic tangle. The intersection of these manifolds creates regions called lobes, which indicate entrainment and detrainment of fluid (Rom-Kedar et al., 1990).

As demonstrated in Fig. 2.2, stable and unstable manifolds are able to separate distinct kinematic regions in simple flows with isolated vortical structures. However, they are strictly valid for time-periodic systems defined over infinite time. In unsteady flows with arbitrary time-dependence defined only over a finite time interval, it is often difficult to use manifolds to identify distinct kinematic

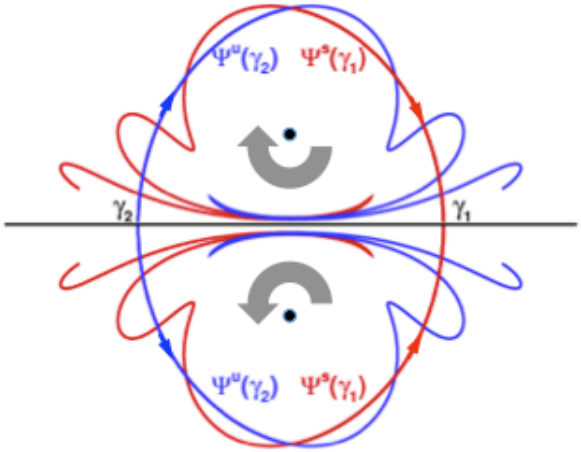

Figure 2.2: Schematic of perturbed vortex dipole analogous to the unperturbed steady case shown in Fig. 2.1. Red: stable manifolds of point γ_1; blue: unstable manifolds of point γ_2.

regions. To overcome this limitation, Shadden, Marsden, Haller and others (Haller and Yuan, 2000; Haller, 2001 and 2002; Shadden et al., 2005 and 2006) identified an analogous feature called Lagrangian Coherent Structures (LCS). LCS are identified from finite time Lyapunov exponent (FTLE) field, which measures separation of fluid tracers in the flow. FTLE offers a convenient way to identify transport barriers in arbitrary unsteady flow.

2.2 Definition of FTLE and LCS

Mathematically, the FTLE field was calculated from fluid tracer trajectories. The FTLE field measures separation rate in the flow. The ridges on FTLE contour plots, indicating local maxima of separation rate, identify the LCS. A detailed description of the FTLE calculation and LCS identification has been given in Shadden et al. (2005 and 2006). A simplified version is given here.

For a given flow field $\mathbf{u}(t, \mathbf{x})$, the trajectory of the fluid particle $\mathbf{x}(t; t_0, \mathbf{x}_0)$ is the solution of

$$\dot{\mathbf{x}}(t; t_0, \mathbf{x}_0) = \mathbf{u}(t, \mathbf{x}(t; t_0, \mathbf{x}_0)), \tag{2.1}$$

with initial conditions

$$\mathbf{x}(t_0; t_0, \mathbf{x}_0) = \mathbf{x}_0, \tag{2.2}$$

where the overhead dot denotes a time derivative. Here $\mathbf{u}(t, \mathbf{x})$ is an Eulerian property defined on fixed locations, whereas $\mathbf{x}(t; t_0, \mathbf{x}_0)$ is a Lagrangian property associated with a particle designated by $(t_0, \mathbf{x}_0)$.

To avoid confusion between particle trajectories and spatial coordinates, the notation ϕ is used for particle trajectories and $\mathbf{x}$ for spatial coordinates. By following particle trajectories over a duration of time T after initial time t_0, a flow map $\phi_{t_0}^{t_0+T}(\mathbf{x})$ is obtained that maps particles from their position $\mathbf{x}$ at initial time t_0 to their position at time $(t_0 + T)$, as

$$\phi_{t_0}^{t_0+T}(\mathbf{x}) = \mathbf{x}(t_0 + T; t_0, \mathbf{x}_0) = \phi_{t_0}^{t_0}(\mathbf{x}) + \int_{t_0}^{t_0+T} \mathbf{u}(\tau, \mathbf{x}(t; t_0, \mathbf{x}_0))d\tau. \tag{2.3}$$

Consider the trajectories for a slightly perturbed particle at $\mathbf{y} = \mathbf{x} + \delta\mathbf{x}(0)$ at initial time t_0. After a time interval T, this perturbation becomes

$$\delta\mathbf{x}(T) = \phi_{t_0}^{t_0+T}(\mathbf{y}) - \phi_{t_0}^{t_0+T}(\mathbf{x}) = \frac{d\phi_{t_0}^{t_0+T}(\mathbf{x})}{d\mathbf{x}}\delta\mathbf{x}(0) + O(\parallel \delta\mathbf{x}(0) \parallel^2), \tag{2.4}$$

where $\frac{d\phi_{t_0}^{t_0+T}(\mathbf{x})}{d\mathbf{x}}$ is the deformation gradient tensor $\mathbf{D}$, calculated as $D_{ij} = \frac{d\phi_i}{dx_j}$. By dropping higher order terms of $\delta\mathbf{x}(0)$, the magnitude of the perturbation is given by

$$\parallel \delta\mathbf{x}(T) \parallel = \sqrt{\delta\mathbf{x}(0) \cdot \Delta \cdot \delta\mathbf{x}(0)}, \tag{2.5}$$

where

$$\Delta = \frac{d\phi_{t_0}^{t_0+T}(\mathbf{x})}{d\mathbf{x}}^* \cdot \frac{d\phi_{t_0}^{t_0+T}(\mathbf{x})}{d\mathbf{x}} \tag{2.6}$$

is the (right) Cauchy-Green deformation tensor. The operator '$\cdot$' indicates the inner vector product and the superscript '*' denotes the transpose of a tensor. The magnitude of the perturbation is maximum when $\delta\mathbf{x}(0)$ is aligned with the eigenvector associated with the maximum eigenvalue of

Δ. That is, if $\lambda_{\max}$ is the maximum eigenvalue of Δ, then

$$\max \parallel \delta\mathbf{x}(T) \parallel = \sqrt{\lambda_{\max}(\Delta)} \parallel \delta\mathbf{x}(0) \parallel . \tag{2.7}$$

The FTLE, representing the maximum linear growth rate of a small perturbation, is defined as

$$\sigma_{t_0}^{T}(\mathbf{x}) = \frac{1}{|T|} \ln \parallel \frac{\delta\mathbf{x}(T)}{\delta\mathbf{x}(0)} \parallel = \frac{1}{2|T|} \ln \lambda_{\max}(\Delta). \tag{2.8}$$

The detonation $\sigma_{t_0}^{T}(\mathbf{x})$ means that FTLE characterizes the amount of fluid separation, or stretching, about the trajectory of a point starting at $\mathbf{x}$ over the time interval $[t_0, t_0 + T]$. The absolute value $|T|$ is used instead of T in the definition because FTLE can be computed for $T > 0$, indicating fluid particle separation; or for $T < 0$, indicating fluid particle attraction (i.e., fluid particle separation in backward time). An illustration is given in Fig. 2.3 in which fluid particle trajectories are used to locate the boundaries of a vortex ring. The vortex ring was generated experimentally by a piston-cylinder apparatus and the velocity field was measured by DPIV (details in Shadden et al., 2006). In Fig. 2.3A, fluid particle pairs straddling the rear vortex boundary separate faster than any other arbitrary pairs in forward time, indicating a larger value of forward-time FTLE at the rear boundary of the vortex ring; in Fig. 2.3B, fluid particle pairs straddling the front vortex boundary diverge faster than any other arbitrary pairs in backward time, indicating a larger value of backward-time FTLE at the front boundary of the vortex ring.

LCS are defined as ridges of the scalar FTLE field $\sigma_{t_0}^{T}(\mathbf{x})$. Intuitively, a ridge is a curve transverse to which the topography is a local maximum and the topography decreases most rapidly. A precise mathematical definition of a ridge on 2-dimesional $D \subset xy$-plane is provided by Shadden et al. (2005) as below.

*A **ridge** of σ is an curve $\boldsymbol{c} : (a, b) \to D$, satisfying the following consitions for each $s \in (a, b)$:*

SR1. *The vectors $\boldsymbol{c}'(s)$ and $\nabla\sigma(\boldsymbol{c}(s))$ are parallel.*

SR2. *$\Sigma(\boldsymbol{n}, \boldsymbol{n}) < 0$, where $\boldsymbol{n}$ is a unit normal vector to the curve $\boldsymbol{c}(s)$ and $\Sigma = \frac{d^2\sigma(\boldsymbol{x})}{d\boldsymbol{x}^2}$ is the*

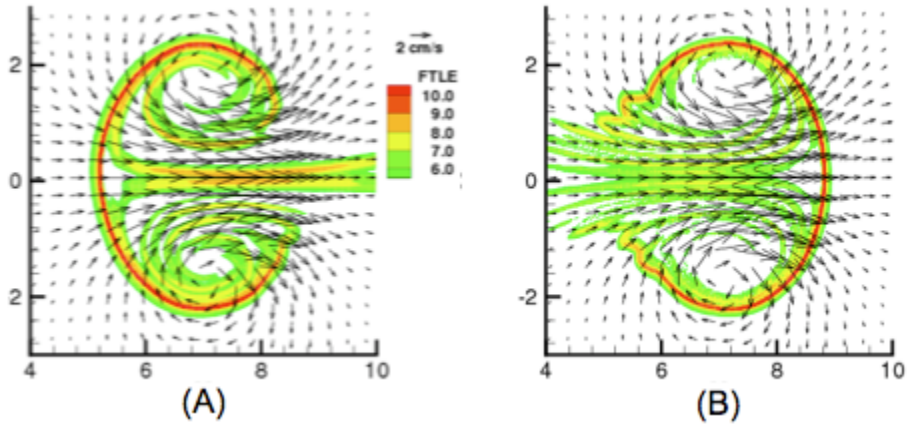

Figure 2.3: Contour plots of the FTLE fields computed from DPIV measurements of a vortex ring generated experimentally by a piston-cylinder apparatus. (A) forward-time FTLE; (B) backward-time FTLE. Position coordinates are specified in centimeters. Reproduced from Shadden et al. (2006).

Hessian of the FTLE field as a bilinear form evaluated at point $\mathbf{c}(s)$.

LCS can be readily identified from the FTLE contour plot. Figure 2.4 shows the LCS extracted from the FTLE fields in Fig. 2.3. LCS identified from forward-time FTLE is called repelling LCS, whereas LCS identified from backward-time FTLE is called attracting LCS. The increasingly sinuous nature of the repelling (attracting) LCS near the front (rear) of the vortex ring is the result of perturbations from an ideal, unperturbed vortex ring. Because LCS are material surfaces, the combination of repelling and attracting LCS indicate the boundary of the vortex ring (Shadden et al., 2006).

The concepts of FTLE and LCS are not limited to 2-dimensional dynamical systems as described above. They are equally applicable to N-dimensional dynamical systems. For a detailed description, please refer to Lekien et al. (2007).

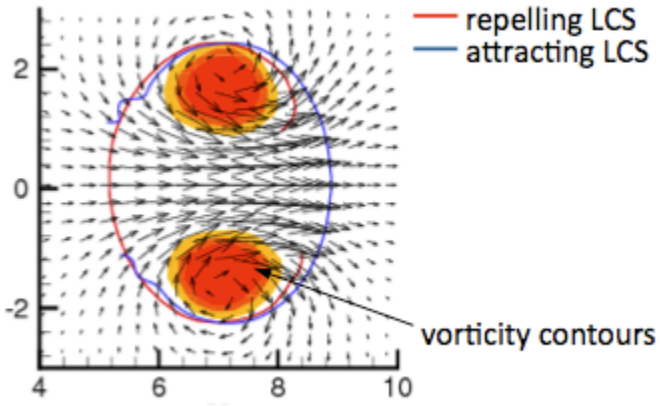

Figure 2.4: Intersection of attracting LCS (blue curve) and repelling LCS (red curve) define the vortex interior. Filled contours show the vorticity in the flow. Reproduced from Shadden et al. (2006).

2.3 Properties of LCS

FTLE $\sigma_{t_0}^T(\mathbf{x})$ characterizes the amount of fluid separation, or stretching, about the trajectory of a point starting at $\mathbf{x}$ over the time interval $[t_0, t_0+T]$. Though FTLE is a function of spatial location $\mathbf{x}$, starting time t_0 and integration time T, LCS is considered as only explicitly dependent on spatial location $\mathbf{x}$ and time instance t_0, not on T. This is because the length of integration time does not affect the location of the LCS. However, longer integration time can more accurately determine the LCS location by better resolving the ridges of local maxima in the FTLE contour plot. Figure 2.5 shows the FTLE for the same vortex ring as in Fig. 2.3 calculated with different integration time T. With a shorter integration time, the FTLE ridges are thick bands and the precise location of the LCS is difficult to determine; while with a longer integration time, the FTLE ridges become sharper, i.e., LCS resolve into clearly defined thin lines. However, the location of the ridge, i.e., LCS is consistent. In practice, the appropriate length of integration time depends on the particular flow being analyzed, but the 'rule of thumb' on the integration time T in any LCS analysis is that it should be chosen to be long enough so that the LCS is clearly identifiable on the FTLE contour plot. Since the length of integration time only affects the ease and accuracy with which the LCS are determined, it has no effect on the location of LCS as long as the integration time is long enough

that LCS is clearly defined.

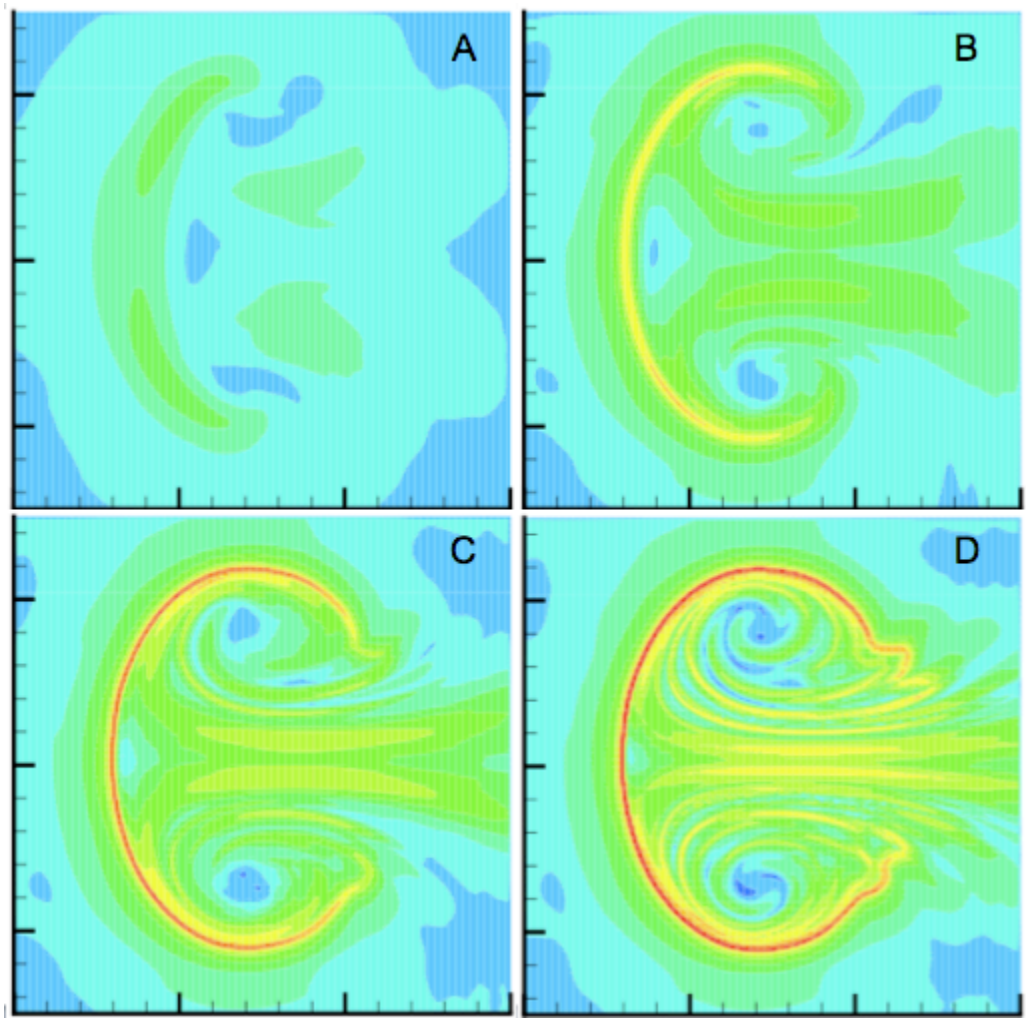

Figure 2.5: The effect of integration time on FTLE and LCS calculation for the same vortex ring as in Fig. 2.3. (A) integration time $T = 0.4$ s; (B) $T = 1.2$ s; (C) $T = 2.0$ s; (D) $T = 2.8$ s. with longer integration time, the FTLE ridges become sharper, i.e. LCS resolve into clearly defined thin lines.

LCS are equivalent to invariant manifolds. The attracting LCS, calculated from backward-time FTLE, are equivalent to unstable manifolds. The repelling LCS, calculated from forward-time FTLE, are equivalent to stable manifolds (Shadden et al., 2005 and 2006). For a well-defined LCS which is obtained from FTLE fields with a sufficient integration time $|T|$, the flux across it is very small (Shadden et al., 2005). Therefore, LCS can be sufficiently treated as material surfaces and transport barriers in flows (Haller, 2002; Shadden et al., 2006).

FTLE and LCS can be computed based on a finite-time record of a flow with arbitrary time-

dependence. This property is important for its applications to both numerically and empirically generated flows in studies of natural and engineering systems, which have these characteristics. In addition, an important benefit of LCS for flow analysis is its objectivity, or invariance under linear transformations of frame (Haller 2005). Furthermore, Haller (2002) showed that the geometry and kinematics of the LCS are robust to localized measurement errors in velocity fields, making it ideal for analyzing empirical and numerical velocity measurements typically defined on sets of discrete points in space and time.

2.4 Computation

This section discusses the numerical computation of FTLE and LCS. Consider the input as a time sequence of velocity data defined on a mesh of discrete points, obtained from empirical measurements or numerical simulations. To calculate FTLE $\sigma_{t_0}^T(\mathbf{x})$, a region of interest is first defined on which FTLE will be calculated. A Cartesian mesh is constructed over the region and used as the initial grid. For every point on the initial grid, its trajectories from $\mathbf{x}(t_0)$ to $\mathbf{x}(t_0+T)$ is calculated from Eqn. 2.3. A 4-th order Runge-Kutta algorithm is used to calculate the integration. When working with velocity data sets only known at discrete locations (like the data sets from DPIV measurements or CFD simulations), a cubic interpolation scheme is used to compute the velocity at arbitrary positions.

After trajectories are calculated, the (right) Cauchy-Green deformation tensor $\frac{d\phi_{t_0}^{t_0+T}(\mathbf{x})}{d\mathbf{x}}$ is evaluated for every node on the initial mesh. For a given node $\mathbf{x} = (x_{i,j}, y_{i,j})$, the deformation tensor is given by

$$\frac{d\phi_{t_0}^{t_0+T}(\mathbf{x})}{d\mathbf{x}} \Big|_{(x_{i,j}(t),y_{i,j}(t))} = \begin{bmatrix} \frac{x_{i+1,j}(t+T)-x_{i-1,j}(t+T)}{x_{i+1,j}(t)-x_{i-1,j}(t)} & \frac{x_{i,j+1}(t+T)-x_{i,j-1}(t+T)}{y_{i,j+1}(t)-y_{i,j-1}(t)} \\ \frac{y_{i+1,j}(t+T)-y_{i-1,j}(t+T)}{x_{i+1,j}(t)-x_{i-1,j}(t)} & \frac{y_{i,j+1}(t+T)-y_{i,j-1}(t+T)}{y_{i,j+1}(t)-y_{i,j-1}(t)} \end{bmatrix}. \tag{2.9}$$

This matrix is then multiplied by its transpose to obtain the Cauchy-Green tensor Δ. The largest eigenvalue of Δ is calculated to determine FTLE $\sigma_{t_0}^T(\mathbf{x})$ at every node on the mesh. This process

can be repeated to calculate FTLE for different t_0 at a series of time frames.

An in-house MATLAB package is developed using this algorithm to calculate FTLE from velocity data sets defined on discrete points (available for download at http://dabiri.caltech.edu/software.html). The code is validated by comparison of results against two case studies in Shadden et al. (2006), which used MANGEN, a C-language program package developed by F. Lekien and C. Coulliette (available for download at http://www.lekien.com/∼ francois/software). The Matlab code is used for FTLE calculations in this thesis.

Note that the FTLE field $\sigma_{t_0}^{T}(\mathbf{x})$ is only directly dependent on particle trajectories; velocity data is used only to calculate trajectories. Therefore, when flow velocity data is in a different format (e.g., Chapter 4) or the trajectories are not simple integration of flow velocity (e.g., Chapter 5), appropriate approaches are taken to calculate trajectories. From there the calculation of FTLE is the same.

The extraction of LCS curves from FTLE fields can be accomplished by a variety of *ad hoc* methods including thresholding or gradient searches of the FTLE field to identify local maxima. Shadden et al. (2005) derives more rigorous criteria; however, for practical purposes, identification of LCS from well-resolved FTLE fields is relatively insensitive to the implemented method of extraction. In this study, the ridges are extracted visually from FTLE contour plots.

Chapter 3

Vortex Boundary Identification and Locomotive Force Estimation

3.1 Summary

Swimming (and flying) animals generate unsteady locomotive forces by delivering net momentum into the fluid wake. Hence, locomotive forces can be quantified by wake momentum measurements. In most experimental studies based on wake measurements, quasi-steady flow is assumed and the flow analysis is based on velocity and/or vorticity fields measured at a single time instant during the stroke cycle. The assumption of quasi-steady flow leads to neglect of unsteady (time-dependent) effects, which can contribute significantly to the instantaneous locomotive forces. In this study, an LCS-based approach is proposed to empirically deduce unsteady locomotive forces based on the identification of vortex boundary and its kinematics in the animal wake. Using vortex boundary information derived from LCS analysis and a potential flow, deformable body theory, instantaneous locomotive forces are approximated as the rate of change of momentum of the wake vortex and its added-mass. The method is demonstrated in a case study quantifying the instantaneous locomotive forces generated by the pectoral fins of the bluegill sunfish (*Lepomis macrochirus*). A key result of this study is its suggestion that the dynamical effect of the vortex wake on locomotion is to replace the real animal fin with an 'effective appendage'. Benefits and limitations of this approach for non-invasive instantaneous force measurement are discussed, and its application to comparative biomechanics and engineering studies is suggested.

3.2 Introduction

The challenge of quantifying the locomotive forces exerted by fluids on swimming and flying animals has attracted interest from both biologists and engineers for many years. Early investigations of swimming and flying animals estimated the locomotive forces from kinematic data of locomotive appendages, due to the lack of experimental techniques to quantitatively measure the properties of the fluid wake. Quantification and validation of locomotive forces using these approaches relies heavily on semi-empirical models (for reviews, see Webb and Blake, 1985; Vogel, 1994).

Recent studies have focused on animal wakes. Newton's second and third laws dictate that swimming and flying animals generate net locomotive forces by transferring momentum into their wakes. Therefore, animal wakes act as 'footprints' of animal-fluid interactions and it is possible to estimate the locomotive force from wake measurements. Over the past decade, developments of flow visualization techniques, such as DPIV, have enabled direct visualization of animal wakes and quantitative measurements of velocity and vorticity fields (e.g., Drucker and Lauder, 1999; Lauder and Drucker, 2002; Spedding et al., 2003; Nauwelaerts et al., 2005; Warrick et al., 2005). These fluid dynamic data have provided necessary information for the estimation of locomotive forces based on kinematics and dynamics of animal wakes.

For most animals, the hallmark of their interaction with surrounding fluid is the creation of vortices. Hence, studies have aimed to quantify the momentum of fluid vortices generated by animals in order to estimate the associated locomotive forces. Several models have been proposed in this regard. These models typically estimate the time-averaged force rather than instantaneous forces. For example, studies have estimated the fluid forces based on measurements of the near-appendage circulation of vortices created by the animals (e.g., Dickinson, 1996; Dickinson and Gtz, 1996; Drucker and Lauder, 1999; Drucker and Lauder, 2002; Johansson and Lauder, 2004; Stamhuis and Nauwelaerts, 2005). In these cases, the momentum of the vortex is usually measured at the time instant when the vortex ring has just detached from the animal fin/wing. The time-averaged locomotive force over the stroke cycle is then determined by dividing the momentum of the shed vortex by the time duration of the stroke cycle. In other studies, the locomotive forces have been

evaluated by examining the wake far downstream, which is equivalent to taking the time-average of what occurred at the site of force generation (e.g., Spedding et al., 2003, Walker, 2004). These studies analyzing wake vorticity have found the measured time-averaged forces to be comparable with the necessary [but not sufficient (Dabiri, 2005)] lift and thrust required to sustain swimming and flying. However, time-averaged forces provide little information about the dynamics of swimming and flying. It is the instantaneous forces that dictate important dynamics of locomotion such as the trajectory, speed, maneuvers, and efficiency.

This study develops a method to empirically deduce unsteady swimming and flying forces from DPIV measurements of the surrounding flow fields. Unlike previous methods described above, the method is independent of the vorticity field, making it unnecessary to directly resolve boundary layers on the animal or body-vortex interactions in the wake. Instead, the method uses LCS analysis to identify the boundary of the vortex. When the vorticity field is sufficiently compact (i.e., bounded spatially), the dynamical properties of LCS can be approximated by potential flow concepts from deformable body theory. And these properties can be used to deduce unsteady locomotive forces on a swimming or flying animal.

As a demonstration, this method is applied to quantify instantaneous locomotive forces generated by the pectoral fins of the bluegill sunfish (*Lepomis macrochirus*) during labriform locomotion. Due to previous work on this species using the time-averaged vortex approach (e.g., Drucker and Lauder, 1999; Drucker and Lauder, 2000; Drucker and Lauder, 2001), good estimates of stroke averaged forces are available for comparison to the instantaneous forces calculated here. In addition, the mean vertical force is known, as the weight of sunfish underwater is a previously measured quantity (Drucker and Lauder, 1999), which allows a further check on the instantaneous force calculations. Furthermore, it is desired to explore the utility of this method with a data set of the kind that is typically available to investigators studying animal locomotion: a time series of two-dimensional DPIV velocity fields.

The outline of our approach is as follows: (1) the time-dependent velocity field of the wake of freely swimming sunfish is measured at high temporal and spatial resolution using DPIV; (2)

LCS analysis is used to identify the boundary of the vortex wake on the two-dimensional (2-D) plane from the velocity field data; (3) a three-dimensional (3-D) approximation based on the 2-D vortex boundary is used to determine the momentum of the vortex itself and its added-mass; (4) the corresponding locomotive forces acting on the pectoral fins are calculated. Unlike previous studies that estimated the time-averaged forces over the stroke cycle, this study provides detailed information on how locomotive forces evolve within the fin stroke cycle.

Like most studies involving time-averaged locomotive force estimation of swimming and flying animals, analysis in the present study is based on the flow velocity data from 2-D DPIV measurements. Assumptions regarding the three-dimensionality of the flow are taken and simplifications are made in the force evaluation. Limitations associated with the use of flow velocity data from a 2-D DPIV measurement to evaluate instantaneous locomotive forces are discussed in this study, and directions for future studies are suggested to enable more accurate force measurements.

3.3 Methods

3.3.1 Flow Measurements

Bluegill sunfish (*Lepomis macrochirus*) ($N = 7$, total body length $L = 17.3 \pm 1.0$ cm, mean $\pm$ s.d.) were collected by seine from ponds in Concord, MA, USA and maintained at an average temperature of 20 °C in 40 l aquaria. In experiments, sunfish swam individually in the center of the working area (28 cm $\times$ 28 cm $\times$ 80cm, height $\times$ depth $\times$ width) of a variable-speed freshwater flow tank under conditions similar to those described previously (Drucker and Lauder, 1999 and 2000). The sunfishes were trained to hold station in a current with a velocity of 0.5 $L \cdot s^{-1}$. At this relatively low speed, sunfish swimming usually involves use of the pectoral fins to generate locomotive forces (labriform locomotion). Only steady rectilinear swimming, during which the fish maintained a speed within 5% of the flow tanks current speed, was considered for analysis. To minimize wall effects, the fish were required to swim near the center of the volume of the working area. Thus the flow structures are assumed to result directly from movements of the fish pectoral fins.

DPIV was used to visualize and measure the wake of the sunfish pectoral fin. The DPIV technique provides empirical velocity field data for flow in 2-D sections of the swimming fish wake (for details, see Willert and Gharib, 1991). A 10 W continuous-wave argon-ion laser was focused into a thin light sheet, 1–2 mm thick and 10 cm wide, which illuminated reflective silver-coated neutrally-buoyant hollow glass spheres (mean diameter 12 μm) suspended in the water. Particle motion induced by pectoral fin activity was recorded by imaging the laser sheet with a high-speed video camera (Photron Fastcam-ultima APX, 1024×1024 pixels at 500 frames s^{-1}). In the experiments described herein, the laser was oriented to reveal the flow in the transverse plane, which crosses the left pectoral fin (Fig. 3.1) and intersects the sunfish body perpendicularly. This provided a full field view of the pectoral fin wake moving toward the camera, and the high temporal sampling rate provided a detailed image of pectoral fin wake flow patterns as the wake moved through the laser plane. Camera images of the transverse light sheet plane were obtained through a mirror located in the flow tank, well downstream (5–10 fin chord lengths) of the sunfish pectoral fin. Considerable effort was made to obtain DPIV images in which the fish was swimming as steadily as possible, not maneuvering, and in which the laser sheet sliced through the fin itself so that the boundaries of vortex structures relative to the fin as it moved during the fin beat cycle could be determined. The sunfish pectoral fin is translucent and the small supporting fin rays do not significantly obstruct the laser light, so no shadows were formed that might inhibit vector calculation between the fin and the body.

The analysis in this paper was focused on the vertical (lift or dorsal-ventral) and side (lateral) forces, for several reasons. (1) Time-averaged calculations of sunfish pectoral fin forces in both of these directions are available from previous work (Drucker and Lauder, 1999); (2) mean lift force should balance the weight of sunfish in water [sunfish are slightly negatively buoyant (Drucker and Lauder, 1999)], and mean lateral forces should be of the same magnitude, providing validation of the calculated instantaneous forces; (3) the DPIV data in the transverse plane were most accurately calculated in the lateral and vertical directions, while thrust estimates were not available as flow was moving through the imaging plane.

For the purpose of demonstration of the method in this study, only one representative set of

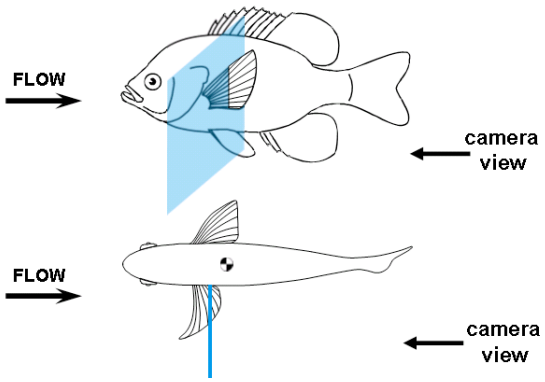

Figure 3.1: The side and top views of a bluegill sunfish and the laser plane (shown in blue) for the DPIV experiments that generated the data used for the analysis in this paper. Note that the camera viewed flow from behind the fish at 500 frames s^{-1}, and pectoral fin wakes thus move toward the field of view allowing a complete view of the wake at high temporal resolution.

velocity data was chosen for the following analyses. Accordingly, the results shown correspond to the specific set of data analyzed, not a composite analysis of all of the measurement samples.

3.3.2 Identification of Vortex Boundary

As in most fluid dynamics problems, the potential approaches for vortex boundary identification fall into one of two basic categories: Eulerian (i.e., fixed in space) or Lagrangian (i.e., moving with individual fluid particles). In most studies of animal vortex wakes, the vortex structure is determined from Eulerian data, using instantaneous vorticity or streamlines. For example, wake vortices have been previously identified by locating regions with vorticity above a given threshold (Drucker and Lauder, 1999; Drucker and Lauder, 2001; Stamhuis and Nauwelaerts, 2005). This approach is sometimes not objective, subject to the choice of threshold value. Few studies use closed or spiral streamlines to identify vortex structures in the animal wake; streamlines are able to give a clearly defined vortex boundary in a purely steady flow (e.g., a vortex dipole, Fig. 2.1), but are of less use in the highly unsteady flows characteristic of swimming and flying. A method of coordinate transformation has been previously developed to expand the utility of streamlines in time-dependent flow (Dabiri and Gharib, 2004), but its use is limited to unsteady cases where a single

dominate characteristic velocity can be identified in the wake, e.g., in the vortex-ring-dominated wakes generated by some jellyfish, squids, and salps.

An alternative is to study the wake from a Lagrangian perspective. Instead of studying the instantaneous velocity/vorticity field, fluid particle trajectories are used to identify vortices. By following fluid particle trajectories, vortices tend to emerge from the wake as coherent structures since, at the Reynolds numbers of relevance to animal locomotion, fluid particles remain inside a vortex over long convective time scales relative to fluid particles outside the vortex (Provenzale, 1999). This property enables implementation of LCS analysis based on FTLE calculation, which identifies boundaries between different kinematic regions. A demonstration was provided by Shadden et al., who used the combination of repelling and attracting LCS to identify the boundary of an empirical vortex ring generated by a piston-cylinder apparatus (Shadden et al., 2006; cf. Figs. 2.3 and 2.4). This LCS approach for vortex boundary identification is analogous to other methods used in time-dependent flows [e.g., hyperbolic trajectory approach (Haller, 2001, 2002 and 2005)], and is preferable because of its relative simplicity and wide compatibility.

In practice, the FTLE field was calculated from the time-series of discrete DPIV velocity field data, following the steps in Chapter 2. One of the difficulties in the present study is that the velocity measurement was made only over a relatively short time span (a single stroke cycle around 600 ms). Therefore, an integration length $|T| = 200$ ms or shorter was used due to the nature of the very short stroke cycle; this limited availability of velocity data prevented a calculation with a larger integration time.

Generally speaking, a long enough integration is required to obtain fully resolved FTLE (as described in Chapter 2). In ideal situations, when integration time is long enough, the LCS, i.e., high-value ridges on the FTLE contour plot, appear as clearly-defined thin curves. However, when the FTLE was not fully resolved due to the limitation of data, ridges have the form of thick bands. In this situation, center lines of the FTLE bands were used to approximate LCS.

Both forward and backward time FTLE were calculated and corresponding repelling and attracting LCS were identified. For an isolated vortex ring, the combination of the repelling and attracting

LCS gives the boundary of the vortex ring (Shadden et al., 2006; cf. Figs. 2.3 and 2.4.). The LCS were calculated on a series of frames, so the time-resolved boundary information of the wake vortex was determined.

3.3.3 Force Evaluation: Deformable Body Theory

Given the geometry and kinematics of the LCS in the flow, the goal is to use these structures to deduce dynamics of the corresponding flow field. The present method takes advantage of the fact that the LCS represent vortex boundary in the flow on which a no through-flow condition holds, since the LCS are material lines. Therefore, the fluid enclosed by the LCS can be treated as a deformable 'virtual vortex body' (Saffman, 1992). If the shear stresses on and outside the LCS boundary are negligible, then the flow external to the LCS can be treated as potential flow and solved as fluid potential from a linear homogenous boundary value problem with appropriate non-homogenous boundary conditions.

The potential flow hypothesis is valid, for example, when all of the vorticity in the flow is enclosed by the LCS, as demonstrated in the isolated vortex ring flow generated by the piston-cylinder apparatus (Shadden et al., 2006; also cf. Figs. 2.3 and 2.4). If the potential flow hypothesis holds, the dynamics of the 'virtual vortex body' can be described by a potential flow, deformable body theory developed by Galper and Miloh (1995). The hydrodynamical forces acting on the 'virtual vortex body' can be deduced and related unambiguously to the dynamics of the animal in the flow. The deformable body theory and the expression for locomotive forces are introduced in the following.

Let S refer generally to an arbitrary deformable body and consider this deformable body as submerged in an irrotational flow of an incompressible liquid. The ambient flow field surrounding the deformable body has a velocity of $\mathbf{U}_0 = \nabla\phi_0(\mathbf{X}, t)$, where ϕ_0 is the velocity potential of the ambient flow and $\mathbf{X}$ is the position vector measured relative to the laboratory frame of reference OX_1, X_2, X_3 (Fig. 3.2). The body has a linear translational velocity $\mathbf{U}$ (measured on its centroid), and an angular velocity $\mathbf{\Omega}$ with respect to a laboratory frame of references OX_1, X_2, X_3. A cartesian

coordinate system ox_1, x_2, x_3 is attached to its centroid and the surface of the body is expressed as $S(\mathbf{x}, t) = 0$ in the body-fixed reference frame. Then the deformation velocity of the surface $\mathbf{v}_d$, measured in the body-fixed coordinate system, satisfies

$$\mathbf{v}_d \cdot \mathbf{n} = -\frac{\partial S/\partial t}{|\nabla S|} \mid_S, \tag{3.1}$$

where $\mathbf{n}$ is the outward-facing unit normal to the surface.

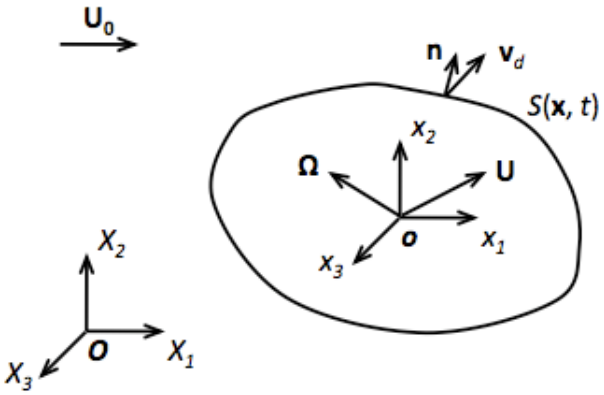

Figure 3.2: Schematic of a deformable surface S in a laboratory coordinate system OX_1, X_2, X_3 and a body-fixed coordinate system ox_1, x_2, x_3.

Assuming that the flow outside the surface S is irrotational, the velocity potential that arises due to the presence of the deformable body in the flow is given by

$$\boldsymbol{\phi} = \mathbf{U} \cdot \boldsymbol{\Phi} + \boldsymbol{\Omega} \cdot \boldsymbol{\Psi} + \boldsymbol{\phi_d} + \boldsymbol{\phi'}. \tag{3.2}$$

The harmonic functions $\boldsymbol{\Phi}$, $\boldsymbol{\Psi}$, ϕ_d and ϕ' represent, respectively, the translational Kirchhoff potential, rotational Kirchhoff potential, deformation potential, and additional potential associated with the ambient flow. These potentials satisfy the boundary conditions listed below:

$$\frac{\partial \Phi}{\partial n} = \mathbf{n} \mid_S \tag{3.3}$$

$$\frac{\partial \Psi}{\partial n} = \mathbf{x} \times \mathbf{n} \mid_S \tag{3.4}$$

$$\frac{\partial \phi_d}{\partial n} = \mathbf{v}_d \cdot \mathbf{n} = -\frac{\partial S/\partial t}{|\nabla S|} \mid_S \tag{3.5}$$

$$\frac{\partial \phi'}{\partial n} = -\mathbf{U}_0 \cdot \mathbf{n} \mid_S . \tag{3.6}$$

Each equation above is evaluated on the body surface S. According to Batchelor (1967), the fluid dynamic force $\mathbf{F}$ (per unit fluid density) acting on the deformable body is expressed as

$$\mathbf{F} = \frac{d}{dt} \int_S (\phi_0 + \phi)\mathbf{n} dS + \mathbf{F}_{st}, \tag{3.7}$$

where the steady force $\mathbf{F}_{st}$ is expressed as

$$\mathbf{F}_{st} = \frac{1}{2} \int_S (\nabla(\phi_0 + \phi))^2 \mathbf{n} dS - \int_S \nabla(\phi_0 + \phi)(\nabla(\phi_0 + \phi) \cdot \mathbf{n}) dS \tag{3.8}$$

Eqns. 3.7 and 3.8 give the full expression of the hydrodynamical force acting on a deformable body submerged in irrotational flow $\mathbf{U}_0 = \nabla\phi_0$ (Galper and Miloh 1995). The force $\mathbf{F}$ is dependent on harmonic function ϕ_0 and ϕ. According to Green formula,

$$\begin{aligned} \frac{1}{2} \int_S (\nabla\phi_0)^2 \mathbf{n} dS - \int_S \nabla\phi_0(\nabla\phi_0 \cdot \mathbf{n}) dS &= 0 \\ \frac{1}{2} \int_S (\nabla\phi)^2 \mathbf{n} dS - \int_S \nabla\phi(\nabla\phi \cdot \mathbf{n}) dS &= 0. \end{aligned} \tag{3.9}$$

So the steady force $\mathbf{F}_{st}$ only has terms of cross-product of $\nabla\phi_0$ and $\nabla\phi$,

$$\mathbf{F}_{st} = \int_S (\nabla\phi_0 \cdot \nabla\phi)\mathbf{n} dS - \int_S \left(\nabla\phi_0(\nabla\phi \cdot \mathbf{n}) + \nabla\phi(\nabla\phi_0 \cdot \mathbf{n})\right) dS \tag{3.10}$$

In the present study, it is assumed that this is no ambient flow, therefore $\mathbf{U}_0 = \nabla\phi_0 = 0$. Under this condition, $\mathbf{F}_{st} = 0$ and

$$\mathbf{F} = \frac{d}{dt} \int_S \phi \mathbf{n} dS, \tag{3.11}$$

with the velocity potential ϕ given by

$$\boldsymbol{\phi = \mathbf{U} \cdot \boldsymbol{\Phi} + \boldsymbol{\Omega} \cdot \boldsymbol{\Psi} + \phi_d.} \tag{3.12}$$

The fluid potential ϕ is solved from

$$\nabla^2 \phi = 0, \tag{3.13}$$

with the boundary condition that the velocity of the fluid at the surface is the same as the velocity of the deformable body in the normal direction:

$$\frac{\partial \phi}{\partial n} = (\mathbf{U} + \mathbf{x} \times \boldsymbol{\Omega} + \mathbf{v}_d) \cdot \mathbf{n} \mid_S . \tag{3.14}$$

Therefore, the flow external to the surface S can be solved as a linear homogenous boundary value problem with nonhomogenous boundary conditions, i.e., a solution of Laplaces equation for the velocity potential ϕ.

Eqn. 3.11 gives the hydrodynamical force acting on the deformable body. To apply to the present case, it gives the force acting on the boundary of the vortex ring defined by the LCS. For an isolated vortex ring attached to a swimming/flying appendage, as in the present study, the appendage resides inside the vortex ring. Therefore, the balance of this fluid dynamic force on the outside boundary of the vortex ring and the force $\mathbf{F}_{ext}$ applied by the animal to the appendage leads to a temporal change in the momentum of the vortex ring:

$$\mathbf{F} + \mathbf{F}_{ext} = \frac{d}{dt} \int_{V_V} \rho \mathbf{u} dV. \tag{3.15}$$

Strictly speaking, the right-hand side of Eqn. 3.15 should be expressed as $\frac{d}{dt} \int_{V_f} \rho_f \mathbf{u} dV + \frac{d}{dt} \int_{V_a} \rho_a \mathbf{u} dV$, i.e., the sum of the integrations over the fluid V_V and over the animal appendage V_a, with ρ_f and ρ_a being densities of fluid and animal. However, given the fact that animal density is usually close to the density of the fluid and fins are often very thin, e.g., the sunfish pectoral fin density is only 10% higher than water and its thickness is on the order of 100 μm (Alben et al., 2007; Lauder et

al., 2007), so the difference in the total mass of the vortex can be neglected in the subsequent force calculations.

Since the external force $\mathbf{F}_{ext}$ is applied by the animal, an equal and opposite locomotive force $\mathbf{F}_L$ is exerted by the fluid on the animal. Therefore,

$$\mathbf{F}_L = -\mathbf{F}_{ext} = -\frac{d}{dt}\left(\int_{V_V} \rho \mathbf{u} dV - \int_{S_V} \rho \phi \mathbf{n} dS\right). \tag{3.16}$$

Eqn. 3.16 is integrated over the vortex volume V_V and surface S_V, as illustrated in Fig. 3.3. Because evaluation of locomotive force using Eqn. 3.16 only requires geometry and kinematics of vortex boundary information, the LCS analysis is sufficient to provide the input information.

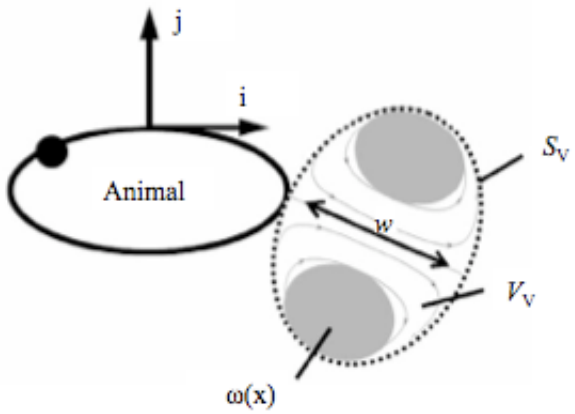

Figure 3.3: Schematic of wake vortex parameters described in the text. The distribution of wake vorticity $\boldsymbol{\omega}(\mathbf{x})$ is indicated by grey patches in this cross-section view. Hypothetical flow streamlines inside the vortex are sketched below the vortex patches. The dimension w is the wake vortex width. Reprinted from Dabiri (2006).

It can be seen from Eqn. 3.16 that the locomotive force is the rate of change of the two momentum terms in the parenthesis. The first term

$$\mathbf{I}_1 = \rho \int_{V_V} \mathbf{u} dV \tag{3.17}$$

is the linear momentum of the fluid inside the vortex, whereas the second term

$$\mathbf{I}_2 = -\rho \int_{S_V} \phi \mathbf{n} dS \tag{3.18}$$

is the momentum of the surrounding fluid due to the motion and deformation of the vortex. These two terms were evaluated at each time step and the locomotive force was calculated as the rate of change of the total momentum.

3.3.4 Approximation

Quantification of the momentum of the wake vortex from Eqn. 3.16 requires 3-D geometry and kinematics of the vortex boundary information. However, because only 2-D DPIV velocity data was available, the LCS could only provide the vortex boundary on the transverse plane. Therefore, approximations and simplifications were made when necessary.

First, the 2-D vortex boundary on the transverse plane was used to construct the 3-D geometry of the vortex. It has been shown in a previous study (Drucker and Lauder, 1999) that an isolated vortex ring is generated by the pectoral fin of the bluegill sunfish during labriform fin kinematics. To approximate the 3-D shape of the vortex, the calculated vortex boundary on the transverse plane was first mapped into an ellipse, which represents the cross-section of the vortex ring in its middle transverse plane (Fig. 3.4). The calculated vortex boundary and the model ellipse have the same long axis length and also the same width. Assuming the elliptical vortex cross-section was perpendicular to and symmetrical about the transverse plane, it was revolved around its axis to generate the 3-D ellipsoidal vortex ring.

The momentum of the fluid inside the vortex $\mathbf{I}_1$ can be simplified as:

$$\mathbf{I}_1 = \rho \int_{V_V} \mathbf{u} dV \simeq \rho V_V \mathbf{U}_V, \tag{3.19}$$

where ρ is water density (1000 kg m^{-3} at 20 ^{o}C), $\mathbf{U}_V$ the velocity of the wake vortex's center of mass, and V_V the volume of the vortex.

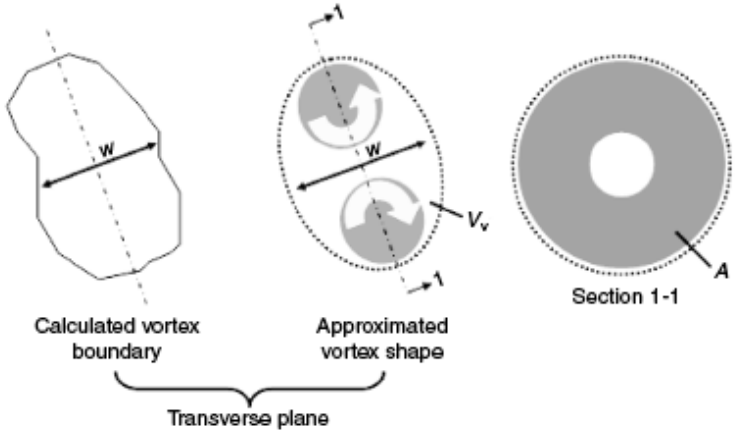

Figure 3.4: Schematic of the approximation of the vortex volume. The calculated vortex boundary on the transverse plane was modeled by an ellipse, which represents the cross-section of the vortex in the transverse plane. The calculated vortex boundary and the model ellipse have the same long axis length and also the same width. The long axes of the calculated boundary and the approximated shape are parallel. The volume of the vortex is approximated by the product of the center-width w of the vortex in the laser plane view and the projected area A of the vortex ring onto a plane perpendicular to the laser sheet.

Based on the expression of fluid potential ϕ (Eqn. 3.12), evaluation of momentum $\mathbf{I}_2$ requires 3-D kinematics on translation, rotation, and deformation of the vortex boundary. For the purpose of demonstration in this study, the rotation and deformation of the vortex boundary were neglected because it was difficult to obtain accurate 3-D information. When only fluid potential ϕ due to translation of the vortex was considered, i.e., $\phi = \mathbf{U} \cdot \Phi$, momentum $\mathbf{I}_2$ was given by

$$\mathbf{I}_2 = -\rho \int_{S_V} \mathbf{U} \cdot \mathbf{\Phi} \mathbf{n} dS = -\rho \mathbf{U} \cdot \int_{S_V} \mathbf{\Phi} \mathbf{n} dS. \tag{3.20}$$

The integration of the translational Kirchhoff potential $\mathbf{\Phi}$ over surface of a body is the added-mass of that body, i.e.,

$$\mathbf{A}_V = -\int_S \mathbf{\Phi} \mathbf{n} dS. \tag{3.21}$$

Thus the momentum $\mathbf{I}_2$ is the momentum of the vortex added-mass, i.e., the fluid induced by the motion of the vortex,

$$\mathbf{I}_2 = \rho \mathbf{U} \cdot \mathbf{A}_V. \tag{3.22}$$

Furthermore, the momentum of the wake vortex added-mass can be approximated based on the added-mass tensor $\mathbf{C}_{AM}$ of the vortex, as well as the volume and velocity of each vortex as it is formed in the wake:

$$\mathbf{I}_2 = \rho V_V \mathbf{U}_V \cdot \mathbf{C}_{AM}. \tag{3.23}$$

The added-mass coefficient tensor $\mathbf{C}_{AM}$ is a 3×3 matrix whose elements c_{ij} are the dimensionless added-mass coefficients that relate linear acceleration in the ith direction to the resultant forces in the jth direction (where i and j can assume x-, y- and z-axis directions. Repeated subscripts c_{ii} do not indicate summation). Because the vortex is approximated by an ellipsoid, the off-diagonal elements of the added-mass tensor $\mathbf{C}_{AM}$ are zero due to symmetry. Also, a previous study (Drucker and Lauder, 1999) has shown that the vortex ring attached to the sunfish pectoral fin mostly moves along its axis of symmetry. Therefore, the added-mass effect is assumed to be dominated by only one single component corresponding that direction. The total impulse $\mathbf{I}$ of the moving vortex can then be simplified as:

$$\mathbf{I} = \mathbf{I}_1 + \mathbf{I}_2 = \rho V_V \mathbf{U}_V + \rho V_V C \mathbf{U}_V, \tag{3.24}$$

where the scalar C represents the added-mass coefficient for linear motion along the direction of $\mathbf{U}_V$. Therefore, the locomotive force exerted by the fluid on the fin is equal and opposite to the rate at which the total momentum $\mathbf{I}$ changes due to the interaction between the fluid and the fin is:

$$\mathbf{F}_L = -\frac{\partial \mathbf{I}}{\partial t} = -\rho \frac{\partial}{\partial t}[(1 + C) V_V \mathbf{U}_V)]. \tag{3.25}$$

The three parameters C, V_V and $\mathbf{U}_V$ were all evaluated from the vortex boundary information obtained from the LCS analysis. The added-mass coefficient C of the vortex body can be determined from an equivalent solid body calculation of the approximated 3-D ellipsoidal vortex shape (Milne-

Thomson, 1960). For an ellipsoid

$$\frac{x^2}{a^2} + \frac{y^2}{b^2} + \frac{z^2}{c^2} = 1, \tag{3.26}$$

the added-mass coefficient for moving along its a-axis is expressed as

$$C = \frac{\alpha}{2 - \alpha}, \tag{3.27}$$

with

$$\alpha = abc \int_0^\infty \frac{d\lambda}{(a^2 + \lambda)^{3/2}(b^2 + \lambda)^{1/2}(c^2 + \lambda)^{1/2}}. \tag{3.28}$$

The vortex volume V_V was approximated by $V_V \simeq wA$, where w is the width of the wake vortex on the laser plane view and A is the projected area of the vortex ring on the plane perpendicular to the transverse plane (Fig. 3.4). The projection of the vortex body velocity $\mathbf{U}_V$ on the transverse plane was approximated by the velocity of the centroid of the area inside the 2-D vortex boundary. Since the velocity component perpendicular to the transverse plane was not available, the locomotive forces in that direction (thrust) were not evaluated. So only lift (vertical) and lateral (horizontal) forces were evaluated.

3.4 Results

3.4.1 Vortex Flow Patterns

A stroke cycle of labriform locomotion for the *Lepomis macrochirus* individuals tested lasts approximately 600 milliseconds in ambient flow of 0.5 $L \cdot s^{-1}$. It involves an oscillatory cycle of (1) anteroventral fin movement (downstroke, $t = 0 - 250$ ms, with time $t = 0$ corresponding to the initialization of fin movement in downstroke), (2) rotation of the fin around its long axis at the end of downstroke (stroke reversal, or fin flip, $t = 250 - 300$ ms), (3) posterodorsal fin movement (upstroke, $t = 300 - 550$ ms), and (4) a kinematic pause period during which the fin is held flush

against the body ($t = 550 - 600$ ms).

The velocity field in the transverse plane and the corresponding vorticity component calculated from the velocity field are plotted in Fig. 3.5 at four instants during the stroke cycle. In the transverse plane, a discrete pair of counter-rotating vortices is seen during the downstroke, indicating a vortex ring in 3-D. One vortex core is located near the dorsal edge of the pectoral fin while the other is near the ventral edges of the fin; the cores possess vorticity of opposite signs (Fig. 3.5A). A jet-like flow passes between the vortex pair. At the end of the downstroke, the vortex pair appears to contract, giving a vortex structure with a smaller diameter (Fig. 3.5B). As the upstroke begins, the vortex generated in the downstroke sheds from the fin while a new vortex becomes visible at the dorsal tip of the fin (Fig. 3.5C). Later in the upstroke, the vorticity map becomes complicated and it is difficult to identify a coherent vortex structure (Fig. 3.5D).

3.4.2 LCS and Vortex Boundary

In Fig. 3.6 color contour plots of the FTLE fields computed with integration times of $T = -200$ ms and $T = 200$ ms at the arbitrary time $t = 250$ ms are superimposed on the velocity map at the same instant in time. The ridges of high FTLE values in each plot indicate LCS. For Fig. 3.6A, the FTLE is a backward-time FTLE with $T < 0$, showing an attracting LCS; and for Fig. 3.6B, the FTLE is a forward-time FTLE with $T > 0$, showing a repelling LCS. The FTLE fields shown in Fig. 3.6 do not give a vortex boundary that is as sharply defined as in previous studies of isolated vortex rings (cf. Figs. 2.3 and 2.4). This is due to the aforementioned limitation in integration time $|T|$. Nonetheless, the location of the LCS can still be approximated to lie at the centerline of the FTLE contours in each frame. The repelling and attracting LCS derived from Fig. 3.6 are plotted together to give the vortex boundary in Fig. 3.7. A best-fit spline connection was used if the repelling and attracting LCS did not intersect in a given frame. Ideally the repelling and attracting LCS should always completely intersect to give a well-defined wake vortex boundary when a wake vortex is present (Shadden et al., 2006; also cf. Figs. 2.3 and 2.4). However, due to the aforementioned short integration time, in some frames less of the boundary is revealed by the LCS. In Fig. 3.7, the

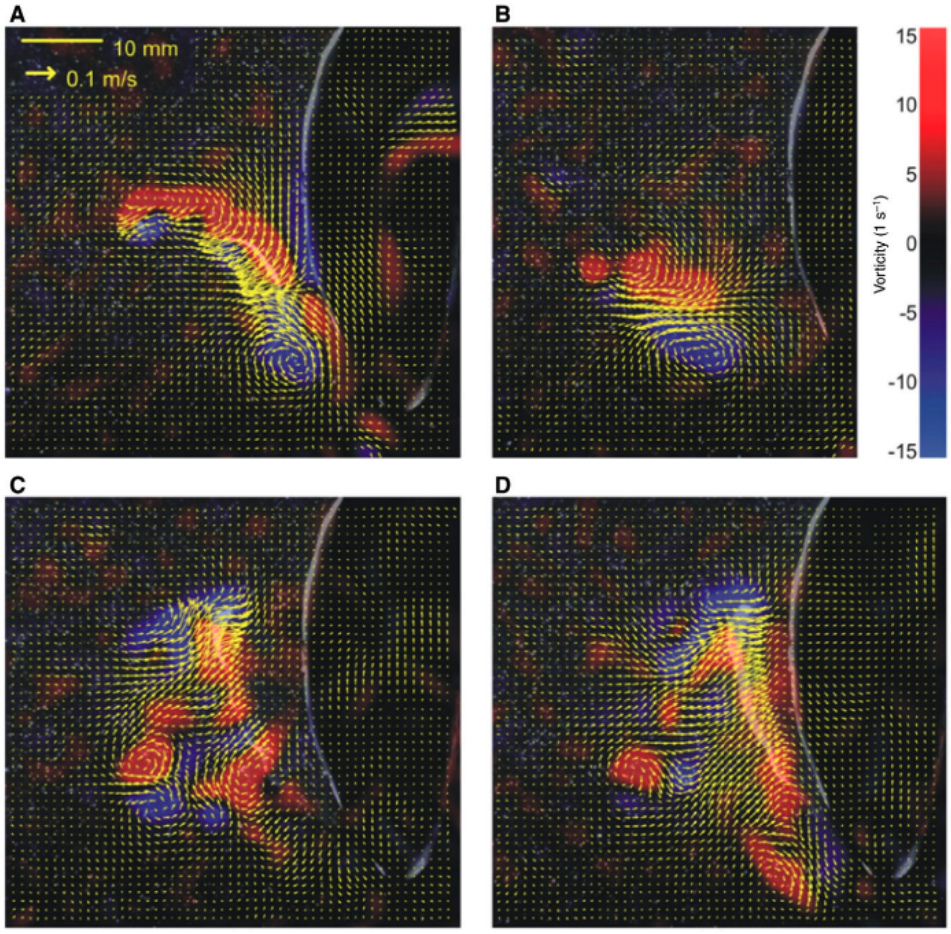

Figure 3.5: Velocity and vorticity fields of the pectoral fin wake in the transverse plane. (A) Early ownstroke; (B) late downstroke and stroke reverse; (C) early upstroke; (D) late upstroke. Red colors represent negative or clockwise fluid rotation, while blue colors indicate positive vorticity or counterclockwise fluid rotation. The camera recorded a posterior view of the left pectoral fin and the fish body.

boundary of the vortex at the transverse plane is superimposed on the DPIV velocity field data at $t = 250$ ms. Notice that it is impossible to define a vortex boundary from inspection of the velocity or vorticity field alone, whereas the theory governing the LCS ensures that the boundary is captured by the present FTLE measurements (Shadden et al., 2005 and 2006).

The boundary of the vortex on the transverse plane does not have a regular elliptic shape, a possibility anticipated in the previous section. The fin (the portion with high brightness alongside the sunfish body in Fig. 3.7) can be seen embedded inside the vortex, i.e., the shape of the vortex corresponds to the shape and location of the fin. The result, that the fin is enclosed in the vortex,

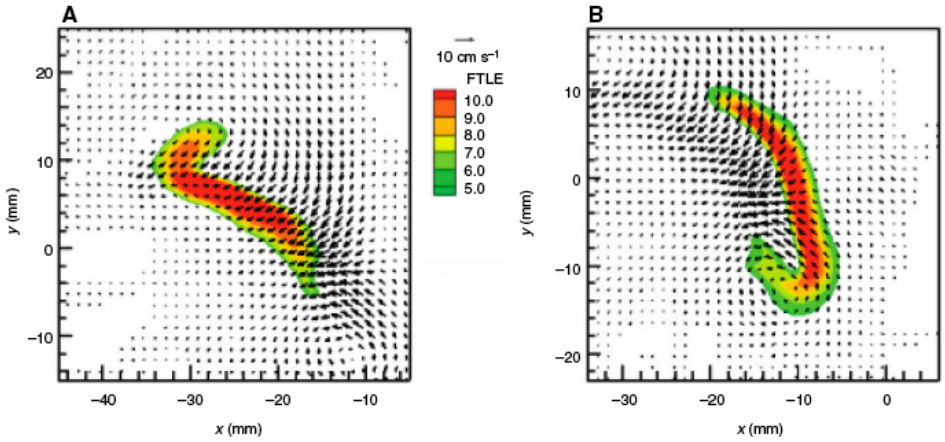

Figure 3.6: A snapshot of color contour plots of the FTLE fields computed from DPIV. (A) Backward FTLE; (B) forward FTLE. Position coordinates are specified in mm.

is consistent with the fact that the pair vortices of the vortex ring are generated at the dorsal and the ventral edges of the fin.

3.4.3 Time Evolution of the Vortex

The FTLE fields were calculated at a series of discrete time instants during the fin stroke cycle ($t = 100 - 400$ ms), with time interval between consecutive time instants $t = 10$ ms. The LCS could not be determined for the very early part of the downstroke ($t = 0 - 100$ ms), when insufficient DPIV data was available to determine the backward time structure (i.e., no data is available before $t = 0$, preventing knowledge of fluid particle behavior for backward integration times T such that $t - |T| < 0$; $T = t$ was used for $t = 100 - 200$ ms and $T = 200$ ms for elsewhere). Neither was the LCS determined for the upstroke ($t = 400 - 600$ ms), during which increasing three-dimensionality of the wake limited the fluid particle behavior that could be deduced from DPIV data in the 2-D transverse plane. The LCS was calculated on the time span from $t = 100 - 400$ ms, during which an isolated vortex pair can be clearly seen on the vorticity map. This time span covers most of the downstroke and the stroke reversal. The time evolution of the vortex boundary is plotted in Fig. 3.8. It can be seen that the shape of the vortex boundary changes with time. Compared with the early portion of the downstroke, the projection of the vortex on the transverse plane becomes wider,

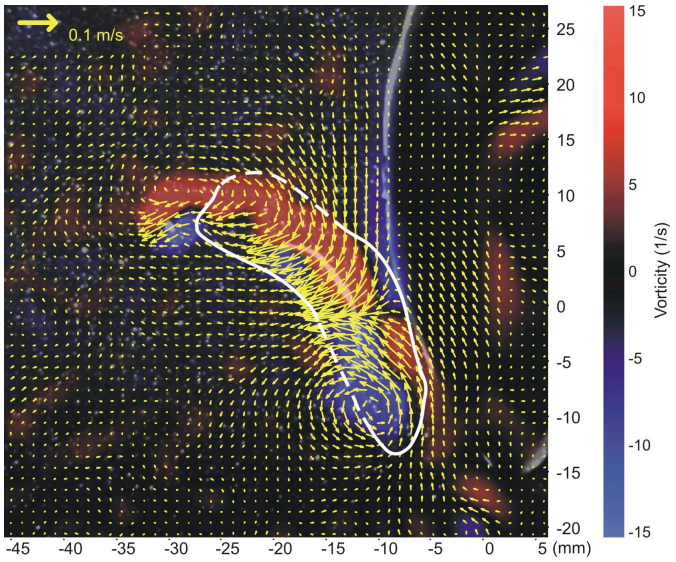

Figure 3.7: The boundary of the vortex derived from LCS. The left solid line shows the attracting LCS from backward FTLE calculation while the right-hand-side solid line shows the repelling LCS from forward FTLE calculation. Broken lines are spline lines connecting the LCS. The fin (the curve with high brightness inside the lines) can be seen embedded inside the vortex. The attracting and repelling LCS do not intersect to give the entire vortex boundary because of the limitation in integration time T.

suggesting that the pair of vortices move closer to each other during the late downstroke, or that the vortex pair is advected out of the plane of the laser sheet, or a combination of these two effects.

The position of the projection of the vortex centroid on the transverse plane was determined by calculating the centroid of the area enclosed in the vortex boundary. The trajectory of the projected vortex centroid on the transverse plane is plotted in Fig. 3.9. The movement of the vortex is consistent with the fin kinematics. The velocity of the projected vortex centroid on the transverse plane was calculated from the trajectory by the change of position in unit time (Fig. 3.10). It can be seen from the velocity profile that during the downstroke, the vortex accelerates vertically most significantly during $t = 100 - 150$ ms and accelerates horizontally most significantly during $t = 160 - 210$ ms. It will be shown later that this pattern of movement plays a major role in the force generation.

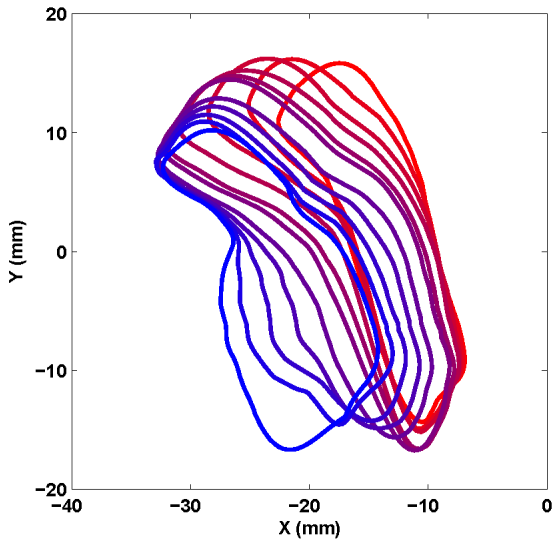

Figure 3.8: Time evolution of the vortex boundary. Vortex boundaries at 11 different time instances are plotted from red to blue with a time interval of 30ms.

3.4.4 Vortex Geometry

The LCS show the boundary of the vortex on the 2-D transverse plane where DPIV data were taken. As mentioned previously, the 3-D shape of the vortex was derived from the 2-D boundary. Since the boundary has an irregular shape, it was approximated by an ellipse to construct the 3-D vortex shape. The time evolutions of the volume, the width and the area of the vortex (all defined previously and shown in Figs. 3.3 and 3.4) are plotted in Fig. 3.11A-C. The volume of the vortex remains relatively constant during the early part of the downstroke and begins to decrease significantly in the latter part of the downstroke and the stroke reversal. This effect, which may be an artifact of planar measurement of a 3-D flow, is examined more closely in the Discussion.

3.4.5 Vortex Added-mass

The added-mass coefficient of the vortex was determined by the approximated 3-D shape of the vortex ring. The relationship between added-mass coefficient and time is plotted in Fig. 3.11D. In the early part of the downstroke, the vortex resembles a relatively oblate disk, giving a larger added-mass coefficient, while in the latter part of the downstroke, the vortex is more sphere-like,

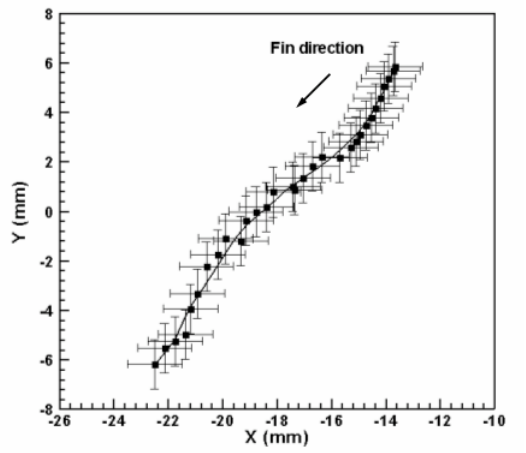

Figure 3.9: Trajectory of the projection of the vortex centroid on the transverse plane. Squares: calculated data at each time instance. Solid line: spline fitting of the data using a centered moving average method with a span of five data points. Error bars indicate measurement uncertainty.

giving an added-mass coefficient with a value approaching 0.5, which is the added-mass coefficient of a sphere. Since the added-mass coefficient is determined by the shape of the vortex, it follows the change in vortex shape closely.

3.4.6 Locomotive Force

The forces exerted by the fluid on the pectoral fin over the time span of interest are plotted in Fig. 3.12, with horizontal component (lateral force) and vertical component (lift force) separated. Also plotted are the time-averaged forces calculated using the vorticity method (Drucker and Lauder, 1999). The positive horizontal force is directed toward the body while the positive vertical force is directed upward. The data indicate that at the early downstroke there is a relatively large lateral force in the direction opposite to the fin movement. The fin also generates a significant lift at the early downstroke. In the late part of the downstroke, the horizontal force is close to zero and the magnitude of the vertical force also becomes much smaller than it was in the early part of the downstroke.

There is a phase difference between when lift force and lateral force are generated during the downstroke. Comparing Fig. 3.11A with Fig. 3.11B, it is apparent that the fin generates significant lift (at $t = 100 - 160$ ms) before it generates lateral force (at $t = 160 - 210$ ms). This effect arises

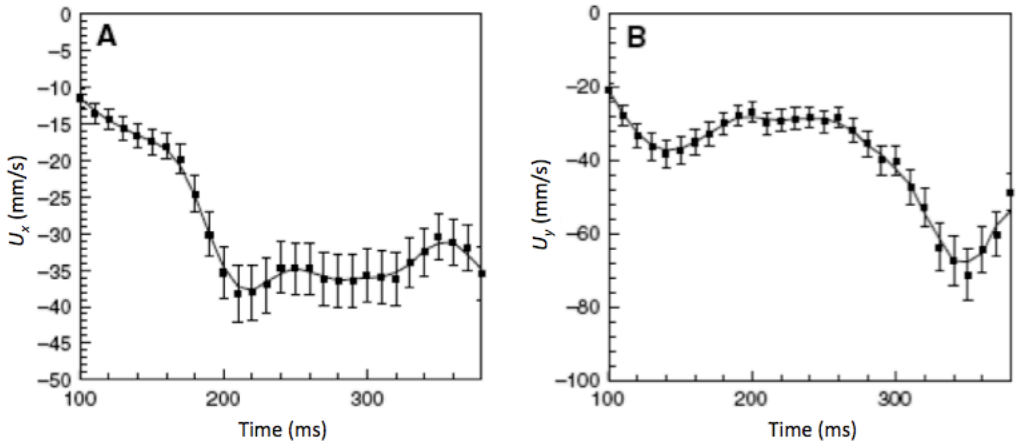

Figure 3.10: The velocity of the projection of the vortex centroid on the transverse plane. (A) Horizontal component U_x; (B) vertical component U_y. Squares: calculated data at each time instance. Solid line: spline fitting of the data using a centered moving average method with a span of five data points. Error bars indicate measurement uncertainty. Note that due to limitations on FTLE integration time, these plots are for $t = 100 - 380$ ms of a 600 ms fin stroke cycle.

because the acceleration of the vortex in the vertical direction occurs prior to its acceleration in the horizontal direction (Fig. 3.10).

3.5 Discussion

In this study, a framework is developed to combine the LCS analysis with a potential flow, deformable body theory to study dynamics of wake vortex and to evaluate locomotive forces. The LCS analysis provides the boundary information of wake vortex, and therefore enables analyzing the wake vortex as a distinct fluid structure with its own added-mass dynamics. In the case study of bluegill sunfish pectoral fin locomotion, the time-resolved vortex boundary information is identified from the DPIV measurements. The momentum of the vortex in animal wake is evaluated as the sum of the linear momentum of fluid inside the vortex and the linear momentum of fluid surrounding the wake vortex, i.e., the added-mass of the wake vortex. Quantification of the momentum leads to the evaluation of instantaneous locomotive forces.

As mentioned previously, the present approach relies on the assumption that there is no vorticity on or external to the LCS boundary, so that the shear stresses on the LCS surface are negligible.

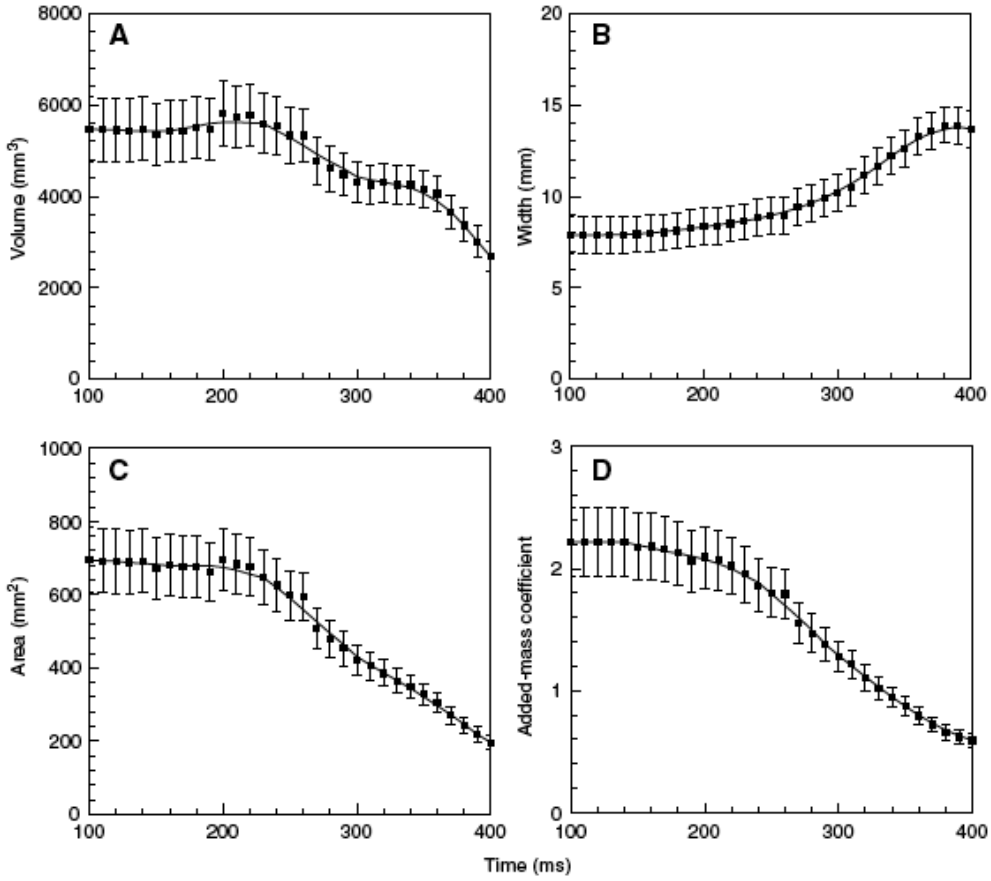

Figure 3.11: (A) Volume of the vortex; (B) width of the vortex; (C) cross-sectional area of the vortex; and (D) added-mass coefficient of the vortex. Squares: calculated data at each time instance. Solid line: spline fitting of the data using a centered moving average method with a span of five data points. Error bars indicate measurement uncertainty.

This hypothesis can be tested directly, based on the measured velocity field data, by calculating the shear stress on the surface $S(t)$ of the LCS and comparing this with the computed locomotive force $\mathbf{F}_L$. The total shear stress is calculated by integrating shear tensor $\boldsymbol{\tau}$ on the LCS in the 2-D transverse plane and then multiplied by the depth of the vortex ellipsoid. The ratio of the absolute values of the two is evaluated and shown in Fig. 3.13. The shear on the LCS is small relative to the locomotive force, consistent with the potential flow hypothesis. The local peak in the pectoral fin data is attributable to vorticity outside the dorsal edge of the LCS, as seen in Fig. 3.7. This vorticity external to the LCS causes the potential flow hypothesis to break down locally. As to the reasons that there is some vorticity outside the vortex boundary defined by the LCS, one of them

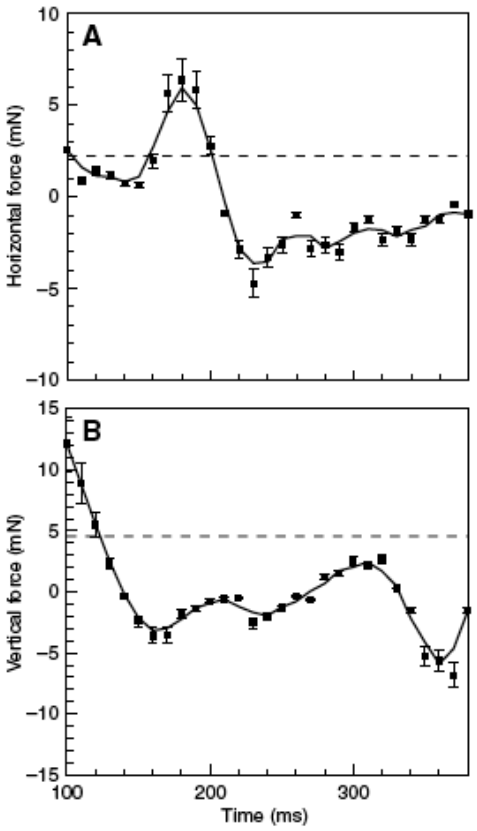

Figure 3.12: The locomotive force (mN) in (A) the horizontal and (B) the vertical directions. Squares: calculated locomotive forces. Solid line: spline fitting of the data using a centered moving average method with a span of five data points. Error bars indicate measurement uncertainty. Broken line: time-averaged forces calculated using the vorticity method (Drucker and Lauder, 1999).

might be the error in calculation of LCS due to the rather short integration time. Also, viscous diffusion occurring at finite Reynolds numbers enables vorticity to cross the flow boundaries defined by the LCS, even when these boundaries form barriers to fluid transport. A similar effect has been observed in studies of isolated vortex rings (Dabiri and Gharib, 2004; Shadden et al., 2006). Another reason is the appendage rotation, e.g., the anteroventral rotation of the sunfish pectoral fin during its downstroke. Haller (Haller, 2005) has shown that in flows with global rotation, the vorticity field can be a poor indicator of vortex boundaries. Hence, in these unsteady flows it is possible to lose a strict correlation between the wake vortex boundary dictated by the LCS and the spatial distribution of vorticity. The quantitative effect of vorticity outside LCS on the validity of the potential flow hypothesis requires further studies.

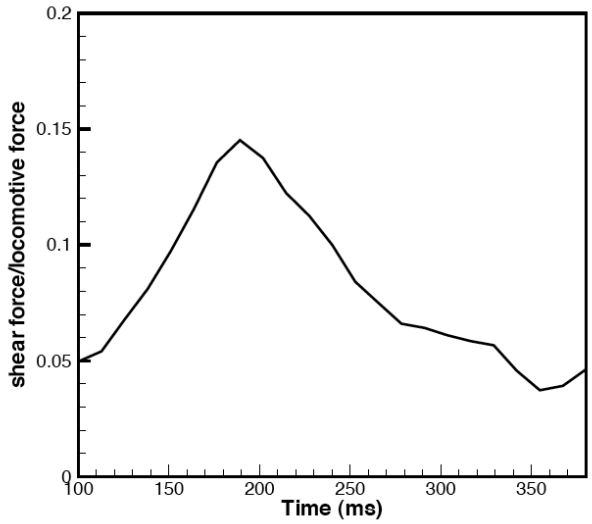

Figure 3.13: Ratio of the shear force on LCS surface to the magnitude of the locomotive force.

The fin of the bluegill sunfish was observed to be embedded within this vortex wake structure. It is expected that a similar phenomenon will observed for other animal appendages moving in air or water. This result suggests that the dynamical effect of the vortex wake on locomotion is to replace the real animal fin with an 'effective appendage', whose geometry is dictated by the LCS and whose dynamics are described by the deformable body theory. A similar concept, the 'displacement thickness', is well-known in the theory of steady aero- and hydrodynamic flows (e.g., Rosenhead, 1963). The benefit of this approach, based on an 'effective appendage', is that it facilitates a direct correlation between the morphology and kinematics of the real appendage and the dynamics of locomotion.

The simplified form for the locomotive force (Eqn. 3.25) has the same expression as in Dabiri (2005 and 2006), in which hydrodynamical forces acting on a vortex were derived from vortex impulse. Eqn. 3.25 indicates that there are three parameters contributing to the force generation: the vortex added-mass coefficient C, volume V_V, and velocity U_V of the wake vortex body. Of these three parameters, C and V_V are more directly related to the geometry of the vortex while U_V is more closely related to the fin motion. Since locomotive forces are generated proportionally to the change of momentum $[(1+C)V_V U_V]$ in unit time, the contribution of each parameter can be evaluated by

comparing the three logarithmic terms on the right-hand side of the following equation:

$$\Delta log[(1+C)V_V U_V] = \Delta log(1+C) + \Delta log V_V + \Delta log U_V . \tag{3.29}$$

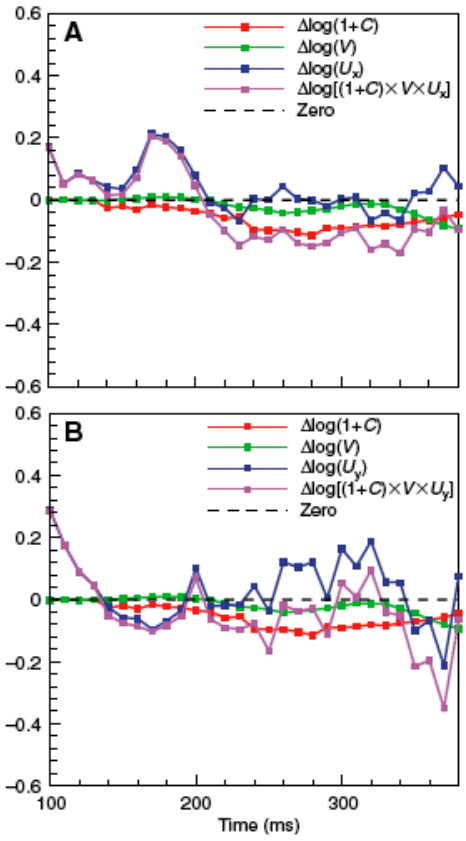

Figure 3.14: Analysis of the contributing factors to the locomotive force. (A) Horizontal direction; (B) vertical direction. The changes in the logarithm of each parameter to the vortex momentum are plotted as well as the total change in the vortex momentum, in order to determine the most dominant contributing parameters to the change in momentum.

Figure 3.14 shows the change of the logarithm of each individual parameter and the total change in wake momentum. It can be seen that early in the stroke cycle, the changes in the shape of the vortex are small and the total change in momentum follows closely the change in vortex velocity. As mentioned previously, the vortex velocity closely follows the fin motion during this stage of the stroke cycle. Therefore, force production during the early fin motion is primarily dependent on the fin kinematics. After the initial fin motion, force generation is primarily dictated by changes in the

vortex shape; hence, fin morphology (which dictates vortex shape) governs force production later in the fin stroke cycle. Analyses of the vertical and horizontal forces are consistent, showing that the shape of the vortex remains relatively constant early in the stroke cycle but changes in the latter stages. Therefore the results imply that locomotive forces can be generated not only by accelerating or decelerating the fin, but also by changing the shape of the vortex via fin morphology. The clarity of the relationship of the parameters in Fig. 3.13 is a benefit of the 'effective appendage' approach taken in the present study. Since the timing of forces on the 'effective appendage' is coincident with those on the real appendage (i.e., instantaneous forces are being evaluated), this perspective is compatible with investigation of muscle dynamics and activity patterns (Lauder et al., 2007; Mittal et al., 2007).

In this study, locomotive force is quantified only on the downstroke and early portions of the stroke reversal, when there is a single vortex structure primarily attached to the fin. The forces estimated are consistent with the magnitude of the time-averaged forces calculated using the same vorticity method as in Drucker and Lauder (1999). The time-averaged vertical and lateral forces are 2.23 mN and 4.55 mN for this study (Fig. 3.12), which are consistent with the time-averaged forces quantified in Drucker and Lauder (1999) for the same species (3.24 mN vertical and 6.96 mN lateral), noting that the data used in that study were taken from a different animal sample and using a different experimental arrangement. The evolution of forces is consistent with the motion of the animal. The lateral forces from the paired pectoral fins are expected to approximately cancel, resulting in the absence of substantial lateral motion as was observed empirically. The resultant vertical force, i.e., lift minus weight, is positive during the early phase but negative during the later phase, consistent with the kinematic measurements of Gibb et al. (1994). Since it only presents kinematic descriptions of the animal locomotion (i.e., no force measurements), the comparison that can be made with the present work is only qualitative. Nonetheless, the force peaks in Fig. 3.12 are suggestive of a rise during the early phase of the fin beat and sinking during the late phase, as seen by Gibb et al. (1994). Perhaps coincidentally, the evolution of the locomotive forces resembles the pattern of forces generated by an insect wing, which has an early peak when the wing starts from

rest followed by decay to a stable level (Birch and Dickinson, 2003).

The greatest challenge in this study was to identify the 3-D boundary of the vortex and its motion given 2-D planar DPIV data. As seen from Eqn 3.16, only by identifying the 3-D boundary of the vortex can the locomotive force be precisely evaluated. Since only 2-D velocity data are available in the present study, approximations were required. The fluid potential due to vortex rotation and pure deformation was neglected in this study, because it was difficult to evaluate with accuracy in 3-D. From the evolution of vortex boundary (Fig. 3.8), it can be seen that there is no significant rotation. The deformation too is relatively small, except during the later phase.

A concern in the calculations is the assumption that the vortex ring is symmetrical about the transverse laser plane. This may not be true during the entire stroke cycle, and an asymmetrical distribution of the vortex ring on either side of the laser plane would cause under-estimation of the vortex volume. Since the vortex cannot move far from the laser plane as long as it is attached to the fin, which is oscillating near the laser plane, the approximation used in this study for the attached vortex is reasonable. However, after the vortex is shed from the fin, it is advected out of the laser plane by the ambient current, making the approximation invalid. This is likely the effect observed toward the end of the present measurements (e.g., Fig. 3.11A,C).

Attempts were made to increase the accuracy of the 3-D vortex boundary approximation. FTLE fields were calculated on horizontal planes from DPIV data, with the aim of identifying the vortex boundary corresponding to the transverse plane measurement and thereby constructing the 3-D vortex boundary. However, boundaries were not clearly revealed in the corresponding FTLE fields due to the effect of net ambient flow on these two planes, which dominated the vortical motions. Even if it is possible to identify the boundary of the vortex on three perpendicular planes, approximation is still required to construct the 3-D boundary of the vortex (though the result may exhibit higher accuracy than the present methods when measuring more complex wake geometries). The identification of 3-D vortex boundaries would also enable evaluation of the effect of rotational added-mass, which is neglected in the present study. The determination of the 3-D vortex boundary requires the development of flow visualization techniques or numerical methods that can provide 3-D velocity

field information, which can then be analyzed using the LCS analysis implemented in this study.

Given volumetric DPIV data for swimming or flying animals (or corresponding data computed in numerical simulations), a true validation of non-invasive force measurements demands a comparison of the animal body trajectory predicted by the force measurements with the body trajectory measured empirically. To our knowledge, such a comparison of measured and predicted kinematic data has not yet been performed by any study. Ideally, wake vortex dynamics and body kinematics should be measured simultaneously and in three dimensions. A demonstration that the estimated forces agree with the time-averaged force required to sustain lift of neutral buoyancy is necessary, but not sufficient by itself to validate instantaneous force estimates (cf. Dabiri, 2005). An additional avenue for validation would be comparison of calculated force profiles with those resulting from computational fluid dynamic analysis of the same fin beats using measured 3-D kinematics from that beat (with coupled fluid-structure interactions included in the computation for the swimming case, due to the comparable density of the fluid medium and the appendage). Once the force model has been validated, other aspects of animal behavior such as energetics can be examined according to established models (e.g., Schultz and Webb, 2002).

To be sure, the present approach requires the extraction of fluid particle trajectories, information that has been derived here from Eulerian velocity data from DPIV measurements. In principle, it would be more efficient to extract these trajectories empirically, as in particle-tracking velocimetry (PTV) techniques. However, PTV methods are most effective in flows with relatively low seeding densities, typically at least an order of magnitude less than DPIV. Computing the FTLE fields would then require substantial interpolation of the measured fluid particle trajectories. One potential advantage of this approach, however, is that three-dimensional PTV can be implemented with substantially greater ease than an equivalent DPIV technique. Furthermore, PTV has experienced significant refinements recently (e.g., Pereira et al., 2006). The extraction of three-dimensional fluid dynamics from animal swimming measurements may be facilitated by the use of PTV within the context of this method.

3.6 Acknowledgements

The author thanks Dr. George Lauder and Dr. Peter Madden for collaborating on this study.

Chapter 4

'Upstream Structure' and Propulsive Efficiency

4.1 Summary

The interaction between swimming and flying animals and their fluid environments generates downstream wake structures such as vortices, which are the focus of many animal-fluid interaction studies. In most studies, the upstream flow in front of the animal is neglected. In this study, the LCS analysis is used to demonstrate the existence of 'upstream fluid structures' even though the upstream flow is quiescent or possesses a uniform incoming velocity. This type of upstream structure is not visualized by Eulerian velocity or vorticity fields, or passive flow markers (dye, smoke, etc). Rather, it is retrospectively identified by tracking the fluid that interacts with the swimmer. Using a computational model, the flow generated by a swimmer (an oscillating thin flexible plate) is simulated and the LCS analysis is applied to the flow to identify the upstream fluid structures. These upstream structures show the exact portion of fluid that later interacts with the swimmer. A mass flow rate and a momentum flux are then defined based on the upstream structures and a metric for propulsive efficiency is established. The unsteady mass flow rate defined by the upstream fluid structures can be used as a metric to measure and compare the efficiency of locomotion in water and air.

4.2 Introduction

As a swimming or flying animal moves through its environment, the surrounding water or air is disturbed, resulting in currents of rotating fluid that are left behind in the animals wake. Over the past several decades, studies of fish swimming (Muller et al., 1997; Drucker and Lauder, 1999; Liao et al., 2003; Wilga and Lauder, 2004; Bartol et al., 2005; Tytell, 2007); bird, bat, and insect flight (Ellington et al., 1996; Dickinson et al., 1999; Spedding et al., 2003; Videler et al., 2004; Warrick et al., 2005; Tian et al., 2006; Hedenstrom et al., 2007; Wang, 2005); and many other modes of locomotion (Nauwelaerts, et al., 2005; Dabiri et al., 2006) have used animal wakes to infer the physical mechanisms governing swimming and flying. However, in each case the focus has been primarily on flow features near the animal appendages or downstream from the animal, based on the assumption that the upstream flow in front of the animal is trivial.

From a dynamical point of view, this is true if the upstream flow is quiescent or has uniform incoming velocity. Because there is no animal-fluid interaction occurring upstream until very close to the swimmer, there are no informative dynamical structures that can be used to study animal-fluid interaction when the upstream fluid is visualized by Eulerian properties such as velocity, vorticity, or streamline plots.

However, LCS analysis, which is from a Lagrangian perspective, enables identification of more general types of fluid structures. These coherent structures include vortices, but are more general fluid structures that have distinct kinematics from the surrounding fluid. The technique is able to locate vortices in downstream wakes (e.g., Shadden et al., 2006); importantly, it also identifies fluid structures in the upstream flow that indicate distinct kinematic regions. For example, coherent fluid structures are observed upstream of a cylinder in cross-flow (Franco et al., 2007) though there is no upstream vorticity (the incoming flow is uniform). Upstream coherent structures are also seen in front of a swimming jellyfish (Shadden et al., 2006).

The identification of upstream coherent structures provides additional information regarding the fluid dynamics. Previous research has shown that these upstream structures govern fluid mass transport (Shadden et al., 2006; Franco et al., 2007). Because any mass transport is correlated

with momentum and energy transport, the LCS can also be used to quantify momentum and energy transport. Therefore, it provides a useful tool for animal locomotion studies.

The correlation between the upstream structures and the energetics of animal locomotion has not been investigated previously. In this study, a computational model is used to simulate a self-propelled undulatory swimmer and upstream fluid structures in the flow are identified using the LCS analysis. A mass flow rate and a momentum flux are then defined based on geometry of upstream structures and a metric for propulsive efficiency is established using the momentum flux and the kinematics of the swimmer. The study proposes that just as the downstream wake has been traditionally correlated to the forces and energetics of locomotion, the heretofore invisible upstream wake also exhibits dynamical significance and variation across animal species that can inform ongoing comparative biological and engineering studies of animal swimming and flying.

The outline of the study is as follows: (1) In Section 4.3 a computational model is introduced to simulate the flow field generated by an undulatory swimmer. The LCS analysis is then applied to the flow field. (2) In Section 4.4 upstream fluid structures identified by LCS are presented and their physical meanings are discussed. A mass flow rate and a momentum flux are then defined based on the upstream structures and a metric for propulsive efficiency is established using the momentum flux and the kinematics of the swimmer. (3) In Section 4.5 applications to real animal locomotion studies are discussed.

4.3 Methods

4.3.1 Computational Model

A computational model was created to provide generic locomotion kinematics for this study. The model consists of a thin flexible plate that exhibits time-periodic oscillations of its trailing edge. The shape of the flexible plate was prescribed by the tangential angle $\Psi(t, s)$ or by the lateral position $y(t, s)$ in the body frame of reference attached at its leading edge (Fig. 4.1). Three different kinematics were used in this study, all describing flapping motions. These kinematics are listed in

Table 4.1.

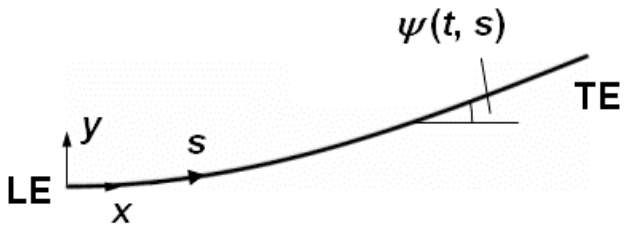

Figure 4.1: Schematic of the flexible plate model swimmer. s is the curve length and $\omega(t,s)$ is the tangential angle. LE: leading edge (s = -1); TE trailing edge (s =1).

Kinematics 1	$\Psi(t,s) = -tan^{-1}(\epsilon sin(\pi s/4)cos(2\pi ft))$
Kinematics 2	$\Psi(t,s) = \epsilon exp(2(s/L - 1/2)cos(2\pi ft))$
Kinematics 3	$y(t,s) = \epsilon exp(2(s/L - 1/2)cos(2\pi ft))$

Table 4.1: Kinematics used in the study. In these mathematical descriptions, variable t is time, f is the stroke frequency, s is the curve length on the plate (from s = -1 at the leading edge to s = 1 at the trailing edge), and ϵ is a parameter indicating the stroke amplitude.

An inviscid vortex sheet method was used to solve the flow induced by the model swimmer. It relies on calculations based on potential flow theory. However, the features of flow separation and vortex shedding are included. The vortex sheet method has been used extensively to compute separating flow past a sharp edge at high Reynolds number (Nitsche and Krasny, 1994; Jones, 2003; Shukla and Eldredge, 2007). It has been validated by comparison with experimental results in a number of previous studies (Nitsche and Krasny, 1994; Jones, 2003).

In the general case of a thin flexible plate moving in fluid, the plate was modeled as a bound vortex sheet and the separated shear layers were modeled as free vortex sheets shed at the edges of the plate. The generation of the vortex was modeled by the roll-up of the free vortex sheet (Fig. 4.2). Both the bound and free vortex sheets were discretized as a set of vortex filaments.

The flow is considered as induced by all bound and free vortex filaments. The velocity at (x,y)

Figure 4.2: A diagram of the bound vortex sheet (black solid line) on a moving flexible plate and the generated free vortex sheet (red dash line). The bound and free vortex sheets are discretized into vortex filaments (circles).

induced by a vortex filament of unit strength located at $(\tilde{x}, \tilde{y})$ has components

$$\begin{aligned} u_\delta(x, y; \tilde{x}, \tilde{y}) &= -\frac{1}{2\pi} \frac{y - \tilde{y}}{\rho^2 + \delta^2} \\ v_\delta(x, y; \tilde{x}, \tilde{y}) &= \frac{1}{2\pi} \frac{x - \tilde{x}}{\rho^2 + \delta^2}, \end{aligned} \tag{4.1}$$

where $\rho^2 = (x-\tilde{x})^2+(y-\tilde{y})^2$ and δ is the vortex-blob smoothing parameter used to regularize the roll-up of the free vortex sheet (Chorin and Bernard 1973). For vortex filaments on the free vortex sheet, a small value $\delta > 0$ (0.1 for the present study) for the vortex-blob smoothing parameter was used to evaluate their induced flow velocity. However, this parameter was set to $\delta = 0$ when evaluating the velocity induced by bound vortex filaments. The purpose of using different values of δ for free and bound vortex filaments is to prevent the motion of free vortex sheet from suffering Kelvin-Helmholtz instability and to prevent ill-conditioning when solving the equations for the bound-sheet strength (Nitsche and Krasny, 1994).

The velocity of the flow at (x, y) was obtained by summation of velocity induced by all the vortex

filament on the bound and free vortex sheets,

$$\begin{aligned} u(x,y) &= \sum_i u_\delta(x,y;\tilde{x}_i,\tilde{y}_i)\Gamma_i \\ v(x,y) &= \sum_i v_\delta(x,y;\tilde{x}_i,\tilde{y}_i)\Gamma_i, \end{aligned} \tag{4.2}$$

where i is the index corresponding to the bound and free vortex filaments, and Γ_i is the circulation on that filament.

A time-stepping procedure was used to solve vortex strength on the bound vortex sheet and to release the vortex filament into the free vortex sheet. The procedures on every time step are described as follows:

(i) Solve the strength of bound vortex sheet

The position of the bound vortex sheet was known since it coincides with that of the plate at any time t. Given the locations and strength of all free vortex filaments, the unknown bound vortex filament circulations were solved at each time step by a system of equations imposing the continuity of normal velocity on the plate, i.e., the normal flow velocity at any point on the plate, induced by all vortex filaments, was the same as the known normal velocity of the plate:

$$\mathbf{u}\cdot\mathbf{n} = \mathbf{v}_{plate}\cdot\mathbf{n}, \tag{4.3}$$

where flow velocity $\mathbf{u}$ was calculated from Eqn. 4.2 and $\mathbf{v}_{plate}$ is the plate moving velocity. Moreover, the sum of circulation on all bound and free vortex filaments satisfies Kelvin's circulation theorem.

(ii) Evaluate circulation shedding rate and introduce a new free vortex filament

In this current study, the angle of attack at the leading edge of the body is zero. Because the vortex sheet method can only be applied to separation at sharp edge, vortex shedding at the leading edge of the plate was suppressed. No free vortex sheet was generated at the leading edge; rather, a single vortex filament which remained fixed at the leading edge contained all the circulation shedded

at the leading edge.

The flow separates at the trailing edge, giving rise to free shear layers in the flow. The circulation shedding rate at the edge is

$$\frac{d\Gamma}{dt} = \frac{1}{2}(u_-^2 - u_+^2), \tag{4.4}$$

where u_- and u_+ are the slip velocities (velocity component tangential to the plate) on different sides at the edge of the plate. Due to the slip condition for the tangential velocity,

$$u_- - u_+ = \sigma_e, \tag{4.5}$$

in which σ_e is the bounded vortex sheet strength at the edge. For each time step, a vortex filament with circulation $\Gamma_i = \frac{d\Gamma}{dt}\Delta t$ was released at the trailing edge into the free vortex sheet.

(iii) Evaluate the velocity for free filaments and update their positions

Filaments on the free vortex sheet follow flow velocity. For each filament on the free vortex sheet, its velocity $(u(x,y), v(x,y))$ was evaluated by Eqn. 4.2 as the flow velocity at its current location $(x(t), y(t))$. Its new position $(x(t+\Delta T), y(t+\Delta T))$ is updated by

$$\begin{aligned} x(t+\Delta t) &= x(t) + u(x,y)\cdot\Delta t \\ y(t+\Delta t) &= y(t) + v(x,y)\cdot\Delta t. \end{aligned} \tag{4.6}$$

(iv) Evaluate the force acting on the swimmer and update its swimming speed

As viscosity is neglected in the problem, the hydrodynamic forces acting on the swimmer are normal pressure forces proportional to the pressure difference across the plate. The pressure difference across the bound vortex sheet $[p](\mathbf{x}, t)$ ([ ] indicates the discontinuity across the plate) can be

expressed as (Jones, 2003)

$$[p](\mathbf{x},t) = -\frac{d\Gamma(\mathbf{x},t)}{dt} - \sigma(\mathbf{x},t)(u(\mathbf{x},t) - \tau(\mathbf{x},t)), \tag{4.7}$$

where Γ is the circulation, σ is the vortex sheet strength, u is the tangential component of the average velocity at the bound vortex sheet, τ is the tangential component of the velocity of the plate, and $\mathbf{x}$ is the spatial coordinate. The net hydrodynamic force acting on the swimmer is therefore

$$\mathbf{F}(t) = \int [p](\mathbf{x},t)\mathbf{n}(\mathbf{x},t)dx, \tag{4.8}$$

where spatial integration over the normal direction $\mathbf{n}(\mathbf{x},t)$ is taken over the plate.

This hydrodynamical force $\mathbf{F}$ was applied to the swimmer (with unit mass per unit length) to calculate its acceleration and to determine the swimming motion. For simplicity, the lateral component of $\mathbf{F}$ was not fed back into the swimming motion so as to avoid lateral motion of the swimmer. Moreover, the net torque on the swimmer was also neglected to avoid pitching. Therefore, the motion of the swimmer is limited to streamwise and its forward motion depends only on the streamwise acceleration rate $\mathbf{a}(t) = \mathbf{F}(t)_{\text{streamwise}}/m$. The streamwise velocity of the swimmer was computed by integrating the resulting streamwise acceleration $\mathbf{a}(t)$ as

$$\mathbf{U}(t) = \int_0^t \mathbf{a}(\tau)d\tau. \tag{4.9}$$

Hence, the swimming kinematics and locomotive dynamics in the streamwise direction were fully coupled in the model.

An in-house code was developed to implement the vortex sheet method described above. The code was validated with the results from two case studies (sinusoidal oscillation with symmetric bowing and flexible flapping at zero free stream velocity) in Shukla and Eldredge (2007). Good agreements were observed in all parameters including free vortex sheet configuration, circulation

shedding rate, and force acting on the plate.

To demonstrate that the numerical method used in this study is sufficient to capture the essential features of animal locomotion in fluids, the method was used to compute the flow generated by a specific swimming mode, i.e., anguilliform swimming of an eel (Tytell, 2007). The computed flow is consistent with the result of previous DPIV measurements (Fig. 4.3), with strong lateral jets present in the wake rather than downstream jets; these lateral jets are the key characteristic of eel swimming (Tytell and Lauder, 2004). The self-propelled swimming speed is higher for the model versus the real animal (1.9 body-length/sec versus 1.5 body-length/sec), a discrepancy that can be primarily attributed to the lack of skin friction in the vortex sheet model. Despite this effect, the comparable flow kinematics support the notion that the numerical method is appropriate for this proof-of-concept analysis.

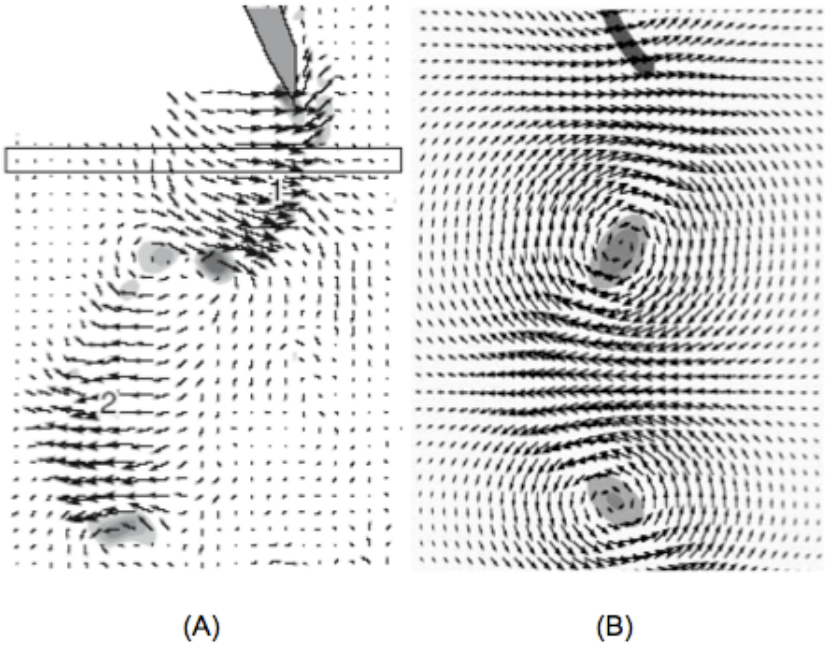

Figure 4.3: Flow fields in the wake of a free-swimming eel. (A) DPIV measurement (from Tytell, 2007); (B) simulation using the vortex sheet method. Only the tail of the eel is shown at the top of the images. Vectors: velocity field; shades: high vorticity regions. The key feature of the wake claimed by Tytell and Lauder (2004), i.e., the strong lateral jet rather than a downstream jet, is consistent between the simulation and the measurement.

4.3.2 FTLE Calculation and LCS Extraction

The flow velocity field was solved in a laboratory frame to show the self-propulsion of the swimmer. During the simulation, the vortex sheet information and the kinematics of the swimmer were recorded at each time step. Velocity fields were not recorded because they could be calculated from vortex sheet data when needed.

The calculation of FTLE is similar to that described in Chapters 2 and 3. The only difference is that when computing Lagrangian trajectories, velocity at any location was evaluated directly from vortex sheet information, rather than interpolated from a given velocity mesh. This provided higher accuracy of FTLE calculation. Also, velocity was converted to a fixed-frame attached to the leading edge of the swimmer in FTLE calculation; thus it was able to analyze the location and kinematics of LCS relative to the swimmer. The change of reference frame did not change the FTLE field, as it is independent to the choice of reference frames under linear transformations (Haller, 2002; Shadden et al., 2006). The integration time in this study was 4 stroke cycles of the swimmer, long enough to identify well-defined ridges. LCS were extracted visually from FTLE contour plots.

4.4 Results

4.4.1 Flow Fields

In this section, the flow generated by the self-propelled swimmer with kinematics 1 in Table 4.1 (with $\epsilon = 0.64$ and $f = 1$) is present. A time series of the calculated swimming motion is shown in Fig. 4.4, as well as the velocity field and vortex wake that it creates. The results are plotted in a laboratory reference frame, so the forward-motion of the swimmer is shown by its position over time. The simulated wake is consistent with previous experimental studies of similar modes of locomotion (e.g., Muller et al., 1997). As in previous studies, there is no indication of flow structure in the region upstream of the animal from this perspective.

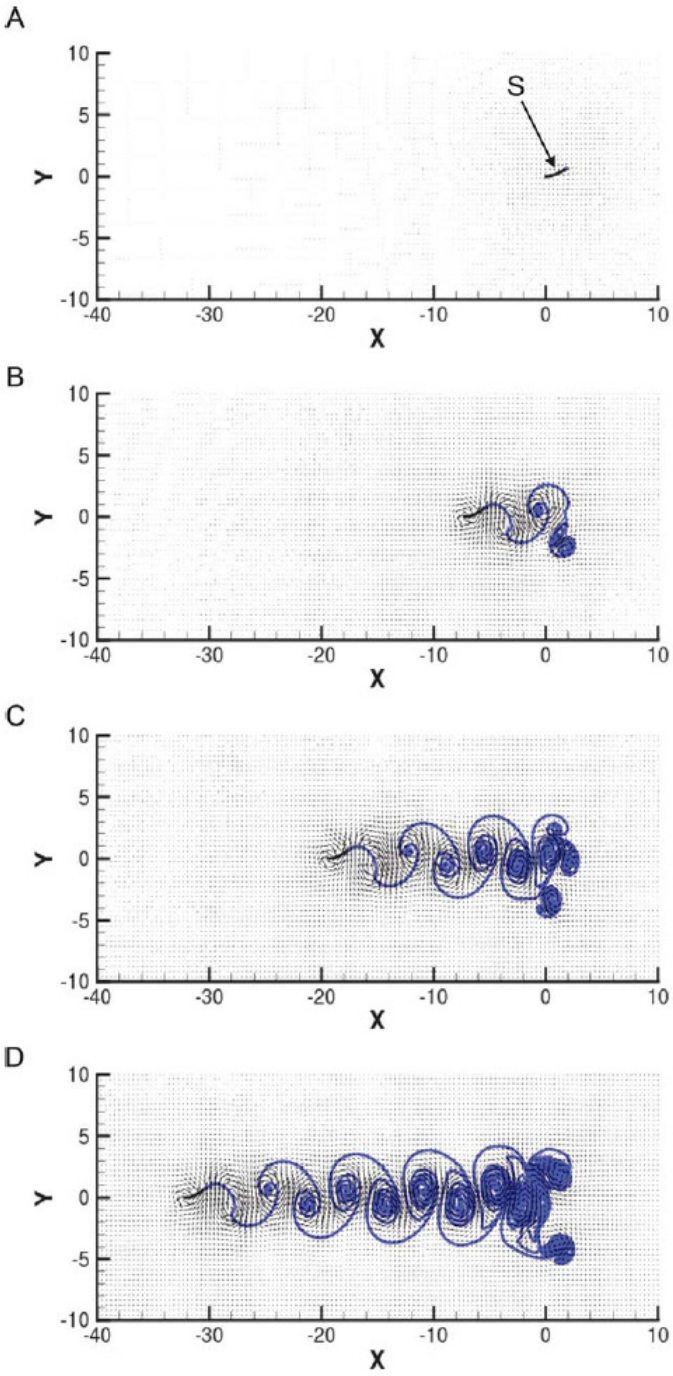

Figure 4.4: Locomotion of the model swimmer. The swimmer (S) begins at rest (A) and flaps its flexible body to propel itself forward. The vortex wake generated by the swimming motion (blue curve) and the resulting forward motion of the swimmer are shown after two (B), four (C), and six (D) swimming cycles. The swimmer moves from right to left in a laboratory reference frame. Velocity fields generated by the swimmer are also shown as vector plots.

4.4.2 Upstream Fluid Structures

In this section, the upstream structures identified by LCS analysis are present in the flow shown in Fig. 4.4. Results in this section are plotted in a reference frame fixed on the leading edge of the swimmer. Fig. 4.5A shows the backward-time FTLE field. Recall that the backward-time FTLE is computed by observing a reversed time record of the flow; the ridges of high values indicate attracting LCS. As one might expect, attracting LCS coincide with structures revealed in a dye or smoke visualization of a flow, since the fluid labeled by these flow markers will tend to align with the attracting LCS over time. Fig. 4.5A shows similar behaviour for the model swimmer. Comparison with Fig. 4.4 indicates that the attracting LCS curve is correlated with the configuration of the vortex sheet in the wake.

In contrast, Fig. 4.5B plots the forward-time FTLE computed by observing the behaviour of the flow as it evolves forward in time. The repelling LCS, located by the ridges of high forward-time FTLE values in the contour plot, are also plotted. What is immediately striking is that this flow structure extends to upstream, in front of the swimmer. In fact, the upstream extent of the repelling LCS increases as the amount of information regarding the forward-time behaviour of the flow increases, i.e., more of the upstream repelling LCS is revealed as the fluid is tracked over sufficiently long durations to observe its interaction with the swimmer (Shadden et al., 2005). The morphology of the upstream fluid structures is clearly observable.

Because fluid is not attracted to the repelling LCS (by definition), the upstream fluid structure, which is comprised of the repelling LCS, is not readily visualized using passive flow markers (i.e. dye, smoke, etc.) as is the case for the attracting LCS. In addition, since the upstream flow typically possesses a uniform or zero velocity, the repelling LCS propagates without changing its shape until after it reaches the downstream wake (Fig. 4.5B). By that point, the behaviour of the fluid around the swimmer is dominated by the nearby attracting LCS; hence the presence of the repelling LCS is obscured. It is largely for these reasons that the upstream fluid structures have not been observed previously. The present method does not rely on the aggregation of fluid to reveal the repelling LCS. Instead, it is computed based on observed fluid particle separation in the flow. To be sure, the

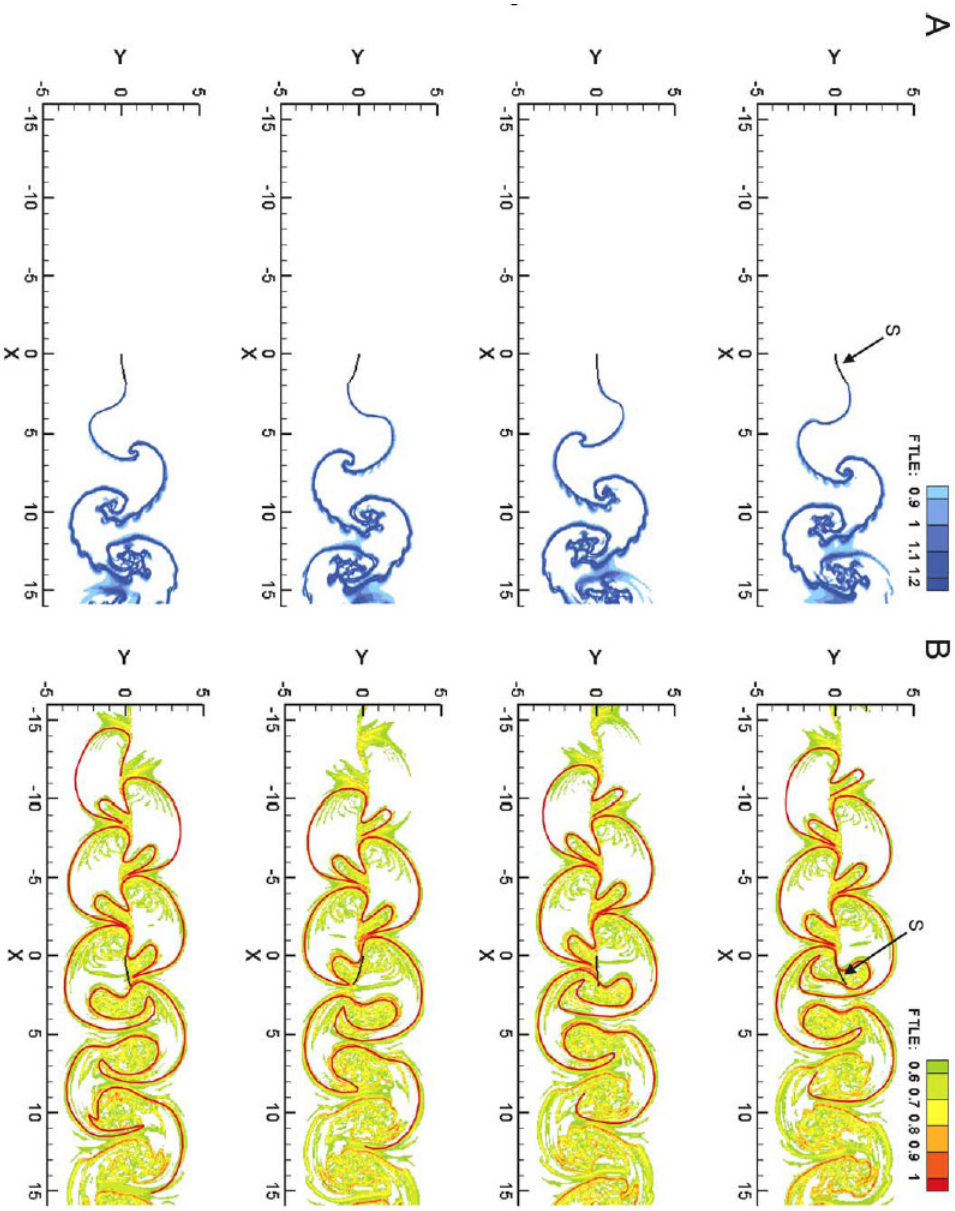

Figure 4.5: FTLE fields of the flow created by the model swimmer. Results are presented in a reference frame fixed on the leading edge of the swimmer; the swimmer moves from right to left in a laboratory reference frame, see Fig. 4.4. S, swimmer. Top panel, time $t = 0$; second panel, $t = T/5$; third panel, $t = (2/5)T$; bottom panel, $t = (4/5)T$, where T is the duration of a single swimming cycle. (A) Backward-time FTLE field. The ridge of large FTLE values identifies the attracting LCS. (B) Forward-time FTLE field. The ridge of large FTLE values (solid red curve) identifies the repelling LCS.

upstream fluid structures can only be visualized by tracking them until the associated repelling LCS has interacted with the swimmer. At this time fluid particle separation becomes most pronounced, and the upstream fluid structures are retrospectively identified.

As previously mentioned, a physical significance of the upstream fluid structures is that it indicates the extent of the region around the swimmer that is affected by its locomotion. In fact, in the present paradigm, locomotion is essentially the process whereby a swimming or flying animal transfers fluid from the upstream fluid structure (defined by the repelling LCS) to the downstream wake (defined by the attracting LCS). To demonstrate these concepts, the behaviour of fluid bounded by adjacent repelling LCS structures in the upstream fluid structures are computationally labeled and tracked. Fig. 4.6 indicates that the fluid in the repelling LCS is indeed the source of fluid that comprises the subsequent downstream vortex wake.

Furthermore, fluid in adjacent repelling LCS structures does not mix and is only moderately deformed, thereby maintaining the coherence of the upstream fluid structures. This is in contrast to the behaviour of arbitrary fluid parcels placed upstream of the swimmer; these experience large deformations of their shape and exhibit substantial mixing (Fig. 4.7). Incidentally, the magnitude of downstream mixing and shape deformation can be predicted by observing the amount of overlap between the interface of the adjacent fluid parcels and the repelling LCS boundaries (Shadden et al., 2007). Despite the fact that the parcels in Fig. 4.7C cover the same amount of upstream area as each of the repelling LCS labeled in Fig. 4.6, they do not indicate the full extent of the downstream wake. This illustrates that both the area and the shape of the upstream fluid structures are important for capturing the subsequent downstream wake and locomotive dynamics.

4.4.3 Mass Flow Rate and a Metric for Swimming Performance

Another goal of the present study is to identify correlations between the geometry of the upstream fluid structures and the propulsive efficiency. One of the most widely used measures of effectiveness

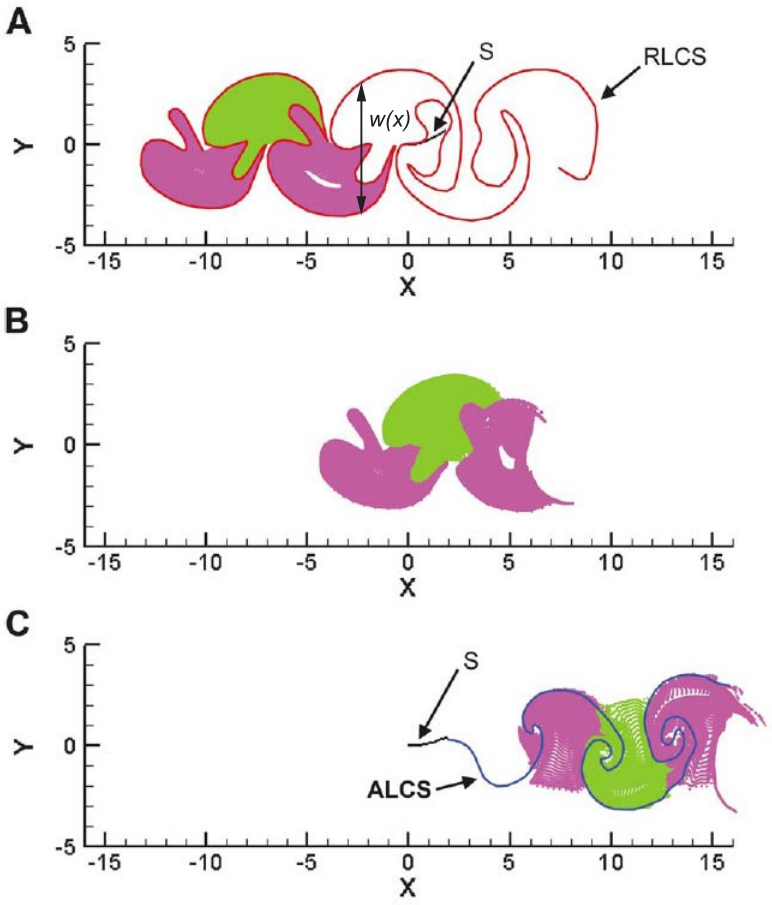

Figure 4.6: Temporal evolution of the upstream wake. Fluid particles in each of three adjacent repelling LCS (red curves) are labeled magenta or green in order to track their evolution. After interaction with the swimmer (shown here in a reference frame fixed on the swimmer; the swimmer moves from right to left in a laboratory reference frame, see Fig. 4.4), the fluid particles in the repelling LCS are shown to comprise the subsequent downstream wake, illustrated by the attracting LCS (blue curves). Fluid particles initially separated by the repelling LCS do not mix and are only moderately deformed. S, swimmer; $w(x)$, the width of the upstream wake; RLCS, repelling LCS; ALCS, attracting LCS. (A) time $t = 0$; (B) $t = (7/5)T$; (C) $t = (14/5)T$, where T is the duration of a single swimming cycle. The width (peak-to-peak in the lateral direction) of the repelling LCS is $w(x)$.

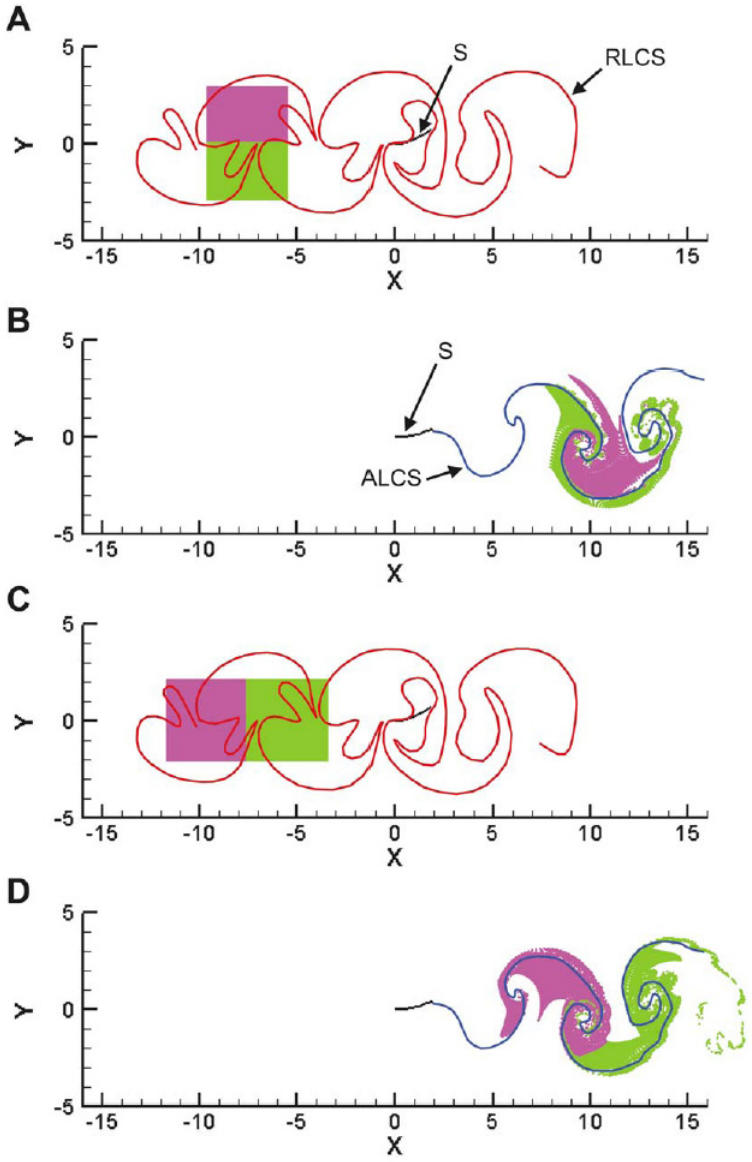

Figure 4.7: Temporal evolution of arbitrary upstream fluid parcels. Fluid particles in adjacent regions with a horizontal (A, B) or vertical (C, D) interface are labeled magenta or green in order to track their evolution. The interfaces in both cases do not coincide with the repelling LCS (red curves). After interaction with the swimmer (shown here in a reference frame fixed on the swimmer; the swimmer moves from right to left in a laboratory reference frame, see Fig. 4.4), the particles in the adjacent parcels exhibit substantial deformation and mixing in the vicinity of the attracting LCS (blue curves). In both cases, the parcels do not indicate the full extent of the downstream wake, in contrast to the repelling LCS parcels in Fig. 4.6. S, swimmer; RLCS, repelling LCS; ALCS, attracting LCS. (A, C) time $t = 0$; (B, D) $t = (14/5)T$, where T is the duration of a single swimming cycle.

of swimming is Froude efficiency, defined as

$$\eta = \frac{\text{useful work}}{\text{total mechanical work}} = \frac{\bar{T}\bar{U}}{\bar{P}}, \tag{4.10}$$

where T is the thrust, U is the swimming speed, P is the total mechanical power, and overhead bars indicate time-averaged values over a stroke cycle. However, for undulatory self-propelled swimmers, it is difficult to separate the drag and the thrusts spatially (Schultz and Webb, 2002), because the entire body contributes to the generation of both forces. This does not mean that the net hydrodynamic force is zero instantaneously. The force is typically oscillatory, resulting in periodic acceleration and deceleration of the swimmer, as shown in Fig. 4.8. This leads to 'temporal separation' of thrust and drag and a corresponding, measurable change in momentum flux in the wake (Tytell, 2007). Therefore, it is possible define an efficiency metric that utilizes the upstream fluid structures to quantify this effect.

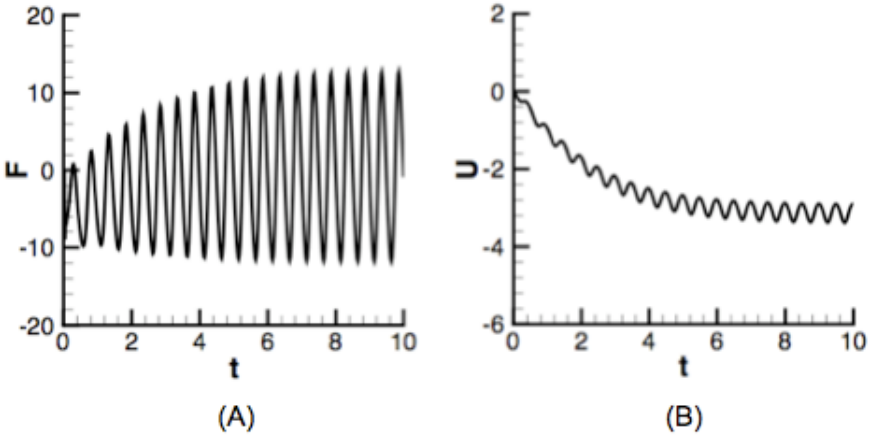

Figure 4.8: (A) Total force acting on the swimmer and (B) the velocity of the swimmer. The swimmer starts from rest. As it approaches a steady state, i.e., the mean velocity over a stroke cycle approaches a constant, the time average of force approaches zero.

To calculate the momentum flux, first a mass flow rate is defined based on the upstream fluid structures described above. Since the upstream fluid structures indicated by the LCS show the exact portion of fluid that is going to interact with the swimmer, it is possible to write a time-averaged

mass flow rate which is relevant to swimming

$$\dot{m} = \rho \bar{U} \bar{w}, \tag{4.11}$$

in which ρ is the fluid density, $\bar{U}$ is the average forward velocity over a stroke cycle, and $\bar{w}$ is the time average of the width (peak-to-peak in the lateral direction) of the repelling LCS $w(x)$ (see Fig. 4.6A). Given the mass flow rate, the net change in the momentum flux due to periodic acceleration and deceleration of the swimmer can be expressed as $\dot{m}\Delta U$, the product of the mass flow rate and the variation (maximum-minus-minimum) of the swimming velocity of the swimmer over a stroke cycle.

Using the momentum flux as a scale for the thrust, a metric for efficiency is introduced as

$$\eta_{LCS} = \frac{(\dot{m}\Delta U)\bar{U}}{\bar{P}}. \tag{4.12}$$

Physically, the term in parenthesis represents the net momentum flux induced by the animal during locomotion. In the limit of purely steady locomotion (i.e. $\Delta U = 0$), there would be no net momentum flux. However, in reality, the forward velocity is only quasi-steady since the reciprocal motion of the appendages causes temporal variations in swimming velocity (Daniel, 1984), as demonstrated in the velocity of the swimmer (Fig. 4.8B).

The efficiency of the self-propelled swimmer using each of the kinematics in Table 1 was calculated after the swimmer reached a steady mean velocity (Fig. 4.8B). The efficiencies were evaluated for different values of ϵ and are plotted in Fig. 4.9 against Strouhal number $St = fA/\bar{U}$ (variable f is the tail beat frequency, A is the peak-to-peak trailing edge excursion, and $\bar{U}$ is the mean swimming velocity). For each swimming kinematics, the efficiency has a peak, located at $St = 0.23, 0.18, 0.27$ for kinematics 1, 2 and 3 respectively. This is consistent with previous studies of oscillating foils and flying/swimming animals that indicate optimal propulsive efficiency at Strouhal numbers within the range of $0.2 \sim 0.4$ (Taylor et al., 2003). Kinematics 1 and 2 have similar efficiencies but lower than that of kinematics 3, indicating that kinematics 3 is the best of the three in terms of swimming

efficiency. The reason that kinematics 3 has the highest efficiency of the three is that it requires less total power than kinematics 1 and swims faster than kinematics 2.

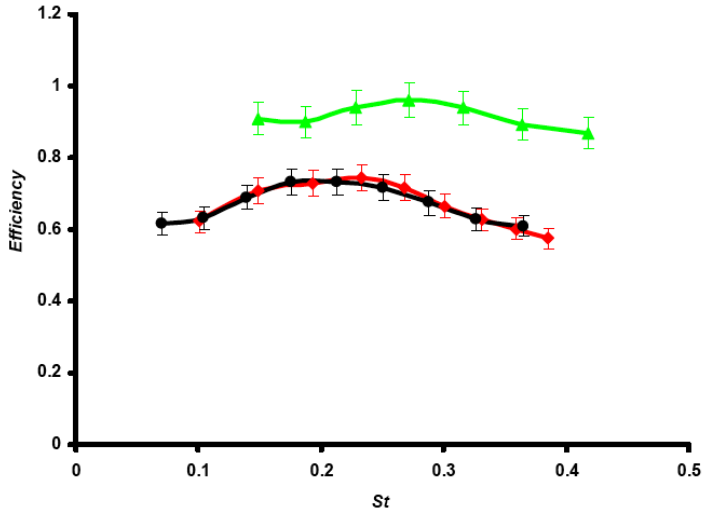

Figure 4.9: Efficiency based on mass flow rate (Eqn. 4.10) of the model swimmer versus Strouhal number $St = fA/\bar{U}$. Red: kinematics 1; black: kinematics 2; green: kinematics 3. Error bars indicate uncertainty in measurement of upstream wake width. The peaks fall into the optimal St range ($0.2 \sim 0.4$) for swimming and flying animals (Taylor et al., 2003).

4.5 Discussion

The LCS analysis provides a method to locate the usually invisible upstream fluid structures. The upstream fluid structures can be used to quantify both the magnitude and the geometry of the interaction between animals and their environment. In this study, the cross-stream dimension of the upstream fluid structures is large relative to the size of the animal. The model swimmer suggests that in order to observe the full extent of the upstream fluid structures in empirical observations of a real animal would require a measurement window many times larger than the animal itself. Notwithstanding, recent measurements of free-swimming jellyfish (Shadden et al., 2006) indicate the existence of upstream fluid structures in that flow as well, albeit with the possibility that the entire structure was not captured in the measurement. By following fluid particles, it is shown that, similar to the model swimmer, only the fluid inside these upstream structures interacts with the

animal. Therefore, despite the simplicity of the computational model used here, the upstream fluid structure is a generic and morphologically diverse feature of locomotion in real fluids.

In the current study, the topology of LCS is consistent with the pattern of the flow generated by a undulatory swimmer. During each stroke cycle, two vortices with vorticity of different signs are shedded from the swimmer, which form a vortex street in the wake. The LCS provides direct geometric information about individual vortices in the vortex street. The evolution of LCS visualizes formation and shedding from the trailing edge, make this Lagrangian analysis a useful tool to understand the dynamics of vortex formation. Similar analysis were used understand vortex formation and shedding in cylinder-cross flow (Franco et al., 2006) and flow around a two-dimensional airfoil (Lipinski et al., 2008).

The upstream fluid structures provide a new focus for fluid dynamic studies of swimming and flying. The upstream structure indicates the portion of fluid that interacts with the animal, thus enabling definition of a mass flow rate induced by locomotion. The new metric for efficiency (η_{LCS}), which is based on change in the momentum flux due to the periodical acceleration of center-of-mass, can be used as a new metric for evaluating swimming performance.

The mass flow rate $\dot{m}$ and the new metric for efficiency η_{LCS} are calculated from the width of the upstream structure w. The width of the upstream structure is larger than the flapping amplitude at the trailing edge, indicating that a larger region of fluid interacts with the swimmer. Fig. 4.10 plots an efficiency metric similar to that in Eqn. 4.11, but with the upstream fluid structure width w replaced by the flapping amplitude A. The efficiency based on flapping amplitude A does not correlate well with the efficiency based on width of the fluid structure w. This is because the width of the fluid structure w depends not only on flapping amplitude A, but also on swimming velocity U. To show this, the width of the fluid structure was calculated for swimming at a constant velocity (2 body length/sec) over a range of tail amplitudes and for swimming over a range of velocities with a fixed flapping amplitude (of 1.44 body lengths). The results are plotted in Fig. 4.11. The width of the upstream fluid structure scales both with increasing flapping amplitude and with increasing swimming velocity. Therefore, the flapping amplitude provides less information about the locomotion

than the upstream fluid structure width, and it cannot take the place of the upstream fluid structure width in the analysis.

Another potentially interesting application of fluid structure shown in this study is to calculate the Strouhal number based on the width of the fluid structure w (as $St = fA/\bar{U}$), similar to its classic definition based on the width of the wake for vortex shedding by bluff bodies (e.g., Triantafyllow et al., 1991), rather than the flapping amplitude used in most animal swimming and flying studies. The efficiencies in Fig. 4.9 are plotted against the modified Strouhal number in Fig. 4.12. Because the width of the fluid structure w is larger than flapping amplitude A, all three curves shift to the right, with the new peaks located at 1.00, 0.92 and 0.91 for kinematics 1 2, and 3 respectively. Interestingly, the new peak efficiency for all three kinematics is more tightly constrained using the modified Strouhal number definition. This result should be investigated further, especially in light of previous studies indicating Strouhal number (defined by flapping amplitude) tuning for a broad range of swimming and flying animals (Taylor et al., 2003).

A major advantage of using the efficiency metric based on the upstream fluid structures and the mass flow rate is that only flow kinematics (i.e., LCS) and body kinematics (i.e., $\bar{U}$ and ΔU) are required for the measurement. To compare the efficiency of animals or propulsion systems for which the mechanical power input is the same, only the numerator of Eqn. 4.11 is needed. Where needed, the mechanical power $\bar{P}$ may be determined by using existing physiological or mechanical measurement techniques (e.g., Biewener, 2003; Krueger, 2006). Importantly, it is not necessary to directly measure the locomotive forces, a longstanding challenge in the study of swimming and flying.

The analysis framework was demonstrated on a model swimmer. The numerical simulation does not include viscous drag; however, the effect of viscous drag contributes only to the total mechanical power $\bar{P}$ in the efficiency calculation. The mass flow rate in real flows can still be determined without loss of generality using the methods described here. In theory, the proposed measure works best when the power loss due to friction P_{fric} is only a small portion of the total mechanical power $\bar{P} = P_{\text{prop}} + P_{\text{wake}} + P_{\text{fric}}$, where P_{prop} and P_{wake} are useful power for propulsion and wake power.

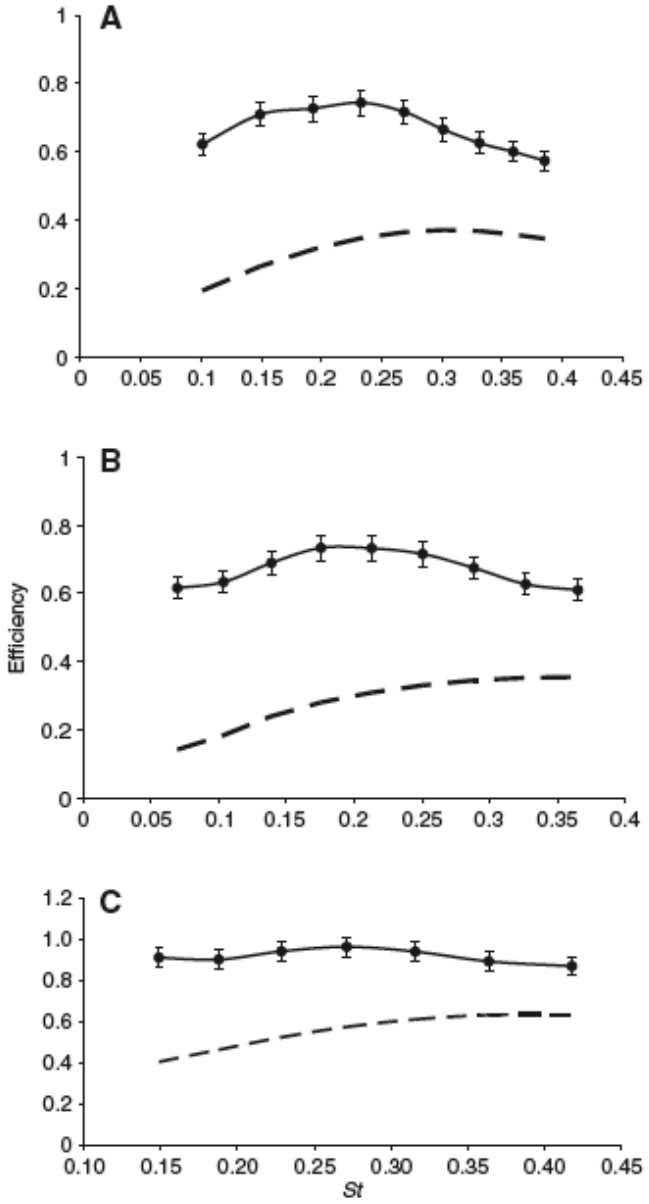

Figure 4.10: Comparison of measures for swimming efficiency. Plots for kinematics 1, 2, and 3 are from top to bottom. Solid line: efficiency based on the width of the upstream fluid structure; Error bars indicate uncertainty in measurement of upstream wake width; dash line: efficiency calculated by replacing upstream wake width with stroke amplitude of the swimmer (peak-to-peak excursion at trailing edge).

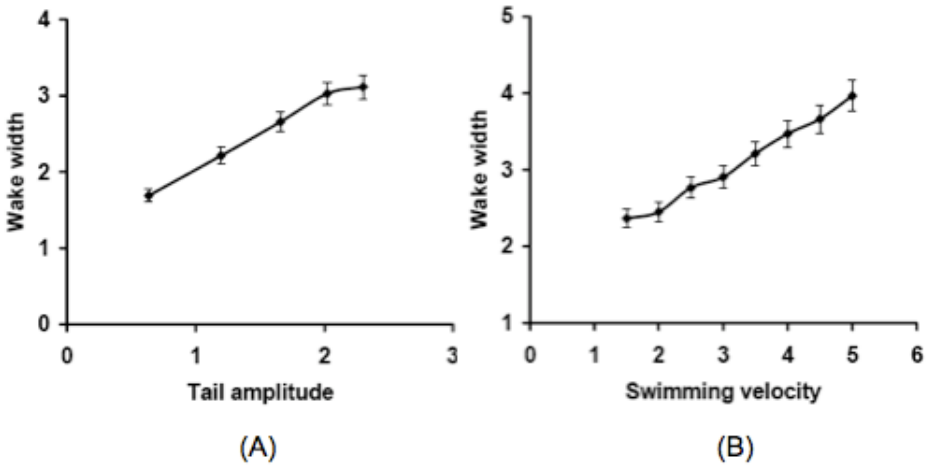

Figure 4.11: The width of the wake. (A) Wake width of a swimmer swimming a constant velocity (2 body length/sec) with different tail amplitudes. (B) Wake width of a swimmer swimming at different velocity with the same body kinematics (flapping amplitudes of 1.44 body length).

This requires

$$P_{\text{fric}} \ll P_{\text{prop}} + P_{\text{wake}}. \tag{4.13}$$

Because the friction force F_{fric} scales with $F_{\text{fric}} \sim \mu AU/L = \rho AU^2/Re$, $P_{\text{fric}} = F_{\text{fric}}U \sim \rho AU^3/Re$. Therefore, the requirement becomes

$$Re \gg \rho AU^3/(P_{\text{prop}} + P_{\text{wake}}), \tag{4.14}$$

where Re is the Reynolds number, ρ is the fluid density, A the wetted surface area of the swimmer and U the swimming velocity.

In the current vortex sheet model, the entire body acts as a swimming appendage actively generating locomotive forces. Kinematics are prescribed for the entire body of the swimmer and the hydrodynamical forces acting on body are coupled only with the motion of the swimmer. This represents swimming animals whose entire body is actively controlled by muscles. However, swimming and flying appendages often have flexibility and are able to deform when interacting with surrounding fluids. Studies have shown that, compared with rigid structures, flexibility can enhance hydrodynamic and aerodynamic performance, which include increased thrust, reduced drag, as well

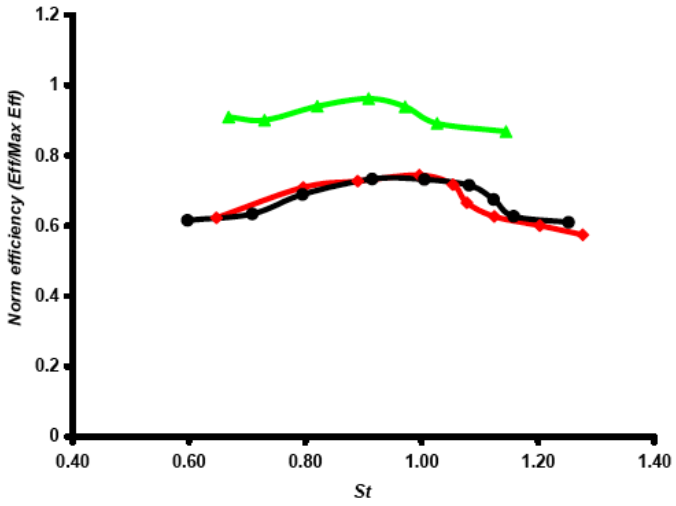

Figure 4.12: Efficiency the swimmer versus modified Strouhal number $St = fw/\bar{U}$. Red: kinematics 1; black: kinematics 2; green: kinematics 3.

as better efficiency (e.g., Alben et al., 2002; Zhu, 2007; Vanella et al., 2009). Recent studies further developed the vortex sheet method to incorporate passive deformation of the body due to the forces from the surrounding fluid and the flexibility of the body itself (Alben, 2008). The effect of body flexibility on the LCS analysis and efficiency measurements developed in this study will be explored in further studies.

Studies are ongoing to apply the method developed here to measure propulsive efficiency of eel swimming from DPIV measurements. When applying to PIV measurements from animal swimming, the field of view in measurements should be large enough to cover some distance upstream the animal. For animals with periodic stroke pattern, the LCS is also periodic with the same frequency. So the distance upstream the animal in the field of view should be equal to or larger than the distance the animal can swim during a stroke cycle, i.e., swimming velocity multiplied by stroke period. Because a relatively large field of view is required, the resolution of the velocity field is limited. Errors may be introduced when interpolating velocity on a finer mesh. However, the proposed method is robust to noise in flow measurements. It has been proved that even large velocity errors lead to reliable predictions on LCS, as long as the errors remain small in a special time-weighted norm (Haller, 2002).

Although the analytical framework was demonstrated in a 2-D flow, the LCS analysis can be extended to 3-D flows, in which the LCS are surfaces rather than a curves (Lekien et al., 2007). Though volumetric flow measurements are difficult for animal swimming, the three-dimensionality of the flow can be evaluated by a single measurement on the mid-plane together with assumptions such as flow patterns are constant in the vertical dimension, up to the dorso-ventral height of the animal; or by measurements on multiple parallel planes. One advantage is that given the fact that Eulerian particle image velocimetry is more difficult than Lagrangian particle tracking velocimetry in 3-D flows, the present analysis would be especially well-suited to 3-D experiments since LCS can be directly calculated from particle trajectories.

In summary, the upstream fluid structures visualized by the LCS analysis provide new information regarding the interaction between swimming/flying animals and the fluid environment. These animal-fluid interactions have broad consequences for predation and other behavioural functions. As previous measurements of animal swimming and flying are re-examined and new observations are made using the methods described here, the upstream fluid structures can become as useful as the downstream wake has traditionally been for comparative biological and engineering studies of animal locomotion.

4.6 Acknowledgements

The author thanks Dr. Robert Krasny, Dr. Jeff Eldredge and Dr. Ratnesh Shukla for discussions on the vortex sheet method. The author also thanks Dr. George Lauder for discussions on eel swimming.

Chapter 5

Particle Lagrangian Coherent Structures and a Medusan Feeding Model

5.1 Summary

When applied to fluid flows, the LCS analysis uses trajectories of ideal (passive, infinitesimal) fluid tracers to identify barriers in fluid transport. In some biological transport systems, what is more relevant to biological activities than fluid transport is the transport of biomass. For example, in planktonic ecosystems, some medusan species, such as moon jellyfish (*Aurelia sp.*), can use their body motion to generate feeding currents that transport zooplankton prey to the vicinity of their capture appendages. Because the dynamics of prey particles are different from ideal fluid tracers, the original LCS analysis does not describe their transport. In this study, the concept of particle Lagrangian Coherent Structures (pLCS) is developed to study transport of particles in fluid flows. The pLCS act as barriers of particle transport in fluid flow, therefore providing direct geometric information about the motion of ensembles of particles. In the application to jellyfish feeding, with the flow field generated by jellyfish measured experimentally and the dynamics of plankton described by a modified Maxey-Riley equation, the pLCS identify an encounter region in which prey can be encountered by jellyfish. This medusan feeding model is able to demonstrate prey selection based on prey size and escape behaviours. The encounter region determined by the model can also explain the observed pattern of encounter region in empirical prey tracking experiments. Hence, the

model provides a mechanical basis for evaluating the predatory role of jellyfish in marine planktonic systems. The pLCS framework developed here can also be used to study transport in multiphase and granular flows in general.

5.2 Introduction

Due to their wide geographic distribution and large populations, jellyfish medusae have a significant influence on marine plankton ecosystems. They feed on zooplankton, fish eggs and larvae, therefore directly influencing plankton ecosystems and natural fishery resources (Purcell and Grover, 1990; Matsakis and Conover, 1991). The importance of medusae in marine plankton ecosystems has motivated interests in understanding their predatory activities and evaluating their trophic effects on marine ecosystems. More frequent and substantial medusan population outbreaks in recent years (Kawahara et al., 2006; Purcell et al., 2007) further highlight the importance of studying this subject.

Medusan species exhibit a variety of predation modes. Of particular interest for fluid mechanics is a group of large medusan species, including hydromedusae and scyphomedusae, which use their body motions to generate feeding currents in their surrounding fluid for predation (Costello and Colin 1994; Ford et al., 1997). For these species, swimming and prey encounter are concurrent activities. The periodic contractions of body not only generate thrust for swimming, but also induce feeding currents to transport prey towards the tentacles and oral arms, where the prey can be captured (Colin et al., 2003). It has been shown that physiological constraints and hydrodynamic requirements for locomotion and feeding determine that these medusae typically have oblate bells and use a rowing swimming mode (Costello et al., 2008). Both the oblate bell shape and the rowing propulsive mode are favorable for these medusae because they appear to increase the feeding current and decrease the energy expended during swimming (Colin et al., 2003).

Estimation of trophic effects of these medusae requires a better understanding of the feeding mechanism. Many previous studies have focused on quantification of predation rate and identification of dominant factors in the predatory process. These studies typically use empirical methods such as functional response curve analysis (Hansson et al., 2005) and gut content analysis (Matsakis and

Conover, 1991). Laboratory and field studies of this kind have provided an abundance of empirical data and demonstrated dietary preferences for prey organisms across different medusan species. They have also identified several important physiological and behavioral factors in prey encounter and selection, such as prey size, escape capability, and digestibility. However, because it is difficult to separate the effects of these parameters in experimental studies, the relative importance of these parameters for different medusan species is still unclear.

Given the nature of the current-generating feeding mechanism, it is expected that transport properties of feeding currents are also important factors in this feeding mechanism. Therefore, it is necessary to understand the fluid mechanical basis of prey encounter and to develop a physical model describing the animal-fluid interactions that underlie the encounter and selection processes. Such a model can potentially test different hypotheses regarding prey encounter and selection. It can also enable independent control of governing parameters in a manner that is more difficult to achieve in field and laboratory studies. A physical model can also generalize experimental results on specific medusan species to predict predation by other species.

Recent studies on large cruising scyphomedusae have made progress in this regard. Using the LCS technique, Shadden et al. (2006) developed a mechanistic model that quantified fluid motions during swimming of scyphomedusae (*Aurelia sp.*) and identified a region in which the fluid can interact with the capture surface. However, the LCS was originally developed to study homogenous fluid transport based on fluid tracer trajectories, rather than the transport of prey particles in the flow, which generally have different dynamics than fluid tracers. Therefore, interactions between the predator medusae and their prey were not considered in the analysis and the effects of prey parameters such as prey size, swimming force, and escape behaviors were not studied. In the present study, the original LCS analysis on homogenous fluid transport is extended to the study of prey particles in fluid flow. A new concept called particle Lagrangian Coherent Structures (pLCS) is developed as transport barriers in the dynamical systems of prey particles. The pLCS is used to quantify the encounter region for different prey types and to demonstrate prey selection based on size, swimming force, and escape behaviors.

The chapter is organized as follow: Section 5.3 presents experimental and theoretical methods used in the study. It starts with descriptions of prey tracing experiments and DPIV velocity measurements. Then it introduces an equation of motion for prey particles in the flow. This is followed by a presentation of the pLCS analysis on prey transport. Section 5.4 reports an encounter map measured from prey tracking experiments. It also presents results from the pLCS analysis, in which effects of prey size, swimming force, and escape behaviors on the encounter region are investigated. The chapter concludes with a discussion in section 5.5 on the benefits and limitations of the developed methods and suggestions for potential applications.

5.3 Methods

5.3.1 Prey Tracking

Juvenile jellyfish (*Aurelia sp.*) (diameter between $6 \sim 12$ cm) were collected from a local aquarium, transported to the laboratory and kept in an acrylic tank ($90\times76\times38$ cm height×length×width) filled with seawater of salinity 33 per mill at 58 °F. Experiments were done within 48 hour of transport. Brine shrimp (*Artemia sp.*) were hatched in an acrylic cone at 80 °F overnight before the experiment.

In prey-tracking experiments, individual jellyfish were transferred to a smaller acrylic tank ($25.5\times30.5\times18.5$ cm). Newly hatched brine shrimp were introduced into the tank as prey for jellyfish. The amount of brine shrimp introduced into the tank was such that the total particle number on the recorded image is around 200. White light from a dive lamp illuminated a water column of roughly $25\times15\times5$ cm at the center of the tank. Videos were recorded on a Pulnix ccd camera with 720×480 resolution at frame rate of 30 Hz. Good video sequences with jellyfish actively feeding (with apparent prey transport) were chosen for analysis.

An in-house code was developed to process the recored videos. The code tracks individual brine shrimp over time and determines trajectories. This code consists of the following parts:

(i) Particle detection on images

Individual brine shrimp (*Artemia sp.*) are visualized as bright particles on recored videos. Before looking for particles, images were thresholded and converted into grayscale light intensity mode in order to reduce the effects of diffused edges. Each particle consists of a certain number of connected pixels with various intensity levels. The center of the particle was determined by Gaussian fitting, which is a commonly used approach to detect particle centroid at sub-pixel level. The intensity of particles (pixel groups) was fitted into the following function (Mann et al., 1999):

$$I(x,y) = \frac{I_0}{2\pi\sigma_x\sigma_y}\exp\left\{-\frac{1}{2}\left[\left(\frac{x-x_c}{\sigma_x}\right)^2 + \left(\frac{y-y_c}{\sigma_y}\right)^2\right]\right\}. \tag{5.1}$$

Five parameters, I_0, σ_x, σ_y, x_c, and y_c, were determined using the Gaussian fitting and (x_c, y_c) was the centroid of the particle.

(ii) Trajectory tracking

After particle centroids were determined on all frames of a video sequence, they were connected on consecutive frames to generate trajectories. A particle tracking algorithm downloaded from http://physics.georgetown.edu/matlab/ was modified and used here. For each particle on frame (i), all particles on frame ($i+1$) within a prescribed radius of maximum displacement r of the original particles position were identified as possible new positions. Given the positions for m particles at frame (i), and n possible new positions at frame ($i+1$), the algorithm considers all possible identifications of the m old positions with the n new positions, and chooses the identification which results in the minimal total squared displacement as the projection from frame (i) to frame ($i+1$). Centroid of the same particles on consecutive frames were connected as trajectories.

After prey trajectories were determined, they were separated into two groups, i.e., encountered and escaped. The criterion for prey encounter is that the prey particle contacts the capture surface. The locations of encountered and escaped prey were used to create the encounter map, which

indicates the regions in which prey can be encountered by the predator.

5.3.2 Flow Velocity Measurements

Due to the limitation in the number of prey trajectories able to be measured, prey tracking experiments could only provide a qualitative measurement of the encounter map. For the feeding model, it was desired that prey transport be determined based on the flow field and properties of prey. DPIV was used to measure velocity fields around jellyfish, which were used as input in the model to predict prey trajectories.

To obtain fluid velocity measurements around *Aurelia sp.*, individual jellyfish were video-taped swimming freely in an acrylic tank (90×76×38 cm). A pulsed argon laser of 30 Hz was focused into a thin light sheet 1–2 mm thick and 20 cm wide at the center of the tank which illuminated reflective silver-coated neutrally-buoyant hollow glass spheres (mean diameter 13 μm) suspended in the water. The density of particles were controlled such that there were around 7 illuminated particles per 32×32 pixel on recorded images. Videos were taken using a Uniq ccd camera with 1024×1024 resolution at frame rate of 30 Hz synchronized with the laser. Video sequences in which a jellyfish swam through the laser plane for several consecutive swimming cycles were collected for analysis. These sequences were analyzed using an in house DPIV analysis system to quantify velocity field measurements of the flow. For details of the experiments, please refer to previous studies on swimming properties of the same species (Shadden et al., 2006; Franco et al., 2007).

5.3.3 Dynamics of Prey

Most jellyfish feed on fish larvae and zooplankton such as copepods. These prey have a characteristic length on the order of $a = 1$ mm (Strickler, 1975). For simplicity, their body shape were neglected and were considered as rigid spherical particles in the model. In a classic paper, Maxey and Riley (1983) described the equation of motion for small rigid spherical particles in an incompressible fluid

as

$$\begin{aligned}\rho_p \frac{d\mathbf{v}}{dt} &= \rho_f \frac{D\mathbf{u}}{Dt} + (\rho_p - \rho_f)\mathbf{g} \\ &- \frac{9\nu\rho_f}{2a^2}(\mathbf{v} - \mathbf{u} - \frac{a^2}{6}\Delta\mathbf{u}) \\ &- \frac{\rho_f}{2}[\frac{d\mathbf{v}}{dt} - \frac{D}{Dt}(\mathbf{u} + \frac{a^2}{10}\Delta\mathbf{u})] \\ &- \frac{9\rho_f}{2a}\sqrt{\frac{\nu}{\pi}}\int_0^t \frac{1}{\sqrt{t-s}}\frac{d}{ds}(\mathbf{v} - \mathbf{u} - \frac{a^2}{6}\Delta\mathbf{u})ds,\end{aligned} \tag{5.2}$$

where variable $\mathbf{v}$ represents the velocity of the particle; $\mathbf{u}$, the local velocity of the flow in the absence of the particle; ρ_p, the density of the particle; ρ_f, the density of the fluid; ν, the kinematic viscosity of the fluid; a, the radius of the particle; and $\mathbf{g}$, gravity. The terms on the right represent, respectively, the force exerted by the undisturbed flow on the particle, buoyancy, Stokes drag, the added mass, and the Basset-Boussinesq memory force (Babiano et al., 2000). The derivative $D\mathbf{u}/Dt$ is along the path of an ideal fluid tracer

$$\frac{D\mathbf{u}}{Dt} = \frac{\partial\mathbf{u}}{\partial t} + (\mathbf{u}\cdot\nabla)\mathbf{u}, \tag{5.3}$$

whereas the derivative $d\mathbf{v}/dt$ is taken along the trajectory of the particle. The history and development of the equation can be found in the review by Michaelides (1997).

The Maxey-Riley equation can be significantly simplified if particles are sufficiently small so that the Basset-Boussinesq memory force and the terms with $a^2\Delta\mathbf{u}$ can be neglected (Babiano et al., 2000). Nondimensionalizing the equation by a characteristic length scale of the flow L, characteristic velocity of the flow U, and characteristic time scale $T = L/U$, the simplified equation of motion is expressed as

$$\frac{d\mathbf{v}}{dt} - \frac{3R}{2}\frac{D\mathbf{u}}{Dt} = -A(\mathbf{v} - \mathbf{u}) + (1 - \frac{3R}{2})\mathbf{g}, \tag{5.4}$$

with

$$R = \frac{2\rho_f}{\rho_f + 2\rho_p}, A = \frac{R}{St}, St = \frac{2}{9}(\frac{a}{L})^2 Re. \tag{5.5}$$

The particle dynamics depend on three dimensionless parameters: the variable R is the mass ratio parameter, St is the particle Stokes number, $Re = UL/\nu$ is the Reynolds number of the flow, and A is the size parameter describing the inertia effect of particles, with the limit $A \to \infty$ corresponding to infinitesimal fluid tracers (a= 0).

Strictly speaking, the Maxey-Riley equation is valid when the following 3 conditions hold (Maxey and Riley, 1983):

(1) particle size is small compared with characteristic length of the flow: $a/L \ll 1$;

(2) the disturbance flow produced by the motion of the particle is at sufficiently low Reynolds number: $Re_a \sim aW/\nu \ll 1$, where W is the representative velocity scale of the velocity difference between the particle and local flow velocity ($\mathbf{v} - \mathbf{u}$); and

(3) particle Stokes number is small: $St \sim (a^2/\nu)(U/L) \ll 1$.

When these conditions are satisfied, the effect on the flow field due to particle motion is restricted to a small area around the particle. In this situation, the flow field is considered independent of particle motion. Therefore, it is possible to first measure the flow and then simulate particle motion using the Maxey-Riley equation.

The Maxey-Riley equation was modified to incorporate self-propulsion of prey zooplankton. The forces on the right-hand-side of the Maxey-Riley equation only include fluid forces acting on passive particles due to the background fluid currents and gravity. However, zooplankton are capable of self-propulsion, often triggered by perception of a nearby predator. This effect was incorporated in this study by the addition of a term $\mathbf{a}_e = \mathbf{F}_e/m$ to Eqn. 5.4, representing the acceleration rate of prey animals due to the self-generated escape force $\mathbf{F}_e$, with m being the mass of individual prey. This escape force may be dependent on prey swimming ability and behavioral responses to predators. Assuming prey are neutrally buoyant, the mass ratio parameter in Eqn. 5.5 was set to $R = 2/3$. Therefore the dynamics of a prey animal can be expressed as

$$\frac{d\mathbf{v}}{dt} - \frac{D\mathbf{u}}{Dt} = -A(\mathbf{v} - \mathbf{u}) + \mathbf{a}_e, \tag{5.6}$$

with $\mathbf{a}_e$ non-dimensionalized by U^2/L. Without the escape acceleration term $\mathbf{a}_e$, Eqn. 5.6 is the simplified Maxey-Riley equation for neutrally buoyant spherical particles. In order to satisfy the abovementioned three assumptions for the Maxey-Riley equation, the external acceleration term has to be on the same or smaller order of magnitude of the Stokes drag term, i.e, $(F_e/m)/(U^2/L) \leq AW/U$, which is equivalent to $F_e/6\pi\mu W \leq O(1)$. So the external (swimming) force term $\mathbf{F}_e$ should be on the same or smaller order of magnitude of the Stokes drag.

The equation was non-dimensionalized by length scale $L = 5$ cm (the radius of the jellyfish) and characteristic velocity $U = 1$ cm/sec (the jellyfish swimming speed). The corresponding Reynolds number of the flow $Re = 500$, and for a prey with size $a = 1$ mm, the particle Stokes number $St = 0.04$ and the particle size parameter $A = 15$.

5.3.4 Transport of Prey by pLCS

The velocity $\mathbf{v}$ of individual prey particles along its trajectories was solved from Eqn. 5.6. Imaginary prey particles could be placed in any area of interest in the flow and their trajectories be calculated. This enabled us to study the transport of prey in detail without being limited by the number of trajectories observed in prey tracking experiments. A fourth-order Runge-Kutta method was used to integrate particle velocity $\mathbf{v}$ and calculate prey trajectories. Calculating prey particle velocity $\mathbf{v}$ requires flow velocity $\mathbf{u}$ as input. Because the DPIV technique only provided time-resolved velocity measurements on a discrete mesh, flow velocity $\mathbf{u}$ at any given point within the field of view was calculated by a cubic interpolation.

Calculation of FTLE from prey particles trajectories is similar to the calculation from ideal fluid tracers. Prey particles were placed on a structured mesh over the entire flow field and their trajectories calculated for a duration of 4 jellyfish stroke cycles. FTLE fields were calculated as described in Chapter 2. pLCS, defined as high-value ridges of FTLE, were extracted visually from FTLE contour plots. The uncertainty of pLCS identification is about 3%.

5.4 Results

5.4.1 Prey Tracking

Trajectories of some prey *Artemia sp.* measured in the prey tracking experiment are plotted in Fig. 5.1. The initial positions of these prey relative to that of the jellyfish are also designated. As shown in the figure, these prey can be separated into two groups, i.e., encountered (red) and escaped (green), based on their trajectories. The criterion for prey encounter is that the prey contacts a capture surface. For *Aurelia sp.*, encounters only occur in the subumbrellar region, primarily on the oral arms or tentacles. From the initial positions of these prey, it is observed that encounter regions in the upstream of the jellyfish are discrete and separated by regions in which prey do not encounter the jellyfish. This characteristic, i.e., the heterogeneity of the encounter map, indicates that the transport process is not continuous. However, due to the limitation in the number of prey trajectories able to be measured in this type of experiments, only a qualitative measurement of the encounter map could be obtained.

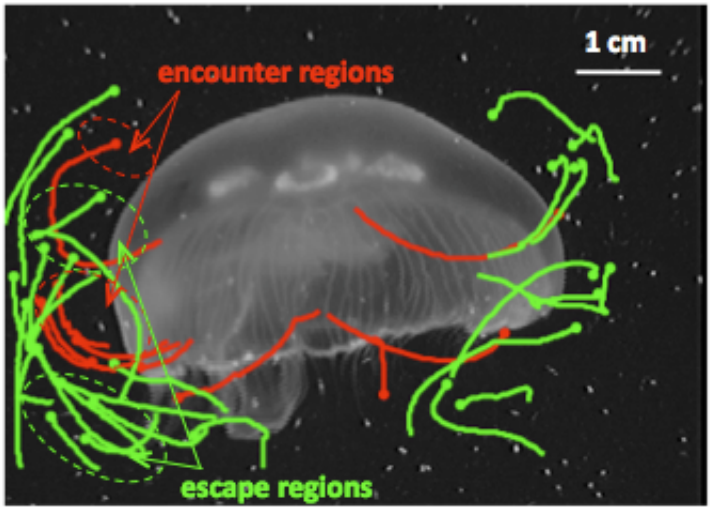

Figure 5.1: Trajectories of brine shrimp (*Artemia sp.*) in feeding currents generated by a jellyfish (*Aurelia sp.*). Red curves: trajectories of brine shrimp being encountered by the jellyfish; green curves: trajectories of brine shrimp not encountered. Dots: initial positions of brine shrimp. Jellyfish image is on the initial frame. The encounter map is heterogeneous, consisting of discrete encounter regions (circled by red dash lines) separated by escape regions (circled by green dash lines).

5.4.2 Prey Trajectories Predicted by the Model

Results below are based on the proposed model. Imaginary prey particles with size $a = 1$ mm (similar to that of copepods, i.e., $a = 1$ mm) and no escape force ($\mathbf{a}_e = 0$) are placed in a region of interest in the flow. Originally they have the same velocity as local flow velocity. Their trajectories were calculated from the measured velocity field and Eqn. 5.6. Fig. 5.2 shows their initial positions and later trajectories. Using the same criterion as in the prey tracking experiment, these prey are separated into groups of encountered (i.e., prey that enter subumbrellar region, follow jellyfish swimming direction, and contact a capture surface) and escaped prey. Similar to the encounter map from prey tracking experiments (Fig. 5.1), the encountered and escaped prey are originally located in discrete regions around the jellyfish. Though these two groups of prey are initially proximate to each other, it can be seen from their trajectories that they have different kinematics. Encountered prey follow the jellyfish and move in the same direction (towards upstream). In contrast, escaped prey advect towards downstream. The spatial separation between the two groups became more significant as time progressed.

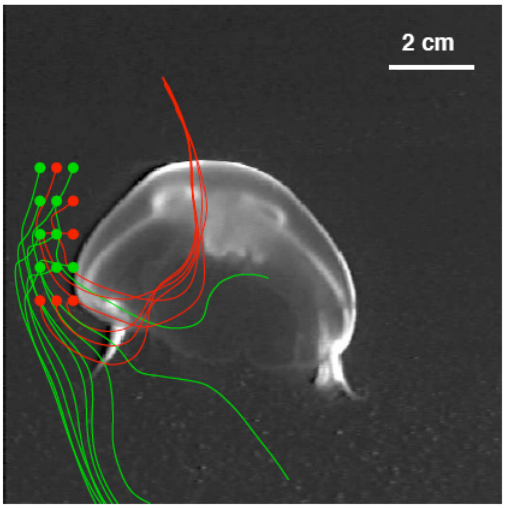

Figure 5.2: Predicted trajectories of prey (size $a = 1$ mm and no escape force) in feeding currents generated by jellyfish. Red curves: trajectories of particles encountered by the jellyfish; green curves: trajectories of particles not encountered. Dots: initial position of prey particles. Jellyfish image is on the initial frame. The separation between originally proximate encountered and escaped prey particles is significant.

5.4.3 The pLCS and Prey Encounter Region

The FTLE field (Fig. 5.3) is calculated from prey trajectories initiated from a structured mesh over the entire flow field. It represents the rate of separation between prey particles. The ridge of the FTLE contour plot is clearly identifiable as the pLCS, plotted as the solid white line in Fig. 5.4 around the jellyfish. The pLCS is a continuous curve that encloses a subumbrellar region in contact with the sensory apparatus of the animal and finger-like structure above the bell called 'lobes' (Shadden et al., 2006). The pLCS is not closed at the top as new lobes are continuously being generated. Even with the opening at the top, it is not conceptually difficult to separate the regions inside and outside the pLCS. The region inside the pLCS is the encounter region, and prey can be captured by the animal. Notice that the pLCS is not symmetric on Fig. 5.4. The most significant difference is that lobes are not well-resolved on the right-hand side of the jellyfish body axis. This is an artifact of the DPIV measurements, in which the velocity on the right-hand side of the animal body was not well-resolved due to the fact the animal body partially blocked some laser illumination in experiments (the laser sheet was introduced from the left). Therefore, there is not much pLCS on the right-hand-side of the animal.

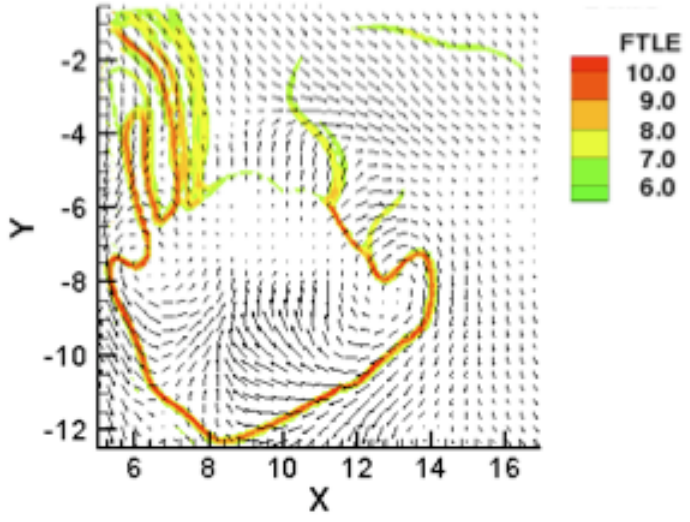

Figure 5.3: The FTLE field (contour plot) and velocity field (vector plot) at a given time instant.

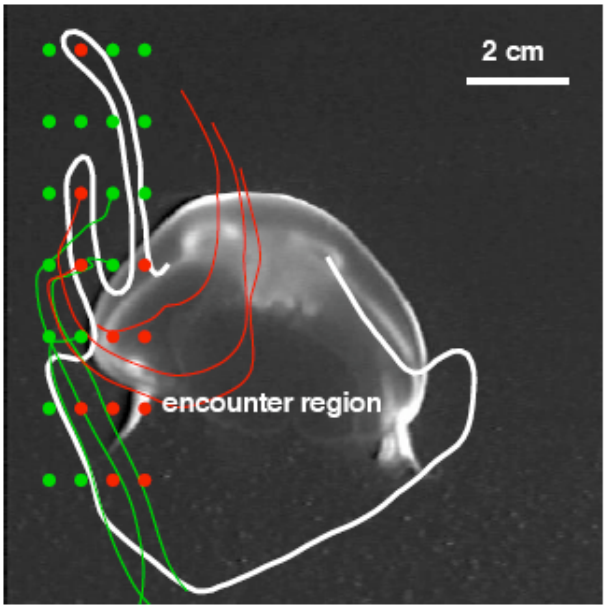

Figure 5.4: The pLCS (thick white curve) around a jellyfish indicating the encounter region. Some prey originated at that frame (dots) and their trajectories (thin solid curves) are also plotted. The prey inside the pLCS (red) are encountered by the jellyfish, whereas prey outside the pLCS (green) are not encountered. The pLCS is calculated at a given time frame and only shows the encounter region at that frame. The pLCS is similar to the fluid LCS of a jellyfish wake in Shadden et al. (2006).

The initial positions of some prey particles and their trajectories are also plotted in Fig. 5.4. The pLCS is similar to the fluid LCS of a jellyfish wake in Shadden et al. (2006) (comparisons are discussed in the following section). The encounter region defined by the pLCS is the region in which prey will encounter the jellyfish capture surface. In other words, prey inside the pLCS are encountered by the jellyfish whereas prey outside the pLCS are not, as shown by the trajectories. Therefore, the pLCS act as a global structure of prey transport. As long as the pLCS is known, it is not necessary to know the trajectories of individual prey to determine whether they are encountered or not. The pLCS in the encounter region includes several slender finger-shaped lobes above the bell of the jellyfish and a subumbrellar cavity. The lobes are not connected in the circumferential direction along the bell, but separated by regions in which prey are not encountered. This pattern is consistent with what is observed in prey tracking experiments (Fig. 5.1). The spatial heterogeneity of pLCS in the lobe region leads to observed patchiness of the encounter map.

5.4.4 Effects of Prey Properties on Encounter Region

The pLCS result shown in the previous section resembles the fluid LCS identified in the flow generated by the same jellyfish species in the study of Shadden et al. (2006). While the fluid LCS is only dependent on the flow field, the pLCS also depends on the properties of particles. In this current study, because the size of the encounter region identified by the pLCS provides a quantitative measurement of jellyfish predation, it is possible to study the effect of prey parameters such as size, swimming force, and escape behaviors. In the following, trajectories of different types of prey are simulated using Eqn. 5.6 and pLCS for these prey types are calculated. Then the comparisons between the encounter region sizes for different prey types are made to study the effect of prey parameters.

First, the effect of prey size/inertia and swimming forces on the encounter region is studied. The pLCS for ideal infinitesimal prey (i.e., fluid LCS) is used as the baseline (white curve in Fig. 5.5). The pLCS for prey with size $a = 1$ mm and no escape force is also plotted in Fig. 5.5 (red curve). It is clear that the encounter region for finite-sized prey is smaller than that for ideal infinitesimal prey. The result indicates that it is more difficult for jellyfish to capture larger prey.

Prey can also generate swimming force to escape predation. Some zooplankton, like copepods, can generate momentary acceleration up to 12 m/s^2 when escaping predation by power-stroke of their legs (Strickler, 1975). To successfully escape predation, the prey escape reaction should be directional. However, there is no existing literature demonstrating the directional preference of zooplankton's escape reaction to a predator. To simplify the problem, it is assumed that the escape force has one of two different forms: $\mathbf{a}_e = -a_e\mathbf{u}/u$ or $\mathbf{a}_e = -a_e\mathbf{n} \times \mathbf{u}/u$ ($\mathbf{n}$ being a unit vector normal to the plane). The former represents an escape force with its direction always opposite to local flow velocity, and the latter represents an escape force with its direction always normal to local flow velocity and away from the predator. It is also assumed that the escape force is persistent, and thus the acceleration has a smaller value, with the magnitude $a_e = 0.05$ m/s^2 ($a_e = 25$ if non-dimensionalized by U^2/L) in both models. The pLCS are shown in Fig. 5.5: the yellow curve is the pLCS for prey with escape force opposite to local flow velocity, and the green curve is the pLCS

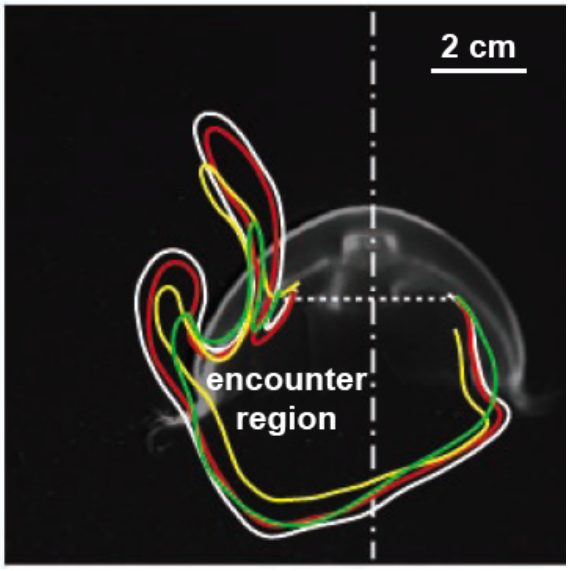

Figure 5.5: pLCS for different prey, superimposed over the jellyfish (a different individual from the one in Fig. 5.4). Solid white: pLCS for ideal infinitesimal prey; red: pLCS for prey with size $a = 1$mm and no escape force; yellow: pLCS for prey ($a = 1$mm) with an escape acceleration ($\mathbf{a}_e = 0.05$ m/s^2) opposite to local flow velocity; green: pLCS for prey ($a = 1$mm) with an escape acceleration ($\mathbf{a}_e = 0.05$ m/s^2) normal to local flow velocity. The encounter region is inside pLCS. The inertia and escape swimming force make the encounter region smaller. The axis of the jellyfish body is shown as the dash-dot line.

for prey with escape force normal to local flow velocity.

Comparing the results plotted in Fig. 5.5, it is clear that the encounter region for finite-sized prey is smaller than that for ideal infinitesimal prey. Adding an escape force to the prey can further reduce the area of the encounter region. This result is consistent in four other individual jellyfish of the same species studied. Comparisons between encounter regions for ideal infinitesimal prey and for prey ($a = 1$mm) with an escape acceleration ($\mathbf{a}_e = 0.05$ m/s^2) opposite to local flow velocity are plotted for these animals in Fig. 5.6.

In Table 5.1, the area and the volume of the encounter region are compared to quantify the effects of prey inertial and escape force. The area of the encounter region is the area inside the pLCS on the left-hand side of the jellyfish body axis (closed by the imaginary dashed line on the top) and the volume of the encounter region is calculated based on the the left-hand side pLCS assuming that pLCS is axisymmetric. For each individual animal, the size of the encounter region area and volume are non-dimensionalized by that for the ideal infinitesimal prey. The average and

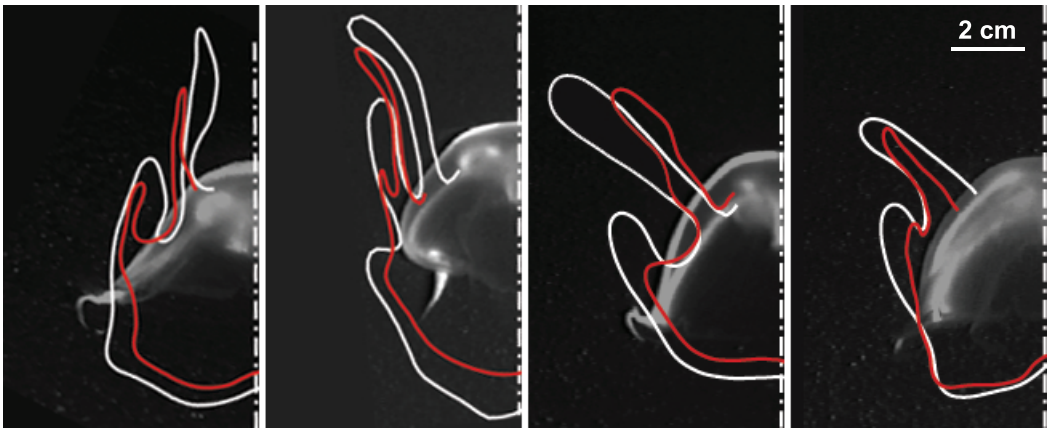

Figure 5.6: Encounter regions for additional four jellyfish individuals of the same species. White: pLCS for ideal infinitesimal prey; red: pLCS for prey ($a = 1$mm) with escape acceleration ($\mathbf{a}_e = 0.05$ m/s^2) opposite to local flow velocity. Animals assume arbitrary swimming directions, but images are rotated so that the body axes are vertical. Only half plane on one side of the body axis (the dash-dot line) is shown. All images are of the same scale.

the standard deviation of the five animals studied are listed in Table 5.1. The size of the encounter region indicates how effectively prey are encountered. Thus it is more difficult for jellyfish to capture finite-size prey than ideal, infinitesimal prey. The capability to generate a directional escape force further enhances prey escape from the predator, consistent with physical intuition.

prey characteristics	area of encounter region	volume of encounter region
$a = 0$, $\mathbf{a}_e = 0$	1	1
$a = 1$ mm, $\mathbf{a}_e = 0$	0.93±0.04	0.90±0.05
$a = 1$ mm, $\mathbf{a}_e = 0.05$ m/s^2 (O)	0.74±0.04	0.64±0.06
$a = 1$ mm, $\mathbf{a}_e = 0.05$ m/s^2 (N)	0.78±0.05	0.68±0.07

Table 5.1: Area/volume of encounter regions for different types of prey, normalized to that of ideal infinitesimal prey. (O) represents for $\mathbf{a}_e$ opposite to the flow direction and (N) represents for $\mathbf{a}_e$ normal to the flow direction. The numbers are shown in the form of the average and the standard deviation from the five animals studied.

The results shown above assumed that the escape response starts at the beginning of calculation, i.e., the prey constantly exhibits the escape response. However, in reality this is not the case. Studies show that escape reaction is usually inhibited in the absence of a predator because it requires up to 400 times the normal energetic expenditure for copepods (Strickler, 1975; Fields and Yen, 1997).

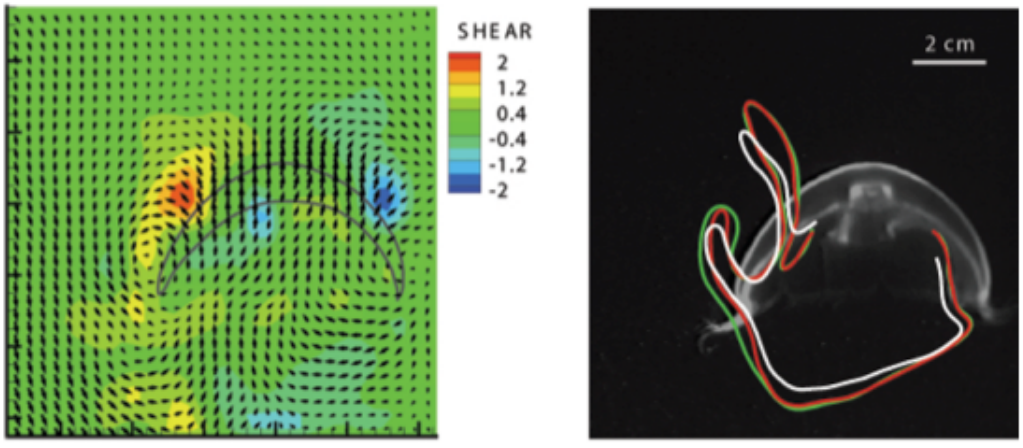

Figure 5.7: (A) Shear rate of the flow. Unit: s^{-1}. The position of jellyfish is given by its surface. (B) pLCS and encounter regions for prey with different perception threshold values. White: $\tau_{th} = 0$ (constant escape response); red: $\tau_{th} = 1s^{-1}$; green: $\tau_{th} = \infty$ (no escape response).

Thus escape reaction is elicited upon the perception of a measurable fluid mechanical signal in the flow generated by the predator. The signal can be disturbance in velocity or acceleration, but the most established signal is flow shear rate. A threshold value for shear rate, 1.5 to 8 s^{-1}, is required to initiate escape reaction for copepods (Fields and Yen, 1997). The contour plot of shear rate of the flow generated by the same jellyfish is shown in Fig. 5.7A. The regions with high shear are in the vicinity of the jellyfish, which implies that prey might not be able to perceive the disturbance until they are close to the predator. To study the effect of the threshold value on escape from the predator, pLCS and encounter regions are identified for different thresholds for shear perception: τ_{th} = 0, 1 s^{-1}, and ∞. Threshold value for shear $\tau_{th} = 0$ is equivalent to a consistent escape response, while $\tau_{th} = \infty$ is equivalent to no escape response. The prey has a size of $a = 1$ mm with an escape acceleration $\mathbf{a}_e = 0.05$ m/s^2 and opposite to local flow velocity. It is assumed that prey do not initiate escape response until they perceive the local shear rate higher than the threshold. After the escape response is initiated, it persists even if the local shear rate drops below the threshold. The pLCS and encounter regions are plotted in Fig. 5.7B: the white curve is the pLCS for prey with perception threshold $\tau_{th} = 0$; the red curve is the pLCS for prey with $\tau_{th} = 1$ s^{-1}; and the green curve is the pLCS for prey with $\tau_{th} = \infty$. The sizes of encounter regions for prey with different

perception thresholds are listed in Table 5.2, normalized with the case of with $\tau_{th} = \infty$ (no response) for individual animals. As the threshold value for perception decreases, the size of the encounter region also decreases. This is because prey are able to initiate the escape response earlier if they can perceive the shear rate at a lower level, thus enabling escape from the predator.

prey characteristics	area of encounter region	volume of encounter region
$\tau_{th} = \infty$ (no response)	1	1
$\tau_{th} = 1\ s^{-1}$	0.94±0.02	0.91±0.03
$\tau_{th} = 0$	0.81±0.04	0.72±0.06

Table 5.2: Area/volume of encounter regions for prey with different perception threshold values, normalized with the case of $\tau_{th} = \infty$ (no response). The prey has a size of $a = 1$ mm with an escape acceleration $\mathbf{a}_e = 0.05$ m/s^2 opposite to local flow velocity. The numbers are shown in the form of the average and the standard deviation from the five animals studied.

5.5 Discussion

5.5.1 The Medusan Feeding Model

The method described in this study represents a new approach to study prey encounter by medusan predators that generate feeding current to transport prey. The pLCS determined from the physical model provides a clear description of the regions in the flow from which encountered prey originate and the medusan predation can be quantified based on the size of the encounter regions. The locations of the lobes explains why spatially heterogenous encounter regions are observed in prey tracking experiments.

In the current study, the prey equation of motion was developed from the simplified Maxey-Riley equation for small, spherical, rigid particles. The Faxen correction terms with $a^2\boldsymbol{\Delta}\mathbf{u}$ and the Basset-Boussinesq memory term are both neglected. The Faxen correction gives a small correction with scale of $O(a^2/L^2)$ relative to the flow and particle motion. The memory term is $O(a^2U/L\nu)^{1/2} \sim St^{1/2}$ compared with Stokes drag. Both terms can be neglected for small particles in low Reynolds number

flows. Some other effect are also neglected by using the Maxey-Riley equation. The particle is assumed to be far way from from any other particle so particle-particle interactions are neglected. The Oseen correction to drag and the Saffman side force, both due to particle rotation, are also neglected, as they have scales of $O(a^2U/L\nu)$ and $O(a^2U/L\nu)^{1/2}$ respectively compared with Stoke drag (maxey and Riley, 1983).

Previous models of medusan feeding appeal to a marginal flow mechanism, which relies on the comparison between prey escape speeds and flow velocities at jellyfish bell margins (Costello and Colin, 1994; Sullivan et al., 1994). Prey with slow escape speeds are drawn to capture surfaces by flow generated by jellyfish at their bell margins. In contrast, the present model directly incorporates prey size, escape forces, and perception threshold. By modeling different prey particles, it is found that compared with ideal infinitesimal prey, the encounter regions for prey with inertia and escape force can be significantly smaller. The differences (up to 26% in area, Table 5.1) are outside the calculation uncertainty (3%), of which the major part is introduced when exacting pLCS from the FTLE plot. The results show that due to inertia, some prey that would be captured if infinitesimal are not captured by the jellyfish, mostly near the boundary of the encounter region. This result is consistent with physical intuition, and it demonstrates that the Lagrangian approach can be used to determine the scaling of feeding efficacy with prey size, a key determinant of ecological niche. Moreover, the method is able to incorporate the escape mechanisms of prey and study their effect on medusan predation. The study demonstrates that specific escape strategies, such as acceleration opposite or normal to the local fluid flow, and escape response initiation early at perception of the predator further aid prey escape. Further studies will focus on other prey escape behaviors and their effects on prey selection.

The model provides a way to isolate a prey parameter from the others and to study its effect on the predation. This can not be achieved in empirical studies, because these parameters are usually inter-dependent. For example, larger zooplankton generally have better swimming capability. When a reduced predation rate is observed in empirical studies for a larger prey than a smaller one, it is difficult to know whether it is primarily due to the size or its swimming capability. However, this

model enables quantification of effects of each parameter. Therefore the model has the potential to find the dominant parameters in the predation process. Additional studies are required to explore the properties of representative prey and to gain further insight into these prey parameters.

The heterogeneity of the encounter region observed in prey tracking experiments (Fig. 5.1) is explained by the configuration of lobes in pLCS (Fig. 5.4). The reason that there are gaps between lobes of encounter regions is that the jellyfish cannot generate feeding currents continuously. As it relaxes its bell, it can generate feeding currents to entrain prey outside the bell into the subumbrellar cavity and the lobes indicate the regions characterized by prey entrainment into the subumbrellar cavity. When the jellyfish contracts the bell, prey are not drawn into the subumbrellar cavity, instead they are transported downstream (Dabiri et al., 2005). Therefore, there are gaps between lobes due to the alternation between contraction and subsequent bell relaxation. During each complete pulsation cycle, prey in one lobe are entrained into the subumbrellar cavity and contact the jellyfish capture surfaces (i.e., tentacles and oral arms) as the fluid flows from the bell exterior into the subumbrellar cavity (i.e., Costello and Colin 1994). At the same time, as the jellyfish swims forward, new lobes will form at the opening of the pLCS. These properties are the same as fluid LCS in Shadden et al. (2006).

The quantification of the encounter region also enables the determination of encounter rate. Because prey in one lobe are entrained into the subumbrellar cavity during a pulsation cycle, the encounter rate of the jellyfish can be quantified as the time-averaged entraining rate, i.e., the volume of a lobe divided by the duration of pulsation cycle. Using the axisymmetric assumption, the average volume of the two lobes on the left-hand side of the jellyfish body axis (Fig. 5.8) is used to obtain the encounter rate of 34.2 l medusa^{-1} hr^{-1}. Based on laboratory studies, Titelman and Hansson (2006) estimate that *Aurelia sp.* of a similar size to that used in our study has a clearance rate of approximately 13.4 l medusa^{-1} hr^{-1} or about 40% of the estimate encounter rate. This level of agreement might be expected since the present hydrodynamically-based estimate does not include post-contact processes (i.e., nematocyst retention, transfer efficiencies from capture surface to the mouth – Hansson and Kiorboe, 2006) that may lower actual ingestion, and hence empirical clearance

rates, after encounter with prey. This indicates that the hydrodynamically-based estimation in this study represents the upper limit for medusan prey capture and actual prey clearance rates are modified by post-encounter chararacteristics of specific predator-prey combinations. In fact, combining the model estimation and the empirical measurement, it is possible to estimate the capture efficiency after encounter as the ratio of empirical clearance rate to the encounter rate predicted by the model (i.e., around 40% for the species *Aurelia sp.*).

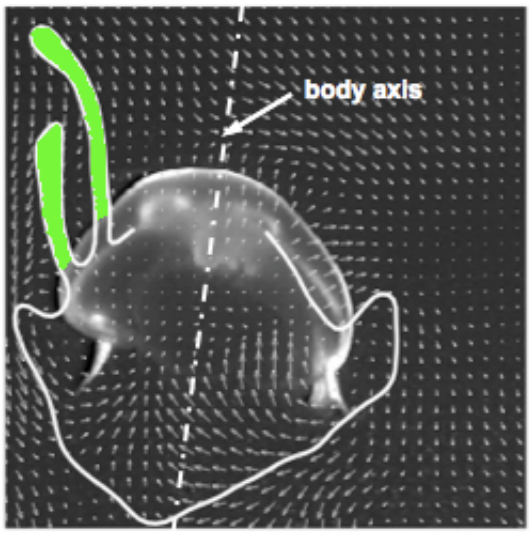

Figure 5.8: Two lobes (green) of the pLCS were used to determine the clearance rate with the axisymmetric assumption.

The characteristics of the encounter region, i.e., the subumbrellar cavity and the elongated lobes shown in this study, are consistent in results of multiple animals of the same species (Fig. 5.6). Other species of rowing or cruising scyphomedusae and hydromedusae generate flow patterns similar to those of *Aurelia sp.* (Costello and Colin, 1995; Colin and Costello, 2002; Colin et al., 2006). However, variable tentacle and oral arm morphologies can result in different encounter locations between predators and prey. For example, scyphomedusae with trailing tentacles and oral arms, such as Chrysaora quinquicirra and Cyanea capillata, can encounter prey in the flow during both the expansion and contraction phases of the swimming cycle (Ford et al., 1997; Higgins et al., 2008). Therefore, their encounter regions may be continuous in the circumferential direction and not exhibit lobes. Likewise, upstream cruising foragers which position their tentacles aborally, such

as Solmissus albescens and Nausitho punctata (Colin et al., 2006), may encounter prey in the flow that is transported around their bell at a distance shorter than the length the tentacles are extended. Such changes in encounter regions due to morphological variations will also change predation rates.

The depictions (e.g., Figs 5.4-5.7) show only snapshots of pLCS and the potential encounter regions for a given time instance. However, the pLCS and the encounter region evolve over time. Because the pLCS are boundaries of the prey encounter region, its evolution shows the transport of prey over time. Fig. 5.9 plots the pLCS (red) and encounter regions at four time instances during the jellyfish swimming cycle. The prey has a size of $a = 1$ mm with a consistent escape force $\mathbf{a}_e = 0.05$ m/s^2 and opposite to local flow velocity. Also plotted are the pLCS (white) for ideal infinitesimal prey. The encounter region for the former is consistently smaller than that for the latter. Fig. 5.9 shows that while the animal swims, the lobes of pLCS on top of the jelly advect downward and are sampled by the jelly and new lobes form upstream, consistent with previous studies (Shadden et al., 2006; Franco et al., 2007). Prey inside the lobes are captured by the jellyfish. To determine the time-averaged encounter probability around the jellyfish, pLCS for a series of frames over two swimming cycles are calculated and different values are assigned accordingly on nodes on a fix grid in a reference frame attached to the jellyfish. On each frame, nodes inside pLCS are assigned value 1 and nodes outside the pLCS are assigned value 0 for each frame. The values are summed up and divided by the total number of frames to calculate the time-averaged encounter probability (Fig. 5.10). This time-averaged encounter map maintains the characteristic pattern of high encounter probability regions separated by low encounter probability gaps.

5.5.2 The pLCS Approach

In this study, a pLCS framework is developed to study transport of inertial and active particles in fluid flows. The framework is based on Lagrangian trajectories of particles, determined from the equation of motion describing their dynamics. FTLE is calculated from particle trajectories and pLCS is identified as the kinematic boundaries for particle transport. As a demonstration, the

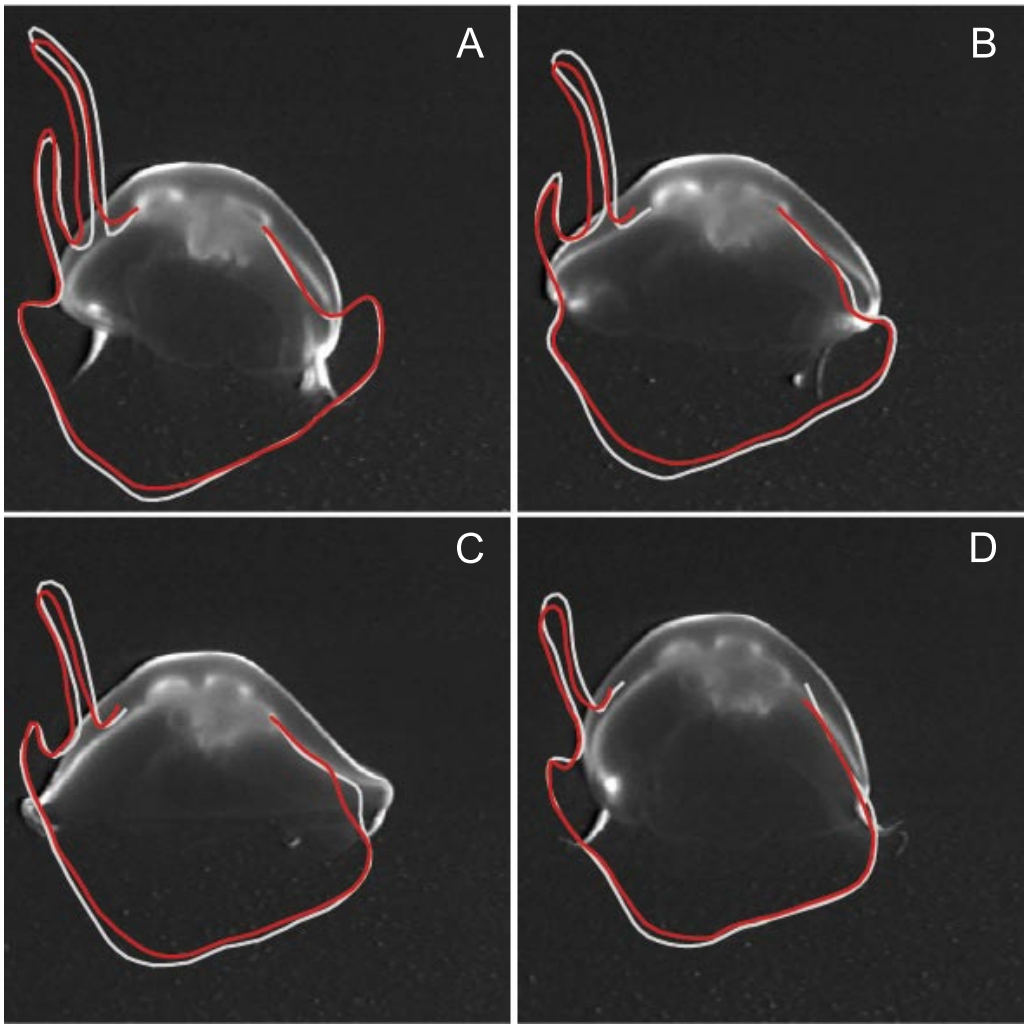

Figure 5.9: Encounter regions for the jellyfish at four time instances during a swimming cycle. (A) $t = 0$, (B)$t = 1.07$ s, (C) $t = 2.13$ s, and (D) $t = 3.27$ s. White: pLCS for ideal infinitesimal prey; red: pLCS for prey ($a = 1$mm) with escape acceleration ($\mathbf{a}_e = 0.05$ m/s^2) opposite to local flow velocity.

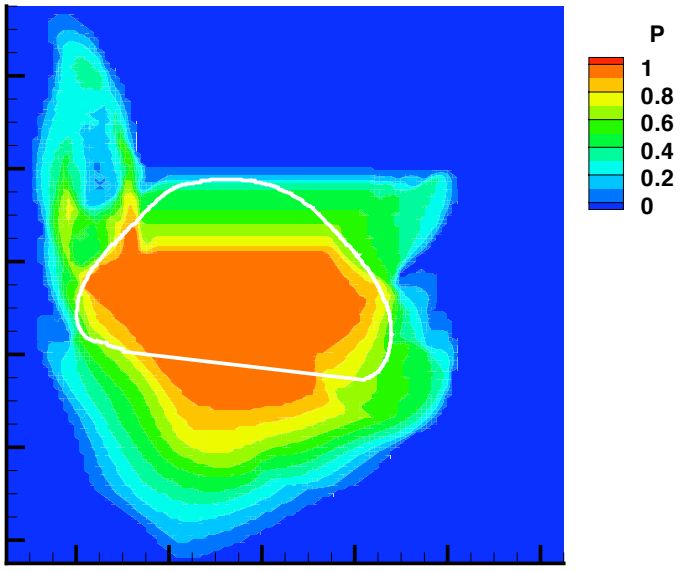

Figure 5.10: The time-averaged encounter probability around the jellyfish. Solid white: the body outline of the jellyfish.

framework is applied to a planktonic predatory system, i.e., jellyfish feeding on small zooplankton. The pLCS separate prey encounter region from prey escape region.

Please note that the present study is 2-D. The measured flow field is a planar cross-section of a 3-D flow, thus the pLCS is the intersection of a 2-D surface with that plane. Nonetheless, the methods described here are not limited to 2-D flow. The Maxey-Riley equation is able to describe particle motions in 3-D and the pLCS analysis is also able to apply to fully 3-D flow. For 3-D flows, the pLCS are surfaces rather than curves and they enclose a capture volume rather than an area. Table 1 and 2 also list the size of normalized capture volume, assuming the pLCS is axisymmetric. The differences in capture volume sizes are more pronounced.

The modified Maxey-Riley equation with a forcing term can be used to study the behaviors of small planktonic animals in fluid flows other than those generated by predators, such as larvae dispersion and sedimentation. Most previous studies on active motion of small biological larvae assume that the velocity of the animal in a flow is the vector sum of animal swimming velocity in still fluid and the ambient current velocity (e.g., Koehl and Reidenbach, 2007). The proposed equation of motion incorporates additional parameters and considers the interaction between fluid

and animal on the force balance, and thus can potentially provide a more accurate way to describe the dynamics.

Only forward-time FTLE is calculated in the current study. Prey particles are released at certain positions and their forward-time trajectories are followed. The corresponding pLCS are repelling, meaning prey always move away from them. However, for the simplified Maxey-Riley equation (Eqn. 5.4), the problem of source inversion, i.e., locating initial positions from current locations, is ill-posed (Haller and Sapsis, 2008). As suggested, when integrating in backward-time, Eqn. 5.4 generates strong exponential growth with exponent of particle size parameter A. This causes numerical instability and blowup in calculation. Because backward-time trajectories are required to compute backward-time FTLE, it is difficult to determine the corresponding attracting pLCS. An invariant slow manifold is introduced to overcome this problem (Sapsis and Haller, 2009). When A is large enough (particle is small enough), the dynamical systems described by Eqn. 5.4 have a slow manifold in the form

$$M_e = \left\{ (\mathbf{x}, \mathbf{v}) : \mathbf{v} = \mathbf{u} + \frac{1}{A}\left(\frac{3R}{2} - 1\right)\left[\frac{D\mathbf{u}}{Dt} - \mathbf{g}\right] + O(1/A^2) \right\}. \tag{5.7}$$

Particles converge fast onto this slow manifold M_e and their dynamics on M_e is described by

$$\dot{\mathbf{x}} = \mathbf{u} + \frac{1}{A}\left(\frac{3R}{2} - 1\right)\left[\frac{D\mathbf{u}}{Dt} - \mathbf{g}\right]. \tag{5.8}$$

Different from Eqn. 5.4, Eqn 5.8 has no singular perturbation terms, and hence no associated instability in backward time. Using Eqn. 5.8, backward-time trajectories can be calculated and the initial positions can be determined from their later locations. Moreover, the slow manifold M_e acts as the attracting surfaces in the particle transport. This method of slow manifold has been applied to source detection of an atmospheric contamination source (Tang et al., 2009), as well as droplets debris congregation in a hurricane (Sapsis and Haller, 2009).

The pLCS methodology proposed in the present study can be used to study transport and mixing of particles with any form of equation of motion. Other examples in natural transport systems

include transport of pollutants in the atmosphere and on ocean surface, transport of organisms in deep water upwelling, dispersion and sedimentation of biomass, etc. Further study will incorporate reactivity of advected organisms to study the interaction between ocean mixing and chemical and biological activities, such as plankton blooming. The method can be equally applicable to engineering systems, such as reacting particles or charged particles. As long as the particle trajectories can be calculated from their equations of motion, or directly measured from experiments, pLCS can be calculated from these trajectories. This makes the method useful for a broad range of fluid mechanics applications, including multiphase and granular flows. As a tentative effort, equations of motion for several particle transport systems are presented below. With the dynamics of particles described by these equations, Lagrangian trajectories can be predicted and pLCS can be used to identify distinct kinematic regions in these transport systems.

I. Electromagnetic force and charged particles

The Maxey-Riley equation does not include electromagnetic forces. If a particle has charge q and can be treated as a point charge, the electromagnetic force acting on it from an electronic field $\mathbf{E}$ and a magnetic field $\mathbf{B}$ is

$$\mathbf{F}_E = q(\mathbf{E} + \mathbf{v} \times \mathbf{B}), \tag{5.9}$$

where $\mathbf{v}$ is the particle velocity. Adding to the right-hand-side of Eqn. 5.4, it gives the equation of motion for a small, rigid, spherical, charged particle in fluid flow $\mathbf{u}$ with an electronic field $\mathbf{E}$ and a magnetic field $\mathbf{B}$ as

$$\frac{d\mathbf{v}}{dt} - \frac{3R}{2}\frac{D\mathbf{u}}{Dt} = -A(\mathbf{v} - \mathbf{u}) + (1 - \frac{3R}{2})\mathbf{g} + q(\mathbf{E} + \mathbf{v} \times \mathbf{B})/m. \tag{5.10}$$

To satisfy the assumptions of the original Maxey-Riley equation, the electromagnetic force acting on the particle needs to be on the same or smaller order of magnitude of the Stokes drag, i.e., $F_E/6\pi\mu W \leq O(1)$.

II. Coriolis force

In many meso scale geological transport systems, due to the necessity of using the Earth as the rotating reference frame, the Coriolis force needs to be considered. For a rotating coordinate frame with angular velocity Ω, the Coriolis acceleration acting on a particle with velocity $\mathbf{v}$ is

$$\mathbf{a}_c = -2\Omega \times \mathbf{v}. \tag{5.11}$$

Therefore, the Maxey-Riley equation with Coriolis effect is

$$\frac{d\mathbf{v}}{dt} - \frac{3R}{2}\frac{D\mathbf{u}}{Dt} = -A(\mathbf{v} - \mathbf{u}) + (1 - \frac{3R}{2})\mathbf{g} - 2\Omega \times \mathbf{v}. \tag{5.12}$$

This equation has been used to study transport of droplets and debris in a hurricane (Sapsis and Haller, 2009).

III. Transport of volcano ashes in the atmosphere

Ash clouds from volcanic eruption are serious problems facing public health and air traffic security. The solid components of volcanic ash clouds are generally sub-millimeter sized particles of rock (tephra). Many volcanic ash transport and dispersion (VATD) models have been developed to simulate the movement of airborne ash in near real-time following an eruption. These models are usually coupled with numerical weather prediction (NWP) data to predict transport of volcano ash clouds in the atmosphere.

One of the popular VATD models is PUFF, a model that tracks particles through a Lagrangian formulation of advection, fallout, and turbulent diffusion using a random-walk technique (Searcy et al., 1998). The kinematics of volcano ash particles are described as

$$\mathbf{v}(t) = \mathbf{w}(t) + \mathbf{z}(t) + \mathbf{s}(t). \tag{5.13}$$

In this equation, $\mathbf{v}(t)$ is the velocity vector of the ash particle at time t. $\mathbf{w}(t)$ is the local wind

velocity simulated from NWP models. $\mathbf{z}(t)$ is a velocity representing turbulent dispersion described by a Rondom-walk process. In practice,

$$\mathbf{z}(t) = \mathbf{r}\sqrt{2nK/\Delta t}, \tag{5.14}$$

in which $\mathbf{r}$ is a unit random vector, n is the dimensionality of the system, K is the diffusivity, and Δt is the time step size. The last term $\mathbf{s}(t)$ is the terminal, gravitational fallout velocity, dependent on the particle's size and evaluated by Stoke's law through the relation

$$\mathbf{s} = 2\rho\mathbf{g}d^2/9\mu, \tag{5.15}$$

where ρ is the density of the particle, μ the dynamic viscosity coefficient, $\mathbf{g}$ the gravitational acceleration, and d is the particles size. Strictly speaking, the equation of motion (Eqn.5.13) is not a dynamical equation, but it describes the motion of ash particles and their trajectories. Thus, it is sufficient to provide input trajectories for the pLCS analysis.

5.6 Acknowledgements

The author thanks Dr. John Costello and Dr. Sean Colin for collaborating on this study. The author also thanks Cabrillo Marine Aquarium for providing animals and assistance with experiments.

Chapter 6

Conclusion

In this thesis, Lagrangian analyses are applied to study fluid transport processes related to two important functionalities of aquatic animals: locomotion and feeding. Although the interaction between animals and their fluid environments are different, these fluid transport processes share a common motif, i.e., the transport of fluid, biomass, momentum and energy. LCS analysis provides a unified approach studying these transport processes. It is able to identify transport boundaries in transport systems, and these boundaries can be correlated with fluid, biomass, momentum, and energy transport.

During locomotion, animals deliver momentum into the surrounding fluid in the form of vortices to generate lift and thrust. The LCS analysis identifies boundary of isolated vortices, as demonstrated in the sunfish pectoral study. When the vorticity is compact and resides within the vortex, the dynamics of the LCS is described by potential flow theory. The kinematics of vortex boundary is used to deduce the momentum of the wake vortex and its added-mass, leading to a quantitative evaluation of instantaneous locomotive forces. When the wake is in the form of a vortex street, as shown in the simulation of undulatory swimming, the LCS analysis identifies the boundary of the vortex street in the downstream. Moreover, it also shows 'upstream structures', which are the portion of fluid that will later interact with the swimmer and form the vortices. Combining the kinematics of the LCS and the animal, a mass flow rate is then defined and a momentum flux is calculated. Therefore, the transport of fluid mass is correlated with the transport of momentum. A metric for propulsive efficiency is established using the momentum flux, which can be used to

measure and compare the efficiency of aquatic animal locomotion.

The original LCS analysis is modified to apply to dynamic systems of inertial, active particles, which has different dynamics from ideal fluid tracers. The concept of pLCS is developed as transport barriers in the dynamical systems of particles with any form of equation of motion. In the application to prey transport in jellyfish feeding, it is demonstrated that the location of boundaries between distinct kinematic regions, i.e. pLCS, is dependent on the property and dynamics of particles. The study is able demonstrate prey selection based on prey size and escape behaviors and provide a mechanical basis for evaluating the predatory role of medusae in marine planktonic ecosystems. The pLCS methodology extends the original LCS analysis on fluid transport to particle transport with any equation of motion, and broadens its potential application to a wide range of transport systems.

Appendix A

Other Studies

There are two other LCS-related studies which I have worked on. In one study, primary and secondary intersection points are defined for convoluted configurations of repelling and attracting LCS in order to formulate a unique, physically motivated definition for fluid exchange surfaces and transport lobes in the flow. The concepts are applied to study fluid transport in numerical simulations of two-dimensional cross flow past a circular cylinder at a Reynolds number of 200; and in measurements of a freely swimming jellyfish.

In the other study, the implementation of LCS analysis in low Reynolds number flows (O(1) – O(100)) is explored, in which viscous diffusion rapidly diminishs the vorticity in the wake. A numerical model is developed to simulate self-propulsion of an articulated jellyfish-like swimmer and the LCS analysis is applied to the flow. The study can help understand locomotion and feeding of jellyfish ephyrae (larvae), which swim at low Reynolds number due to their small size and low cruising speed.

These two studies are included in two publications listed below.

Franco, E., Pekarek, D.N., Peng, J., Dabiri, J.O. Geometry of unsteady fluid transport during fluid-structure interactions. *J. Fluid Mech.* 589: 125-145, 2007.

Wilson, M., Peng, J., Dabiri, J.O., Eldredge, J.D. Lagrangian coherent structures in low Reynolds number swimming. *J. Phys. Condens. Matter* 21: 204105, 2009.

Bibliography

[1] Alben, S., Shelley, M., Zhang, J. Drag reduction through self-similar bending of a flexible body. *Nature* 420: 479–481, 2002.

[2] Alben, S. Optimal flexibility of a flapping appendage at high Reynolds number. *J. Fluid Mech.* 614: 355–380, 2008.

[3] Aref, H. Stirring by chaotic advection. *J. Fluid Mech.* 143: 1–21, 1984.

[4] Babiano, A., Cartwright, J. H. E., Piro, O., Provenzale, A. Dynamics of a Small Neutrally Buoyant Sphere in a Fluid and Targeting in Hamiltonian Systems. *Phys. Rev. Lett.* 84: 5764–5767, 2000.

[5] Bartol, I.K., Gharib, M., Webb, P.W., Weihs, D., Gordon, M.S. Body-induced vortical flows: a common mechanism for self-corrective trimming control in boxfishes. *J. Exp. Biol.* 208: 327–344, 2005.

[6] s Benczik, I. J., Toroczkai, Z., Tel T. Advection of finite-size particles in open flows. *Phys. Rev. E.* 67: 036303, 2003.

[7] Biewener, A. *Animal Locomotion* (ed. T.Y.-T. Wu, C.J. Brokaw & C. Brennan). Oxford: Oxford Univ. Press, 2003.

[8] Chorin, A.J., Bernard, P.S. Discretization of a vortex sheet, with an example of roll-up. *J. Comput. Phys.* 13, 423–429, 1973

[9] Colin, S. P., Costello, J. H. Morphology, swimming performance and propulsive mode of six co-occurring hydromedusae. *J. Exp. Biol.* 203: 427–437, 2002.

[10] Colin, S. P., Costello, J. H., Klos, E. *In situ* swimming and feeding behaviour of eight co-occurring hydromedusae. *Mar. Ecol. Prog. Ser.* 253: 305–309, 2003.

[11] Colin, S. P., Costello, J. H., Kordula, H. Upstream foraging by medusae. *Mar. Ecol. Prog. Ser.* 327: 143–155, 2006.

[12] Costello, J. H., Colin, S. P. Morphology, fluid motion and predation by the scyphomedusa *Aurelia Aurita*. *Mar. Biol.* 121: 327–334, 1994.

[13] Costello, J. H., Colin, S. P. Flow and feeding by swimming scyphomedusae. *Mar. Ecol. Prog. Ser.* 124: 399–406, 1995.

[14] Dabiri, J. O. Note on the induced Lagrangian drift and added-mass of a vortex.*J. Fluid Mech.* 547: 105–113, 2006.

[15] Dabiri, J. O., Colin, S. P., Costello, J. H. Fast-swimming hydromedusae exploit velar kinematics to form an optimal vortex wake. *J. Exp. Biol.* 209: 2025–2033, 2006.

[16] Dabiri, J. O., Colin, S. P., Costello, J. H., Gharib, M. Flow patterns generated by oblate medusan swimmers: in situ observation and analysis. *J. Exp. Biol.* 208: 1257–1269, 2005.

[17] Dabiri, J. O., Gharib, M. Fluid entrainment by isolated vortex rings*J. Fluid Mech.* 511: 311–331, 2006.

[18] Daniel, T.L. Unsteady aspects of aquatic locomotion. *Am. Zool.* 24: 121–134, 1984.

[19] Denissenko, P., Lukaschuk, S., Breithaupt, T. The flow generated by an active olfactory system of the red swamp crayfish. *J. Exp. Biol.* 210: 4083–4091, 2007.

[20] Dickinson, M.H. Unsteady mechanisms of force generation in aquatic and aerial locomotion. *Am. Zool.* 36: 537–554, 1996.

[21] Dickinson, M.H., Gotz, K. G. The wake dynamics and flight forces of the fruit fly *Drosophila melanogaster*. *J. Exp. Biol.* 199: 2085–2104, 1996.

[22] Dickinson, M.H., Lehmann, F.O., Sane, S.P. Wing rotation and the aerodynamic basis of insect flight. *Science* 284: 1954–1960, 1999.

[23] Drucker, E.G., Lauder, G.V. Locomotor forces on a swimming fish: three-dimensional vortex wake dynamics quantified using digital particle image velocimetry. *J. Exp. Biol.* 202: 2393–2412, 1999.

[24] Drucker, E.G., Lauder, G.V. A hydrodynamic analysis of fish swimming speed: wake structure and locomotor force in slow and fast labriform swimmers. *J. Exp. Biol.* 203: 2379–2393, 2000.

[25] Drucker, E.G., Lauder, G.V. Wake dynamics and fluid forces of turning maneuvers in sunfish.*J. Exp. Biol.* 204: 431–442, 2001.

[26] Drucker, E.G., Lauder, G.V. Function of pectoral fins in rainbow trout: behavioral repertoire and hydrodynamic forces. *J. Exp. Biol.* 206: 813–826, 2003.

[27] Eldredge, J.D. Numerical simulations of undulatory swimming at moderate Reynolds number *Bioinsp. Biomim.* 1: S19–S24, 2006.

[28] Ellington, C.P., van den Berg, C., Willmott, A.P., Thomas, A.L.R. Leading edge vortices in insect flight. *Nature* 384: 626–630, 1996.

[29] Fields, D.M., Yen, J. The escape behaviour of Pleuromamma xiphias in response to a quantifiable fluid mechanical disturbance, p 323-340. In: Lenz PH, Hartline DK, Purcell JE, Macmillan DL [eds.] Zooplankton: sensory ecology and physiology, Vol 1. Gordon and Breach Publishers, Amsterdam. 1996.

[30] Fields, D.M., Yen, J. The escape behavior of marine copepods in response to a quantifiable fluid mechanical disturbance. *J. Plankton Res.* 19: 1289–1304, 1997.

[31] Ford, M.D., Costello, J.H., Heidelberg, K.B., Purcell, J.E. Swimming and feeding by the scyphomedusa *Chrysaora quinquecirrha*. *Mar. Biol.* 129: 355–362, 1997.

[32] Franco, E., Pekarek, D. N., Peng, J., Dabiri, J. O. Geometry of unsteady fluid transport during fluidstructure interactions. *J. Fluid Mech.* 589: 125–145, 2007.

[33] Gibb, A., Jayne, B. C. and Lauder, G. V. Kinematics of pectoral fin locomotion in the bluegill sunfish *Lepomis macrochirus*. *J. Exp. Biol.* 189: 133–161, 1994.

[34] Galper, A., Miloh, T. Dynamic equations of motion for a rigid or deformable body in an arbitrary non-uniform potential flow field. *J. Fluid Mech.* 295: 91–120, 1995.

[35] Haller, G., Yuan, G. Lagrangian coherent structures and mixing in two-dimensional turbulence. *Physica D*, 147: 352370, 2000.

[36] Haller, G. Distinguished material surfaces and coherent structures in 3D fluid flows. *Physica D*, 149: 248277, 2001.

[37] Haller, G. Lagrangian coherent structures from approximate velocity data. *Phys. Fluids* 14: 1851–186, 2002.

[38] Haller, G. An objective definition of a vortex. *J. Fluid Mech.* 525: 1–26, 2005.

[39] Haller, G., Sapsis, T. Where do inertial particles go in fluid flows? *Physica D*, 237: 573583, 2008.

[40] Hansson, L.J., Moeslund, O., Kiorboe, T., Riisgard, H.U. Clearance rates of jellyfish and their potential predation impact on zooplankton and fish larvae in a neritic ecosystem (Limfjorden, Denmark). *Mar. Ecol. Prog. Ser.* 304: 117–131, 2005.

[41] Hedenstrom A, Johansson, L.C., Wolf, M., von Busse, R., Winter, Y., Spedding, G.R. Bat flight generates complex aerodynamic tracks. *Science* 316: 894–897, 2007.

[42] Higgins, J.E., Ford, M.D., Costello, J.H. Transitions in morphology, nematocyst distribution, fluid motions, and prey capture during development of the scyphomedusa *Cyanea capillata*. *Biol. Bulletin.* 214: 29–41, 2008.

[43] Jiang, H. and Paffenhofer G.A. Hydrodynamic signal perception by the copepod *Oithona plumifera* *Mar. Ecol. Prog. Ser.* 373: 37–52, 2008.

[44] Johansson, L. C., Lauder, G. V. Hydrodynamics of surface swimming in leopard frogs (*Rana pipiens*). *J. Exp. Biol.* 207: 3945–3958, 2003.

[45] Jones, M.A. The separated flow of an inviscid fluid around a moving flat plate. *J. Fluids Mech.* 496: 405–441, 2003.

[46] Kawahara, M., Uye, S., Ohtsu, K., Izumi, H. Unusual population explosion of the giant jellyfish *Nemopilemia nomurai* (Scyphozoa : Rhizostomeae) in East Asian waters. *Mar. Ecol. Prog. Ser.* 307: 161–173, 2006.

[48] Kiorboe, T., Visser, A. Predator and prey perception in copepods due to hydromechanical signals. *Mar. Ecol. Prog. Ser.* 179: 81–95, 1999.

[48] Kiorboe, T., Saiz, E, Visser, A. Hydrodynamic signal perception in the copepod *Acartia tonsa*. *Mar. Ecol. Prog. Ser.* 179: 97–111, 1999.

[49] Kiorboe, T., Saiz, E. Planktivorous feeding in calm and turbulent environments, with emphasis on copepods. *Mar. Ecol. Prog. Ser.* 122: 135–145, 1995.

[50] Koehl, M. A. R., Reidenbach, M. A. Swimming by microscopic organisms in ambient water flow. *Exp. Fluids* 43: 755–768, 2007.

[51] Koehl, M. A. R., Koseff, J. R., Crimaldi, J. P., McCay, M. G., Cooper, T., Wiley, M. B. and Moore, P. A. Lobster sniffing: antennule design and hydrodynamic filtering of information in an odor plume. *Science* 294: 1948–1951, 2001.

[52] Krueger, P.S. Measurement of propulsive power and evaluation of propulsive performance from the wake of a self-propelled vehicle. *Bioinsp. Biomim.* 1: 49–56, 2006.

[53] Lamb, H. *Hydrodynamics.* Cambridge: Cambridge University Press. 1932.

[54] Lauder, G. V., Madden, P. G. A., Mittal, R., Dong, H., Bozkurttas, M. Locomotion with flexible propulsors. I. Experimental analysis of pectoral fin swimming in sunfish. *Bioinspir. Biomimet.* 1: S25-S34, 2007.

[55] Lekien F., Shadden S.C. and Marsden J.E. Lagrangian coherent structures in n-dimensional systems. *J. Math. Phys.* 48: 065404, 2007.

[56] Liao, J.C., Beal, D.N., Lauder, G.V., Triantafyllou, M.S. The Krmn gait; novel kinematics of rainbow trout swimming in a vortex street. *J. Exp. Biol.* 206: 1059–1073, 2003.

[57] Liao, J.C., Beal, D.N., Lauder, G.V., Triantafyllou, M.S. Fish exploiting vortices decrease muscle activity. *Science* 302: 1566–1569, 2003.

[58] Lipinski, D., Cardwell, B., Mohseni, K. A Lagrangian analysis of a two-dimensional airfoil with vortex shedding. *J. Phys. A: Math. Theor.* 41: 344011, 2008.

[59] Mann, J., Ott, S., Andersen, J.S. Experimental study of relative, turbulent diffusion. Riso National Laboratory Report Riso-R-1036(EN), 1999.

[60] Mathur, M., Haller, G., Peacock, T., Ruppert-Felsot, J. E., Swinney, H. L. Uncovering the Lagrangian skeleton of turbulence. *Phys. Rev. Lett.* 98: 144502, 1997.

[61] Matsakis, S., Conover, R.J. Abundance and feeding of medusae and their potential impact as predators on other zooplankton in Bedford Basin (Nova Scotia, Canada) during spring. *Can. J. Fish. Aquat. Sci.* 48: 1419–1430, 1991.

[62] Maxworthy, T. Experiments on the Weis-Fogh mechanism of lift generation by insects in hovering flight. Part 1. Dynamics of the 'fling'. *J. Fluids Mech.* 93: 47–63, 1979.

[63] Maxey, M. R., Riley, J. J. Equation of motion for a small rigid sphere in a nonuniform flow. *Phys. Fluids* 26: 883–889, 1983.

[64] Michaelides, E. E. Review - The transient equation of motion for particles, bubbles, and droplets. *J. Fluids Eng.* 119: 233–247, 1997.

[65] Milne-Thomson, L. M. *Theoretical Hydrodynamics.* New York, Macmillan. 4th ed, 1960.

[66] Mittal, R., Dong, H., Bozkurttas, M., Lauder, G. V., Madden, P. G. A. Locomotion with flexible propulsors. II. Computational modeling and analysis of pectoral fin swimming in a sunfish. *Bioinspir. Biomimet.* 1: S35-S41, 2007.

[67] Muller, U,K,, van den Heuvel, B.L.E., Stamhuis, E.J., Videler, J.J. Fish foot prints: Morphology and energetics of the wake behind a continuously swimming mullet (Chelon labrosus Risso). *J. Exp. Biol.* 200: 2893–2906, 1997.

[68] Nauwelaerts, S., Stamhuis, E.J., Aerts, P. Propulsive force calculations in swimming frogs I. A momentum-impulse approach. *J. Exp. Biol.* 208: 1435–1443, 2005.

[69] Nitsche, M., Krasny, R. A numerical study of vortex ring formation at the edge of a circular tube. *J. Fluid Mech.* 276: 139–161, 1994.

[70] Pereira, F., Stuer, H., Graff, E.C., Gharib, M. Two-frame 3D particle tracking. *Annu. Rev. Fluid Mech.* 31: 1680–1692, 2006.

[71] Provenzale, A. Transport by coherent barotropic vortices. *Annu. Rev. Fluid Mech.* 31: 95–123, 1999.

[72] Purcell, J.E., Grover, J.J. Predation and food limitation as causes of mortality in larval herring at a spawning ground in British Columbia. *Mar. Ecol. Prog. Ser.* 59: 55–61, 1990.

[73] Purcell, J.E., Uye, S., Lo, W.T. Anthropogenic causes of jellyfish blooms and their direct consequences for humans: a review. *Mar. Ecol. Prog. Ser.* 350: 153–174, 2007.

[74] Rom-Kedar, V., Leonard, A., Wiggins, S. An analytical study of transport, mixing and chaos in an unsteady vortical flow. *J. Fluid Mech.* 214: 347–394, 1990.

[75] Rosenhead, L. *Laminar Boundary Layers.* New York: Dover Publications. 1963.

[76] Sapsis, T. and Haller, G. Inertial particle dynamics in a hurricane. *J. Atmosph. Sci.* in press, 2009.

[77] Searcy, C., Dean, K., Stringer, W. PUFF: A Lagrangian Trajectory Volcanic Ash Tracking Model *J. Volcanol. Geotherm. Res.* 80: 1–16, 1998.

[78] Schultz, W.W., Webb, P.W. Power requirements of swimming: Do new methods resolve old questions? *Integ. Comp. Biol.* 42: 1018–1025, 2002.

[79] Shadden, S. C., Lekien, F., Paduan J.D., Chavez F., Marsden, J. E. The correlation between surface drifters and coherent structures based on HF radar in Monterey Bay. *Deep-Sea Research II* 56: 161–172, 2009.

[80] Shadden, S.C., Taylor C.A. Characterization of coherent structures in the cardiovascular system. *Annals Biomed. Eng.* 36: 1152–1162, 2008.

[81] Shadden, S.C., Katija, K., Rosenfeld, M., Marsden, J.E., Dabiri, J.O. Transport and stirring induced by vortex formation. *J. Fluids Mech.* 593: 315–331, 2007.

[82] Shadden, S. C., Dabiri, J. O., Marsden, J. E. Lagrangian analysis of fluid transport in empirical vortex ring flows. *Phys. Fluids* 18: 047105, 2006.

[83] Shadden, S. C., Lekien, F., Marsden, J. E. Definition and properties of Lagrangian coherent structures from finite-time Lyapunov exponents in two-dimensional aperiodic flows. *Physica D* 212: 271–304, 2005.

[84] Shariff, K., Leonard, A., Ferziger, J. H. Dynamical systems analysis of fluid transport in time-periodic vortex ring flows. *Phys. Fluids* 18: 047104, 2006.

[85] Shukla, R.K., Eldredge, J.D. An inviscid model for vortex shedding from a deforming body. *Theor. Comp. Fluid Dyn.* 21: 343–368, 2007.

[86] Spedding, G.R., Rosen, M., Hedenstrom, A. A family of vortex wakes generated by a thrush nightingale in free flight in a wind tunnel over its entire natural range of flight speeds. *J. Exp. Biol.* 206: 2313–2344, 2003.

[87] Stamhuis, E.J., Nauwelaerts, S. Propulsive force calculations in swimming frogs. II. A vortex ring approach. *J. Exp. Biol.* 208: 1445–1451, 2005.

[88] Strickler, J. R. Swimming of planktonic Cyclops species (*Copepoda, Crustacea*): Pattern, movements and their control. In *Swimming and Flying in Nature* (ed. T.Y.-T. Wu, C.J. Brokaw & C. Brennan). Plenum Press, New York, 599–613, 1975.

[89] Sullivan, B. K., Garcia, J. R., Klein-MacPhee, G. Prey selection by the scyphomedusan predator *Aurelia Aurita*. *Mar. Biol.* 121: 335–341, 1994.

[90] Tang, W., Haller, G., Baik, J. J., Ryu, Y. H. Locating an atmospheric contamination source using slow manifolds. *Phys. Fluids* 21: 043302, 2009.

[91] Taylor, G.K., Nudds, R.L., Thomas, A.L. Flying and swimming animals cruise at a Strouhal number tuned for high power efficiency. *Nature* 425: 707–711, 2003.

[92] Tian, X., et al. Direct measurements of the kinematics and dynamics of bat flight. *Bioinsp. Biomim.* 1: S10–S18, 2006.

[93] Titelman, J., Hansson, L.J. Feeding rates of the jellyfish *Aurelia aurita* on fish larvae.. *Mar. Biol.* 149: 297–306, 2006.

[94] Triantafyllou, M.S., Triantafyllou, G.S., Gopalkrishnan, R. Wake mechanics for thrust generation in oscillating foils. *Phys. Fluids* 3: 2835–2837, 1991.

[95] Tytell, E.D., Lauder, G.V. The hydrodynamics of eel swimming - I. Wake structure. *J. Exp. Biol.* 207: 1825–1841, 2004.

[96] Tytell, E.D. Do trout swim better than eels? Challenges for estimating performance based on the wake of self-propelled bodies. *Exp. Fluid* 43: 701-712, 2007.

[97] Videler, J.J., Stamhuis, E.J., Povel, G.D.E. Leading-edge vortex lifts swifts. *Science* 306: 1960–1962, 2004.

[98] Walker, J. A. Dynamics of pectoral fin rowing in a fish with an extreme rowing stroke: the threespine stickleback (*Gasterosteus aculeatus*). *J. Exp. Biol.* 207: 1925–1939, 2004.

[99] Wang, Z.J. Dissecting insect flight. *Annu. Rev. Fluid Mech.* 37: 183-210, 2005.

[100] Warrick, D.R., Tobalske, B.W., Powers, D.R. Aerodynamics of the hovering hummingbird. *Nature* 435: 1094–1097, 2005.

[101] Webb, P. W., Blake, R. W. Swimming. In *Functional Vertebrate Morphology* (ed. M. Hildebrand, D. M. Bramble, K. F. Liem and D. B. Wake), 110–128, Cambridge, MA: Harvard University Press. 1985.

[102] Werth, A.J. Odontocete suction feeding: Experimental analysis of water flow and head shape. *J. Morph.* 267: 1415–1428, 2006.

[103] Wiggins, S. The dynamical systems approach to Langrangian transport in oceanic flows. *Annu. Rev. Fluid Mech.* 37: 295–328, 2005.

[104] Wilga, C.D., Lauder, G.V. Hydrodynamic function of the shark's tail. *Nature* 430: 805, 2005.

[105] Willert, C. E., Gharib, M. Digital particle image velocimetry. *Exp. Fluids* 10: 181–193, 1991.

[106] Vanella, M., Fitzgerald, T., Preidikman, S., Balaras, E., Balachandran, B. Influence of flexibility on the aerodynamic performance of a hovering wing. *J. Exp. Biol.* 212: 95–105, 2009.

[107] Vogel, S. *Life in Moving Fluids: The Physical Biology of Flow* (2nd edn). Princeton: Princeton University Press. 1994.

[108] Xu Z., Chen N., Shadden S.C., Marsden J.E., Kamocka M.M., Rosen E.D. and Alber M. Study of blood flow impact on growth of thrombi using a multiscale model. *Soft Matter* 5, 769–779, 2009.

[109] Zhu, Q. Numerical simulation of a flapping foil with chordwise or spanwise flexibility. *AIAA J.* 45, 2448–2457, 2007.